THE STRUCTURE OF THE NEUTRAL CURRENT COUPLING IN HIGH ENERGY NEUTRINO-NUCLEON INTERACTIONS

Thesis by

Frank Smith Merritt

In Partial Fulfillment of the Requirements

for the Degree of

Doctor of Philosophy

California Institute of Technology

Pasadena, California

1977

(Submitted January 4, 1977)

Acknowledgements

I am very much indebted to my adviser, Barry C. Barish, and to Frank Sciulli, for their insight and encouragement over the past years and for their efforts in creating an experiment and an atmosphere in which it is possible to do exciting physics. It has been a privilege to work on the neutrino experiments with them and with the other members of the Caltech group.

This neutral current experiment has been a part of the Caltech-Fermilab neutrino program and as such has depended, directly and indirectly, on the combined work and expertise of a large number of people. The data-collection and much of the analysis of this and other Caltech experiments have depended on the excellent interactive online software system developed by Fritz Bartlett. George Krafczyk, of Fermilab, has provided first rate technical expertise and much hard work from the beginning of the neutrino program, and has had a large influence on the successful operation of this experiment. The others who are responsible for the preparation and data-collection for this experiment are Arie Bodek, Wyatt Brown, Dave Buchholz, Gene Fisk, Francois Jacquet, Linda Stutte, and Henri Suter. Most of the analysis of the test-calorimeter data discussed in this thesis was done by Arie Bodek and Henri Suter. Much of the earlier development and construction of the experiment is due to the efforts of Al Mashke, Yori Nagashima, Dennis Shields, and Tom Humphrey.

The members of the Fermilab neutrino lab deserve credit for their work on the beam line and their cooperation with this experiment.

I thank Wyatt Brown for critically reading the final draft of this thesis.

I am grateful to the National Science Foundation and the California Institute of Technology for financial support.

A B S T R A C T

The primary objective of this experiment was to determine the Lorentz structure of the neutral current coupling -- that is, to determine what combination of V-A and V+A (or possibly S, P, and T) components make up the neutral coupling.

The experiment used the Fermilab narrow band neutrino beam to provide separated neutrino and antineutrino fluxes, each consisting of two energy bands at $\approx$55 and $\approx$150 Gev. Deep inelastic inclusive neutrino-nucleon interactions of the form

$$\nu(\bar{\nu}) + N = \mu^-(\mu^+) + \text{hadrons} \qquad \text{(CC event)}$$

$$\nu(\bar{\nu}) + N = \nu(\bar{\nu}) + \text{hadrons} \qquad \text{(NC event)}$$

were observed in an instrumented steel target-calorimeter, which measured the total energy of the hadrons produced in each event. The neutral current coupling was determined by comparing the hadron energy distributions of neutrino and antineutrino neutral current events.

An analysis of the charged-current data was carried out in order to determine the background of charged-current events with unobserved muons, and to provide a normalization for the neutral current data. Various parameterizations of the CC interaction were tested, and their effects on the neutral current analysis were studied in detail.

The neutral current analysis indicates that, if only vector and axial-vector components exist, then the neutral current coupling lies between V and V-A. A pure scalar coupling is excluded. The data have been compared to the Weinberg-Salam theory (extended to semileptonic interactions), and are in very good agreement with its predictions. Comparison of this data to the low-energy Gargamelle data indicates consistency with a scaling hypothesis.

TABLE OF CONTENTS

CHAPTER 1
INTRODUCTION

1.1 RECENT HISTORY

This thesis concerns an experiment[1] carried out by the Caltech-Fermilab neutrino group in September 1974 to determine the nature of the neutral current coupling observed in high-energy neutrino-nucleon interactions.

Before the summer of 1973, weak neutral current interactions had never been observed. The only evidence concerning their existence was negative: strangeness-changing neutral currents had been ruled out at a level of $\leq 10^{-6}$ relative to strangeness-changing charged currents[2], and low-energy experiments indicated a limit of $\leq .2$ for the neutral-current/charged-current cross-section ratio in neutrino-nucleon scattering[3].

The discovery of neutral currents therefore came as somewhat of a surprise. The observation of neutral current neutrino interactions was first announced by the Gargamelle neutrino collaboration[4] in July of 1973, and was soon after also reported by the Harvard-Penn-Wisconsin neutrino experiment[5] at Fermilab. Both experiments reported a NC/CC ratio of .2-.3.

The members of the Caltech-Fermilab experiment (including myself) had been studying only CC interactions up to that time. With the discovery of neutral currents we began planning modifications to the Caltech apparatus to make the experiment more sensitive to neutral current interactions. A preliminary run[6] in January 1974 confirmed

the existence of neutral current events at a level consistent with the initial Gargamelle results. But by this time there were several conflicting indications[3,7,8] of the structure of the NC coupling, and the nature of the neutral current interaction was not clear.

Although neutral currents had not been previously observed, their existence had been a subject of active theoretical speculation for years. The Fermi theory of the weak interaction was known to be lacking; although it agreed well with charged-current data to first order, it diverged in second order calculations. The introduction of neutral currents, however, could be made to cancel this divergence and thus give a renormalizable theory[9]. Moreover, Weinberg and Salam had created a gauge theory[10] in which the neutral intermediate boson Z_0 and the photon appeared as linear combinations of two basic gauge fields, so that the weak and electromagnetic interactions were combined in a unified, renormalizable, and exactly calculable theory. The possibility of such a unification was and is tremendously exciting.

The original Weinberg-Salam theory, which applied only to purely leptonic interactions, was extended to semileptonic interactions (including $\nu + N \rightarrow \nu +$ anything) by Glashow, Iliopoulos, and Maiani[11]. Other unified and renormalizable gauge theories were developed, and in some cases incorporated a more far-reaching unification of weak-interaction phenomena[12]. In almost all of these theories the neutral current was expected to couple through a linear combination of vector and axial-vector currents, ranging from V-A (like the charged current) to pure A or pure V (like the electromagnetic current) to pure V+A. The exact form of the predicted coupling differed in different theories. Other more exotic couplings (such as tensor, scalar, and pseudo-scalar) were also suggested[13].

After the discovery of neutral currents, the most important step needed to understand the neutral current coupling, and in particular to understand the relation between the weak neutral force, the weak

charged force, and the electromagnetic force, was the experimental determination of the space-time structure of the neutral current coupling. In this context, the Caltech-Fermilab group planned a second neutral current experiment aimed specifically at determining the structure of the neutral current coupling from the measured hadron energy distributions of neutral current events.

1.2 KINEMATIC VARIABLES IN THE INCLUSIVE INTERACTION.

Both the reactions

$$\nu(\bar{\nu}) + N \rightarrow \mu^-(\mu^+) + \text{hadrons} \qquad \text{(CC interaction)} \qquad (1\text{-}1)$$

$$\nu(\bar{\nu}) + N \rightarrow \nu(\bar{\nu}) + \text{hadrons} \qquad \text{(NC interaction)} \qquad (1\text{-}2)$$

are believed to occur through a current exchange[14] as shown in the diagram below. The inclusive interaction can be completely described in terms of the dimensionless kinematic (scaling) variables x and y and the center-of-mass energy.

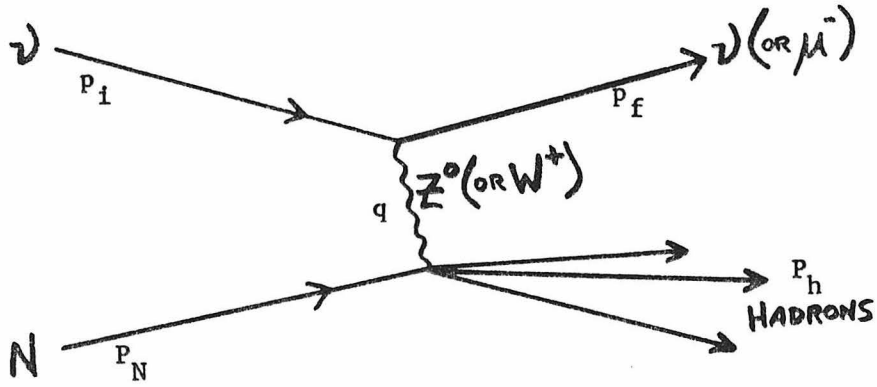

where $q = p_f - p_i$ = momentum transfer

$\nu = q \cdot P_N / M_N = E_h - M_N$ (M_N = nucleon mass)

$x = -q^2 / 2M_N \nu$

$y = 2q \cdot P_N / s = \nu / E_i^{\nu}$

The general form of the differential cross-section in the scaling limit (see Appendix A) is

$$\frac{d^2\sigma}{dxdy} = \frac{G^2 M E}{\pi} [\ Q(x) + \bar{Q}(x)\ (1-y)^2\ ] \qquad (1\text{-}3)$$

In the parton model[15], x is physically interpreted to be the fraction of the nucleon's momentum carried by the interacting parton in the infinite momentum frame. The x-dependence of the interaction therefore primarily reflects the nucleon structure, and is of secondary interest to us. The y-dependence and the consequent E_h distributions of the events reflect the structure of the coupling.

1.3 RELATION BETWEEN COUPLING AND Y DEPENDENCE.

The relation between the structure of the coupling and the y distributions can be seen most easily in the simple parton model (see Appendix B). If we assume scaling[16] of the nucleon structure functions, the Callan-Gross relation[17] (spin 1/2 partons). proton-neutron charge symmetry[14], and a pure V-A coupling, then the differential y-distributions for CC events have the form

$$\frac{d\sigma^{\nu}}{dy} = \bar{E} [\ (1-\alpha) + \alpha\ (1-y)^2\ ] \qquad (1\text{-}4a)$$

$$\frac{d\sigma^{\bar{\nu}}}{dy} = \bar{E} [\ \alpha + (1-\alpha)\ (1-y)^2\ ] \qquad (1\text{-}4b)$$

where $\bar{E} = \frac{G^2 M E}{\pi} \int_0^1 F_2(x)\, dx$, and α is the fractional antiparton component in the nucleon (expected to be 5 - 10%)[18,19]. The dominantly flat distribution for ν events and $(1-y)^2$ for $\bar{\nu}$ are a consequence of V-A coupling and the negative helicities of the scattered partons (see Appendix B).

Predictions of gauge theories, as well as the analogy to charged and electromagnetic current couplings, strongly suggest that the neutral current couples through a combination of V and A (other couplings are possible and will be considered later, but for the time being we will ignore them). In this case, the neutral current distributions are similar in form to the charged current distributions:

$$\frac{d\sigma^{\nu}}{dy} = \overline{E}\, g_{nc} \left[(1-P) + P\,(1-y)^2 \right] \qquad (1\text{-}5a)$$

$$\frac{d\sigma^{\overline{\nu}}}{dy} = \overline{E}\, g_{nc} \left[P + (1-P)\,(1-y)^2 \right] \qquad (1\text{-}5b)$$

P, analogous to α in equations (1-4), is a "positive-helicity parameter", which receives contributions from <u>both</u> a) V-A coupling to antipartons, and b) V+A coupling to partons. If the neutral current coupling is V-A (like the CC coupling), then P in equations (1-5) is equal to α. If the coupling is pure V+A, $P = 1 - \alpha$; and if the coupling is pure V or pure A, then $P = 1/2$ (see Appendix B for more detail).

Note that the structure of the neutral coupling affects only P, while the strength of the coupling determines g_{nc} (measured relative to the CC coupling). The determination of P was therefore the most central aim of this experiment.

Since P alone determines both the shapes and the relative magnitudes of the ν and $\overline{\nu}$ y-distributions, these could be used to experimentally determine P. However, the y-distributions of NC events could not be measured directly since the energy of the incident neutrino could not be measured directly. Instead, we have used the hadron energy distributions of NC events ($E_h = y\,E_\nu$) produced by interactions of a narrow band neutrino beam, since E_h is the measurable quantity most directly related to y. The plan of the

experiment was therefore to measure the E_h distributions of neutral (and charged) current events for ν and $\bar{\nu}$ interactions separately, and then to use both the shapes and the relative magnitudes of these distributions to extract P.

1.4 OUTLINE OF PRESENTATION.

The formation and characteristics of the narrow band neutrino beam used in the experiment are discussed in Chapter 2. Chapter 3 gives a physical description of the apparatus used to detect and measure neutrino events, and describes the method used to calibrate the target-calorimeter which measured the hadron energy of the events. The techniques of event analysis and the method of separating NC and CC events are discussed in Chapter 4.

The actual data analysis begins with Chapter 5. Various sources of background in the experiment and possible biases and errors in event identification are discussed here, as well as the corrections and cuts used to minimize them. Chapter 6 is devoted to the analysis of the charged-current events, and various models -- both scaling and non-scaling -- are compared to the data. The analysis of the neutral current data is presented in Chapter 7; the best values of P and g_{nc} are calculated and compared to the possible V and A coupling schemes (including the Weinberg-Salam model). More general coupling schemes and possible deviations from a linearly rising NC cross-section are considered in Chapter 8.

The most basic conclusions of the experiment are summarized and reviewed in Chapter 9.

CHAPTER 2
THE NARROW BAND NEUTRINO BEAM

2.1 ADVANTAGES OF THE NARROW BAND BEAM

In order to determine the nature of the neutral current coupling, it is essential to be able to separately measure neutrino and antineutrino neutral current cross-sections. But it is impossible to tell from the final state hadrons produced by a neutral current interaction whether the event was produced by a neutrino or by an antineutrino; this information must be obtained from a knowledge of the incident neutrino flux. It is essential to use a neutrino beam with good "sign selection" -- i.e., one that can be tuned to produce only neutrinos or only antineutrinos -- so that neutrino and antineutrino interactions can be clearly separated.

It is also important to have a good understanding of the incident neutrino spectrum and for this spectrum to be as simple as possible. Since the final state neutrino carries away undetected energy, only the energy of the hadron shower is measured in neutral current events. It is impossible to tell whether a given interaction is due to a high-energy incident neutrino interacting with low y, or a lower energy neutrino interacting with larger y.

Since there is such limited information available from the final state products of a neutral current interaction, the kind of neutrino beam used is extremely important. The ideal neutrino beam would be both sign-selected and monoenergetic. The closest approximation to this, in practice, was the Fermilab narrow band beam[20,21,22].

In the Caltech-Fermilab neutral current experiment, the narrow band neutrino beam was formed by targetting the 300 Gev Fermilab proton beam to produce secondary pions and kaons. These secondaries were sign- and momentum-selected to form a parallel beam of 170 Gev central momentum. This beam was directed down a 350-meter evacuated decay pipe, where $\pi(K) \rightarrow \mu + \nu$ decays provided the neutrino flux. The decay pipe was followed by 500 meters of earth and steel shielding, so that all the hadrons and almost all the muons were absorbed, and only the neutrinos reached the detection apparatus. The resulting neutrino spectrum was composed of two bands: a low energy band ($\approx$55 Gev) from pion decays and a high-energy band ($\approx$150 Gev) from kaon decays.

The narrow band beam had several additional advantageous features. The beam was tuned to a high energy, and the neutrino spectrum at the apparatus was consequently peaked at high energy. In contrast, the production spectrum from a bare target is peaked at low energy. Since high energy CC events tend to produce higher-energy and more forward muons, the high-energy fluxes made it easier to identify CC events and to separate them from NC events. It was also much easier to trigger on and identify high-energy NC events, since very small hadron showers were difficult to detect. In addition, a comparison of the calculated two-band structure of the beam to the measured total energy distributions of CC events also provided a check on energy resolutions in the detector.

There were two serious problems associated with the beam. Normalization of the secondary fluxes was not known very well and could not be easily monitored. This made it impossible to externally determine the flux normalization, and the observed CC events had to be used for this purpose. Secondly, there was a significant "wide-band background", produced by hadrons which decayed before the momentum selection. This background was not sign-selected, and was peaked at low energies. It was directly measured, as described below, but at the cost of a significant amount of running time. These problems are not peculiar to the narrow band beam, of course, and are much worse

for a beam with poorly defined momentum and sign selection.

2.2 FOCUSING SYSTEM

Both the focusing system and the neutrino flux produced are discussed in detail elsewhere[21,22], so only a brief description will be given here.

A schematic of the focusing system is shown in figure 2-1. The quadrupoles Q_f (focusing horizontally and defocusing vertically) and Q_d (focusing vertically and defocusing horizontally), together with the dipoles D1-3, are tuned to form a point-to-parallel focusing system. The width of the momentum-slit aperture determines the width $\Delta P/P$ of the transmitted beam. The part of the primary proton beam which does not interact in the target is absorbed by the beam dump. The direction of the final hadron beam is adjusted by horizontal steering magnets T_h at the downstream end of the system, and is monitored by a counter at the downstream end of the decay pipe.

Ideally, one would like to have an intermediate focus at the momentum slit (point-to-point-to-parallel focusing) to give maximal acceptance for minimal $\Delta P/P$. This is not possible with conventional magnets in the limited space available, and therefore a reduction in momentum acceptance costs heavily in rate. It is impractical to try to reduce the momentum acceptance below $\Delta P/P$ = 10%.

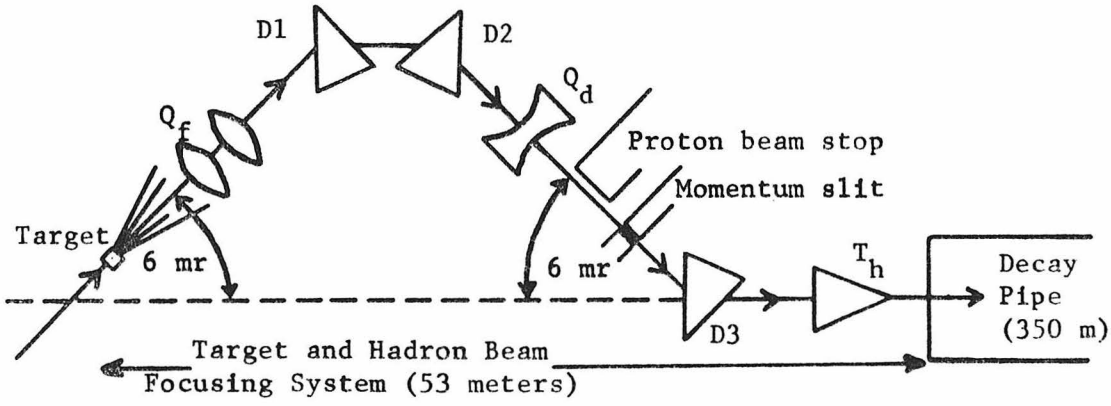

Figure 2-1: Schematic of Narrow-Band Focusing System.

The system was tuned in this experiment to transmit a central momentum of 170 Gev, with $\Delta P/P$ (HWHM) = 15%. The dipoles were calibrated before being installed, and both dipole calibration and magnet alignment were checked by steering the primary proton beam through the system and measuring its position at the beam dump as a function of dipole current.

Both the momentum spectrum and the spatial shape of the beam are insensitive to changes in quadrupole focusing, collimator position, and size of the proton beam at the target. The momentum is determined primarily by the dipoles and momentum slit aperture, and the angular divergence is determined primarily by the apertures of the downstream dipoles (used for steering). The overall acceptance, however, is sensitive to the quadrupoles, collimators, and spot size.

2.3 NEUTRINO SPECTRUM

The neutrino spectrum resulting from $\pi, K \rightarrow \mu + \nu$ consists of two bands, ranging from approximately 20 to 70 Gev (ν_π) and from 120 to 160 Gev (ν_K). The difference between the bands stems from the difference in parent masses: if a particle of mass m_p and energy E_p decays into $\mu\nu$, then the neutrino energy is given by

$$E^\nu = \frac{m_p^2 - m_\mu^2}{m_p^2} \frac{1}{1 + (\theta \cdot E_p / m_p)^2} \equiv E^\nu_{max} \frac{1}{1 + (\theta \gamma_p)^2} \qquad (2\text{-}1)$$

where θ is the angle in the lab between the ν and the parent particle. The highest energy ν's are those emitted in the forward direction (with $E^\nu = E^\nu_{max}$). Neutrinos from K-decay are higher in energy than those from π-decay due to the higher parent mass. With a 170 Gev parent beam, $E^\nu_{max} = .43 \cdot E_p = 70$ Gev for ν_π, and $E^\nu_{max} = .96 \cdot E_p = 160$ Gev for ν_K.

The neutrino spectrum at the detector apparatus, shown in figure 2-2, was calculated by ray-tracing secondary hadrons through the focusing system, weighting each hadron by the predicted

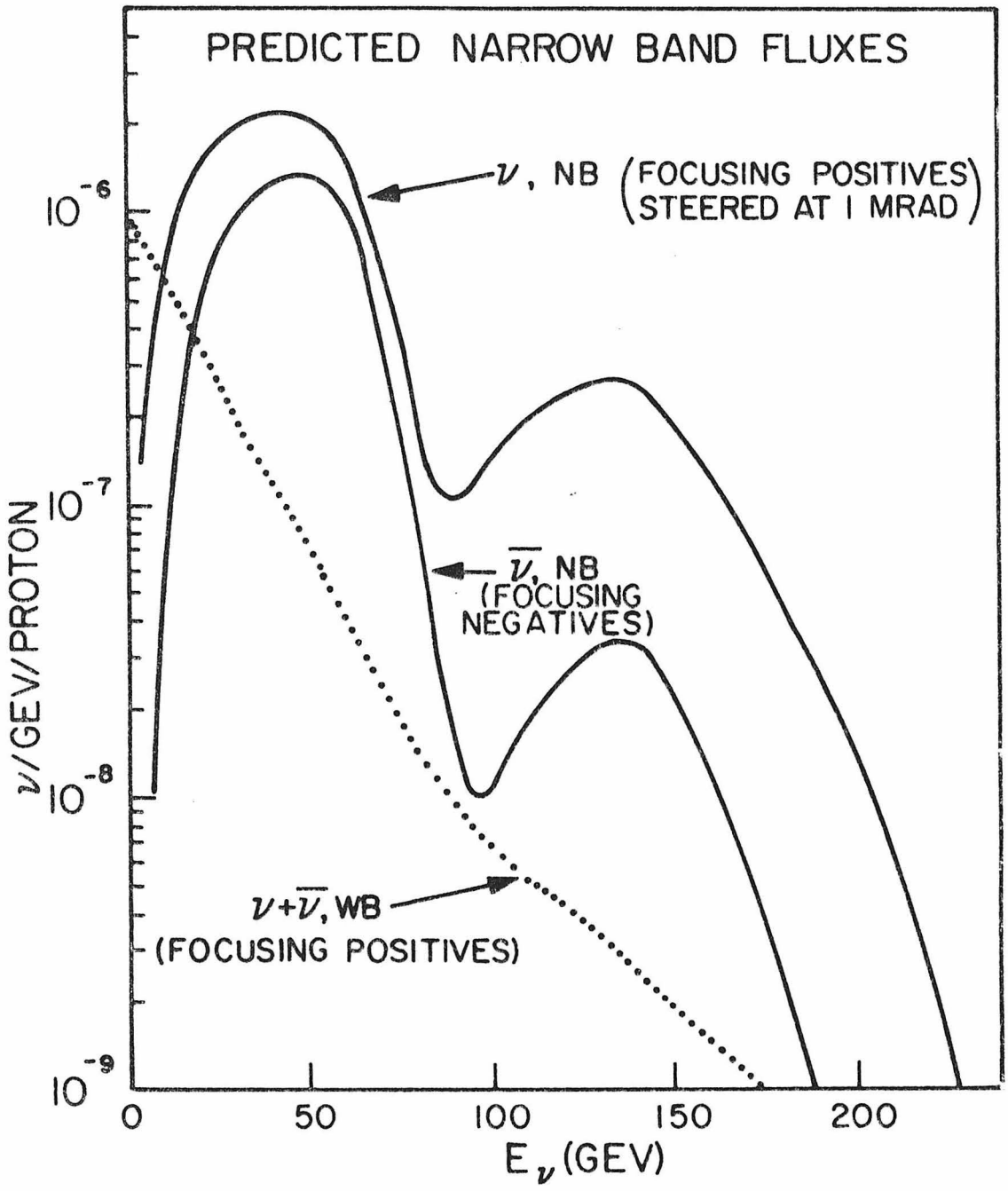

Figure 2-2: The narrow band flux spectra expected at the detector for both ν (positive secondary beam) and $\bar{\nu}$ (negative beam). Note that the two peaks from π- and K-decay dominate the spectrum at high energy, but the wide-band background dominates at low energy. The calculation used Hagedorn-Ranft flux predictions with adjustments in normalization based on earlier beam studies[21].

Hagedorn-Ranft[23] production spectrum at the proton target, and analytically calculating the neutrino flux from each secondary decay (normalization of these fluxes is discussed in section 2.5). Since the neutrino flux at the apparatus varied with transverse position, the flux was calculated as a function of the transverse spatial coordinates x and y, as well as of E^{ν}.

2.4 STEERING OF THE BEAM

In addition to the difference in energy, the ν_{π}'s also differed from the ν_K's in angular distribution. The ν_{π}'s, emitted with smaller transverse momentum, tended to be emitted at smaller lab angles than the ν_K's, and therefore lay in a narrower peak at the detector (see figure 2-3).

In the neutrino data, the beam was steered 1 mrad away from the center of the apparatus to take advantage of this difference. The flux at the apparatus, as a result, had two useful features: 1) the average neutrino energy was higher than it would have been for straight-ahead data, since the lower-energy ν_{π}'s were less dominant; 2) the ν_K/ν_{π} (or high-energy/low-energy) ratio varied across the apparatus, so a strong energy dependence in the neutral current

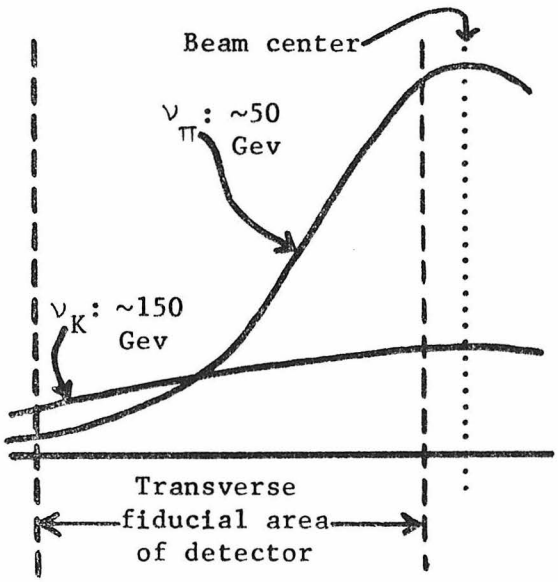

Figure 2-3:
Beam profile at detector, with hadron beam steered 1 mrad away from center. Since ν_K component is much broader than ν_{π}, both ν_K/ν_{π} ratio and mean beam energy at detector are higher than for straight-ahead steering.

cross-section, if it existed, should have been more apparent. In antineutrino data taking this was not attempted since the $\bar{\nu}_K$ flux was too small relative to the $\bar{\nu}_\pi$ flux.

2.5 FLUX NORMALIZATION

Due to uncertainties in the calculated normalization, the Hagedorn-Ranft flux spectra mentioned previously were used only for spectral shape of the secondary fluxes and not for normalization. Instead, the ν_{π^+}, ν_{K^+}, $\bar{\nu}_{\pi^-}$, and $\bar{\nu}_{K^-}$ fluxes were determined from the observed CC events -- i.e., the charged current data were used to normalize the neutral current data.

A more direct determination of fluxes would have been preferable. But flux measurements are in general one of the most difficult problems of neutrino experiments, and were particularly difficult in this one. Previous Caltech-Fermilab measurements[19,21] of the CC cross-section used a slow-spill extracted proton beam with a spill time of ~1 sec. A neutral current trigger must be very unrestrictive, however, since there is no final state muon to trigger on. The only signature of an event is the hadron shower, and the experiment had to be sensitive to low-energy showers (see section 3-5). Backgrounds from cosmic rays were consequently high, and would have been intolerable with a 1-second beam gate. For this reason a fast-spill proton beam was used with a spill time of 400 μsec. This made it impossible to count individual particles in the decay pipe, and the high instantaneous rates caused saturation problems with some of the existing monitors.

Even if the total beam intensity could have been monitored well, a complete survey of the secondary beam, including measurement of π / K / p ratios under the beam conditions used, would have been necessary to determine normalization. This would have required considerable extra beam time and significant improvements in monitoring (see reference [21]).

We have also attempted to directly calculate the fluxes. But the calculation of the acceptance of the focusing system requires a rather sophisticated Monte-Carlo program, and is sensitive to magnet and collimator alignments, quadrupole settings, and beam size at the target, for example. In addition, the production spectra of secondary π's and K's have not been measured very precisely at the beam energies used in this experiment[21]. The resulting errors in normalization are >50%.

For these reasons, and in order to make the analysis as empirical and self-contained as possible, we have used the rate of observed CC interactions to determine the neutrino fluxes used in the analysis of neutral current interactions.

2.6 WIDE BAND COMPONENTS

In addition to the two energy bands described above, there were some unwanted background components in the neutrino flux. The largest of these was the "wide band background" (see figure 2-2), due to decays of π's and K's which occurred before the beam was momentum selected (i.e., between the proton target and the momentum slit). This background was reduced by targetting the proton beam at a 6 mrad angle (see figure 2-1) so that the secondaries were directed away from the apparatus before being momentum selected. Nevertheless, the hadron flux near the target was much larger than that in the decay pipe, and the wide band background from wide-angle decays was therefore sizable. This was particularly true in the antineutrino running, since the beam consisted of π^- and K^- decays only, while the background included neutrinos from the much more numerous π^+ and K^+ decays.

The wide band background was a potential problem for several reasons. It was predominantly low-energy due to the 6 mrad targetting angle, the larger low-energy fluxes, and the higher probability of decay of low-energy hadrons. As discussed later, the muon detection

efficiency of charged current events was worse at low energy, and therefore CC events were harder to distinguish from NC events. Furthermore, the events originating from the background were not well-defined in energy, so the wide band background compromised some of the major advantages of the narrow band beam. Finally, the wide band was predominantly composed of neutrinos from π^+ and K^+ decays (since the π^+ and K^+ fluxes were much higher than π^- and K^-), and therefore constituted a large wrong-sign background in the antineutrino running. Since the separation of ν and $\bar{\nu}$ NC cross-sections was crucial to the experiment, it was essential to eliminate this background.

The wide band background can be estimated from production models such as the Hagedorn-Ranft model (as shown in figure 2-2), but there are large uncertainties in normalization. It is particularly difficult to calculate the effect of the thick target (12" of aluminum) on the produced hadron spectrum at low energy. Interactions of the secondary beam in the collimators and magnets immediately after the target could also produce a significant component. Even more important, and more uncertain, are collisions of the primary proton beam (and its halo) with any material such as monitors, collimators, or magnets. Such interactions, particularly those occurring well upstream of the target, could produce a significant background since the π's and K's produced could have a long decay path.

Due to these uncertainties, we have not attempted to use calculated wide-band backgrounds, but instead have directly measured this component of the flux. This was done by running the experiment almost a third of the time with the momentum slit closed, so that only wide-band background was observed. The closed-slit backgrounds measured in this way were subtracted from the ordinary open-slit data.

There are other possible sources of wide-band background, such as decays of π's and K's in the proton beam dump. In principle, there could be sources of direct neutrino production or even production of a

new particle (such as a heavy neutrino) in the target and beam dump. Reasonable estimates of these sources indicate that they should be quite small (<1%), but it is difficult to set firm limits. In any case, all of these sources are included in the closed-slit subtraction and therefore cannot contribute to the observed narrow-band signal. The closed-slit subtraction insures that the observed signal originates from decays occurring after the momentum slit and thus well downstream of the target and beam dump.

2.7 ELECTRON NEUTRINO COMPONENT

Another contamination in the beam was the electron neutrino flux. Since electron neutrino interactions produced no final state muon, and since the electromagnetic shower from the produced electron could not clearly be distinguished from the hadron shower, ν_e interactions looked very much like NC interactions in the detection apparatus.

The primary source of ν_e's was K_{e3} decays (see figure 2-4). At very low energies, $\mu^+ \rightarrow e^+ \nu_e \bar{\nu}_\mu$ decays occurring both within the decay pipe and in the shielding following the decay pipe contributed more, but the total signal was strongly dominated by K_{e3}. This background could be reliably calculated from the K_{e3} branching ratio (4.82%) and the kaon flux. Since the K^- fluxes were small, this background was significant only for neutrino and not antineutrino data.

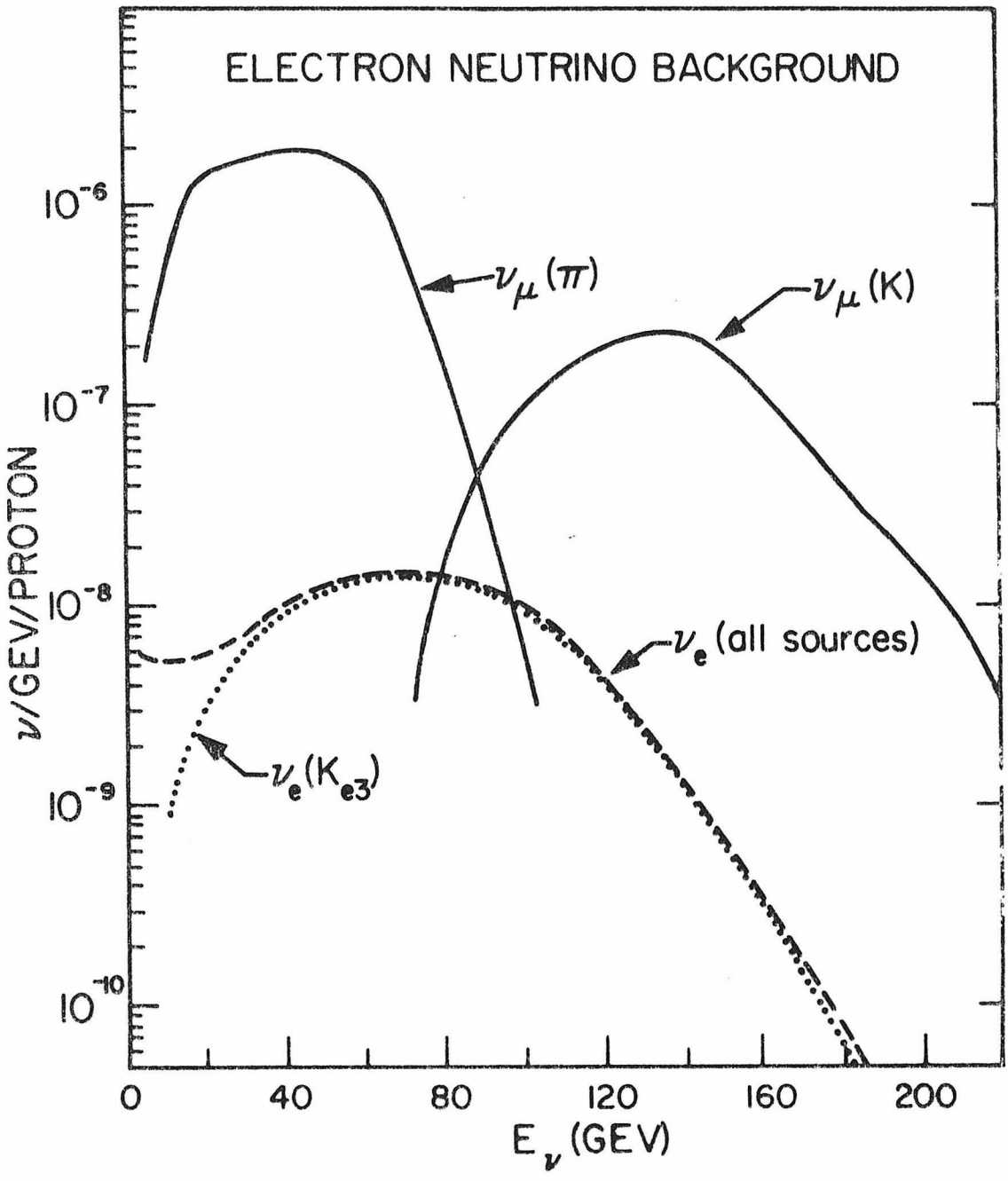

Figure 2-4: The total electron-neutrino flux is compared to the total muon-neutrino flux (ν_μ^π and ν_μ^K are shown separately). The most important contributor is the decay $K^+ \longrightarrow \pi^0 e^+ \nu_e$, but $\mu^+ \longrightarrow e^+ \nu_e \bar{\nu}_\mu$ is also important for low-energy ν_e.

CHAPTER 3
APPARATUS

3.1 BRIEF GENERAL DESCRIPTION

A neutrino detector for neutral currents must meet several fundamental requirements. It needs to contain a massive target to produce a reasonably high event rate. It must allow good muon identification to differentiate between NC and CC events. Since high-energy muons and hadrons are distinguished only by their penetration through matter, there must be a dense material to absorb the hadron shower and thus allow identification of the penetrating muon. The target must be instrumented to measure the position of charged particles near the interaction, not only to identify the muon but also to identify a neutrino event and measure its interaction position from the hadrons alone (since only the hadrons are detected in neutral current events). It must provide a good measurement of the total hadron shower energy, since this is the only physics quantity measured for a neutral current event. Finally, it must be triggerable by the hadron shower alone so that there is no trigger bias in favor of CC events over NC events.

In the Caltech apparatus[24], these requirements were met by constructing a dense target-calorimeter, which contained spark chambers and liquid scintillation counters sandwiched between steel plates throughout the length of the calorimeter (see figure 3-1). The calorimeter was approximately 48 feet long and 5' by 5' in transverse dimensions; it contained a total of 35 spark chambers, 70 counters, and 143 tons of steel. The steel provided the mass necessary for a

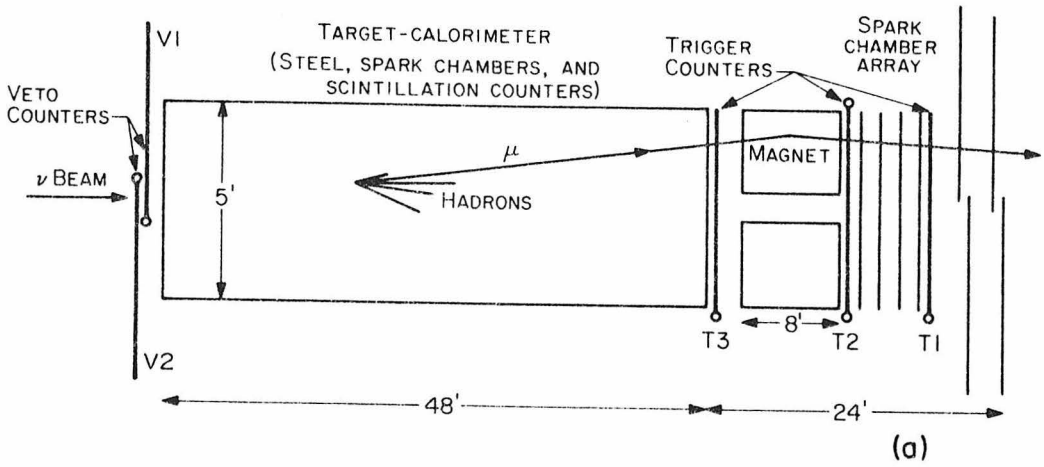

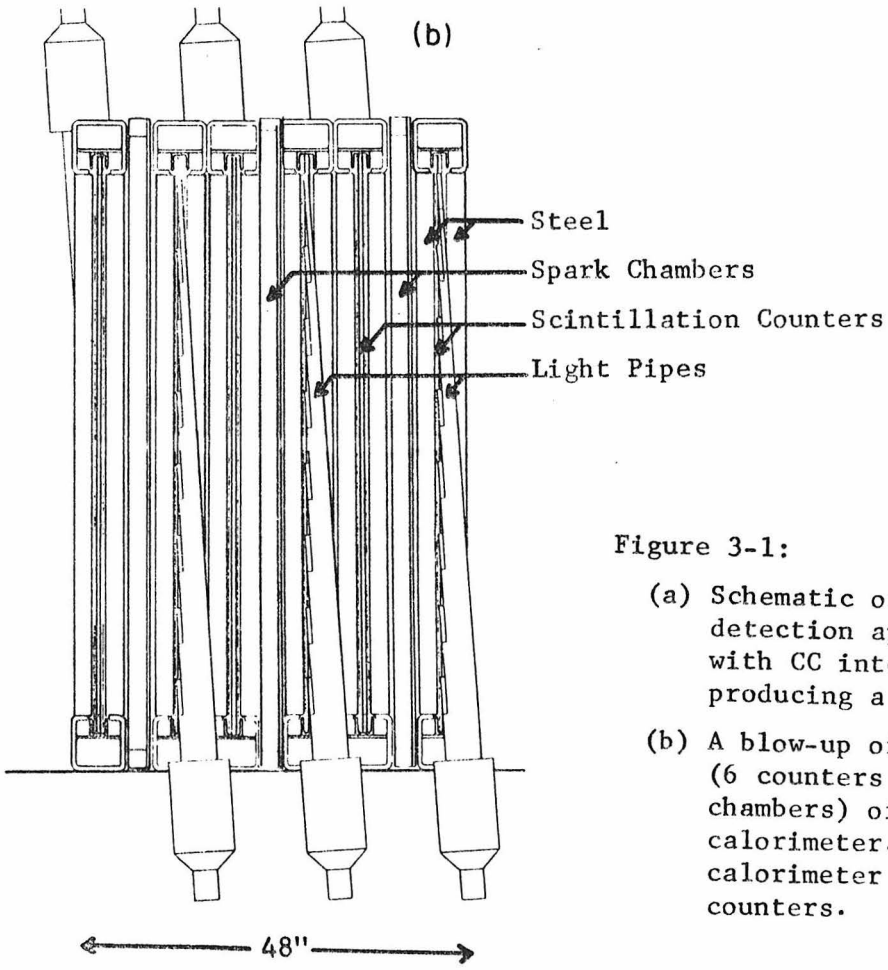

Figure 3-1:

(a) Schematic of neutrino detection apparatus, with CC interaction producing a forward muon.

(b) A blow-up of one module (6 counters and 3 spark chambers) of the target-calorimeter. The entire calorimeter contains 70 counters.

sufficiently high event rate, and also developed and absorbed the hadron shower produced by a neutrino interaction. The total energy of the hadron shower was measured by the scintillation counters, which sampled the energy of the hadron cascade after every 4" of steel. A spark chamber after every second counter measured the transverse position of the interaction.

For CC events, the muon production angle was also measured by the spark chambers in the calorimeter. The energies of forward muons were measured by a spectrometer, consisting of a toroidal iron-core magnet followed by a spark chamber array, immediately downstream of the calorimeter.

The apparatus was triggered in either of two ways: (1) by a muon passing through the trigger counters T1, T2, T3 (for CC events only), and (2) by a hadron cascade of total energy $E_c > 12$ Gev as measured by the calorimetry counters (for both CC and NC events). The veto counters V1 and V2 at the upstream end of the calorimeter vetoed charged-particle triggers (primarily due to muons which penetrated the shielding).

3.2 COUNTERS: PHYSICAL DESCRIPTION

The counters were made from plexiglas boxes, 72" by 64" by 1", and contained liquid scintillator in a 60" by 60" by 1/2" volume. A pseudo-cumene based scintillator (mixed with mineral oil to reduce cost) was used in the counters, yielding a signal of 6-8 photoelectrons per single ionizing particle (a typical hadron cascade of 20 Gev gave a signal equivalent to about 100 single ionizing particles). The light output was therefore easily sufficient for calorimetry.

The use of liquid scintillator did present a problem, however, since the pressure from a 5' head of scintillator was sufficient to make the counter bulge (and even break) near the bottom; but to have

uniform light production over the counter, the distance between counter walls had to be uniform. To prevent bulging due to the scintillator pressure, each empty counter was wrapped between two polyethylene water bags, which covered the 5' by 5' sides, and was then placed between two 2" thick steel plates which were joined together to form a sandwich with the counter in the middle (see figure 3-1(b)). The counter and water bags were simultaneously filled, so that the pressure on the sides of the counter was always equalized. As an additional precaution, the walls of the counter were reinforced with twenty-five 1" spacers which bridged the gap between the walls and prevented damage to the counters if the water bags had broken or leaked.

Light was collected by a plexiglas light pipe on one side of the counter and channelled into a 5" RCA-4525 phototube (see figure 3-1(b)). The light pipes were composed of 8 independent arms, each of which ended in a flat 4" by 1/2" surface which was optically connected to the end of the acrylic box. Light entering the pipe was bent by a 45 degree mirror down the long straight section. Since less light was transmitted by the longer arms due to attenuation, the shorter arms were partially masked with black enamel at the counter to admit less light. This resulted in a light collection efficiency which was uniform to within 8% from the top to the bottom of the counter.

The side of the counter opposite the light pipe was covered by a mirror to give more uniform response across the counter. The resulting attenuation across the counter is shown in figure 3-2(a). Systematic effects due to this attenuation were reduced by alternating the sides on which the light pipes were placed, so that the nth counter had the light pipe on the right and the (n+1)th counter had it on the left. The average calibration of a pair of adjacent counters was then much more uniform, as shown in figure 3-2(b). The remaining x-dependent variations were corrected in the analysis by using position information from the spark chambers.

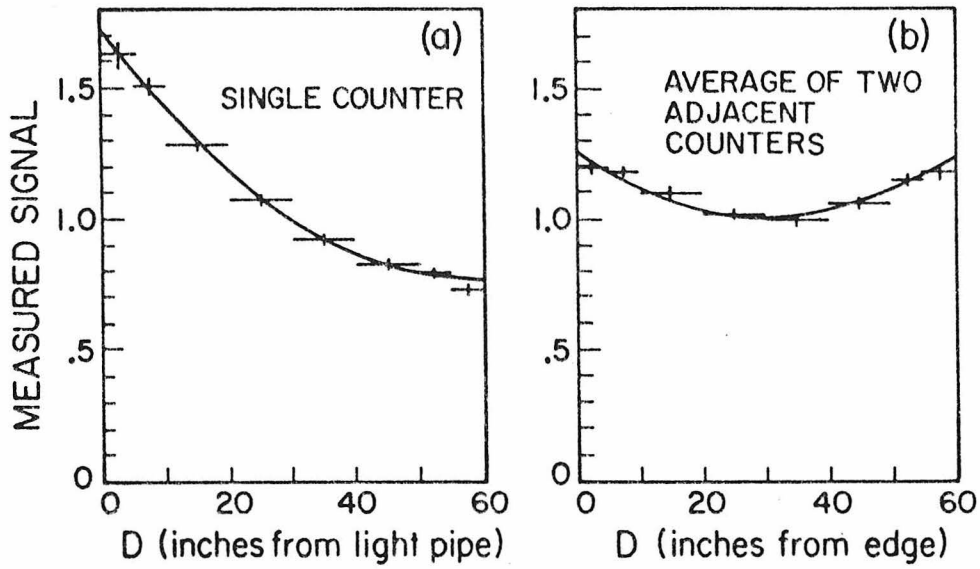

Figure 3-2: (a) The variation in light output of a single counter due to attenuation is plotted as a function of the distance between the ionization source and the light pipe.
(b) Adjacent counters have their light pipes on opposite sides, so the attenuations tend to cancel when the two outputs are summed.

3.3 ANALYSIS OF COUNTER SIGNALS

The signals from the calorimetry counters were used for hadron energy measurement, triggering, muon detection, and calibration of the calorimeter. All except the first of these required good sensitivity to single-particle signals, but hadron showers produced total signals over the range from 1 to 1000 times greater. To cover such a wide range, the counter signals were handled in several different ways.

The high voltage on the counters was adjusted to give a signal of about 3 mv for a single-particle signal; a typical hadron shower produced signals on the order of .1 volts in a single counter. Each phototube was connected to an amplifier which produced both unamplified outputs and outputs amplified by a factor of ~30. The amplified signals were used for calibration and for trigger logic, and the unamplified outputs were used for hadron energy measurement.

The first unamplified output went to a mixer, where the two counters in each odd-even pair were added to form an input for a pulse-height analyzer. Since there were 70 counters, there were 35 PHA signals; these were the basic signals used for the measurement of hadron energy and shower development. Each PHA covered a total range in shower energy of 0 to ~40 Gev.

The second unamplified output was connected to a 6-fold mixer. There were 11 such units (counters 1-4 had no output of this kind), each mixing 6 consecutive counters which formed a trigger module. These "module signals" were primarily used in the hadron trigger (described later).

In addition, the module signals were attenuated by a factor of 50 and then pulse-height analyzed to supplement the ordinary unamplified signals. If a hadron shower saturated one or more of the PHA's, then the attenuated module signals, which never saturated, were used to measure the hadron energy. In addition, comparing the sum of the ordinary single signals to the module signal gave a continuous monitor of the PHA's and mixers.

The amplified outputs were used for measuring energy deposition on the order of 1 single-ionizing particle. The first output determined whether a signal of at least one single-ionizing particle was observed in the counter, and was used to define the region of interaction in the apparatus. The second output was used only for calibration of the counters (described below).

The counters were monitored continually during the running period with light-emitting diodes which were inserted into the counters on the side opposite the light pipe. These were set to provide a signal equivalent to about 30 Gev for each counter. The LED's were automatically pulsed, usually after every 10th beam cycle, and provided a check on the stability of each counter's signal at the 10% level. The pedestal levels of the PHA's were automatically monitored in a similar fashion.

3.4 CALIBRATION OF THE CALORIMETER

The counters were calibrated by turning off the veto counters and using the single-ionizing signals produced by muons which penetrated the shielding and the calorimeter. The amplified phototube signals were used for this calibration. The beam was run at the highest energies possible in order to get sufficient muon flux, and only energetic muons (which didn't stop in the calorimeter) were used. Since the muon flux was spread over the apparatus, the response of the counters could be measured as a function of position, and in fact this is how the attenuation curves in figure 3-2 were measured.

Each muon produced an average of about 6-8 photoelectrons per counter, so the single-ionizing signal was not sharply peaked (see figure 3-3(b)). However, with enough events, it was possible to calibrate the counters to good accuracy. The fit in figure 3-3 assumes a modified Poisson distribution for the single-ionizing signal; the peak and width of the curve were adjusted to give the best fit. A small contribution from delta-ray production, which gave a second peak at twice the single-ionizing peak with 12% probability, was also included. All corrections for attenuation across the counter were included.

This calibration allowed the measurement of hadron shower energy only in terms of equivalent single-ionizing signals. However, all the energy in a hadron shower is not observed[25], since much of it goes into nuclear fragments, stopping or decaying particles, etc. In order to determine an absolute calibration in Gev, it was necessary to measure the total observed signal, in terms of single-ionizing particles, produced by a hadron shower of known energy. But it was impossible to move the 143 ton calorimeter into a hadron beam for a direct calibration.

Instead, a smaller version of the calorimeter was built with the same sampling density (one counter after every 4" of steel). This "test calorimeter"[26] contained 14 counters and 56" of steel, and

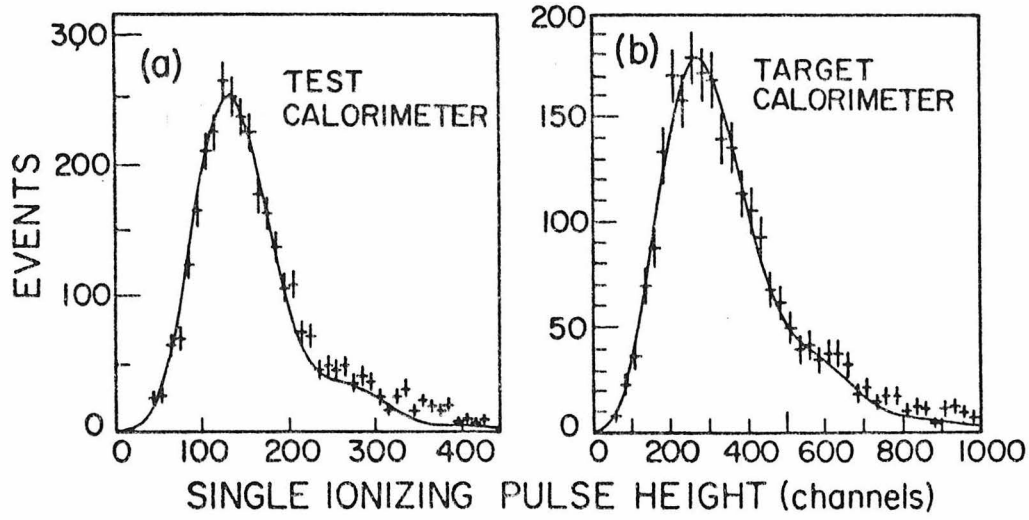

Figure 3-3: Comparison of the single-ionizing muon signals obtained from the two calorimeters. These distributions were used to measure the relative calibrations of the two calorimeters.

measured 10" by 14" in transverse dimensions and 70" in length. It was thus large enough to contain the shower but small enough to be mobile (unlike the target calorimeter). It was placed in a momentum-selected hadron beam of variable and well-defined energy for calibration.

The test calorimeter used the same electronics as the target calorimeter, and was calibrated with straight-through muons in the same way as the target calorimeter. Since different scintillator was used in the smaller calorimeter, there were more photoelectrons per single-ionizing particle and the single-ionizing peak was somewhat better defined (see figure 3-3(a)). The same type of Poisson fit was used for both figures 3-3(a) and (b), but the number of photoelectrons per single ionizing particle was fit separately. A comparison of the single-ionizing signals in the two calorimeters gave a relative calibration good to about $\pm 8\%$.

There was a small difference in the muon energy deposition in the two calorimeters due to the relativistic rise in dE/dx. The muons used to calibrate the test calorimeter were part of a 50 Gev momentum-selected beam, but the ones used to calibrate the target calorimeter had a much broader spectrum with a mean energy of ~20 Gev. This difference caused an estimated shift of $\leq 4\%$ in relative calibrations.

In both calorimeters, the hadron shower energy was measured by summing the pulse-heights, in units of single-ionizing particles, of the 14 counters downstream of the interaction. This length (56" of steel) was sufficient to contain essentially all of the shower at all energies up to and including the beam energy of 170 Gev. The average shower development at two different energies is shown in figure 3-4.

The single-ionizing equivalent of the shower, as well as the resolution, were measured in the test calorimeter as a function of incident beam energy. Histograms of the measured signal for various beam energies are shown in figure 3-5. In general, the calibration was approximately linear with a slope of 5.4 single-ionizing particles/Gev, and the fractional resolution varied as $E_h^{-1/2}$. The best fits obtained for calibration and resolution are (see figure 3-6)

$$T = \frac{5.43\ E_h^2}{E_h + .72} \tag{3-1}$$

$$\frac{\Delta T}{T} = \frac{1.11}{\sqrt{E_h}} \tag{3-2}$$

where T is the total signal in terms of single-ionizing particles.

This calibration technique assumes that the calibration for neutrino-induced showers is the same as for hadron-induced showers. There could be a small difference between these. In particular, π^0's produced at the vertex decay immediately and produce electromagnetic

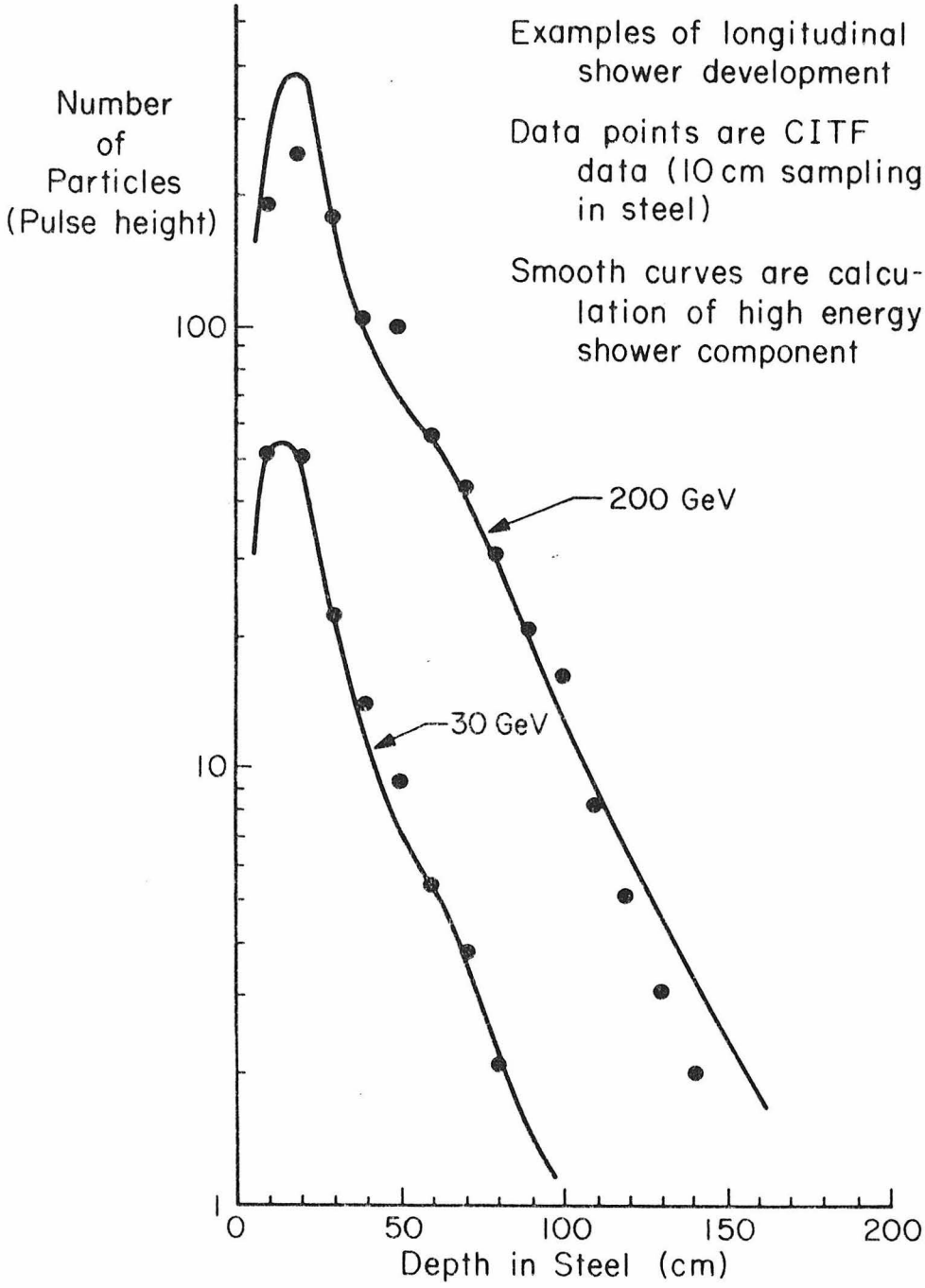

Figure 3-4: Hadron shower development measured in the test calorimeter as compared to Monte-Carlo predictions. (10 cm of steel = 1 collision length = 1 counter)

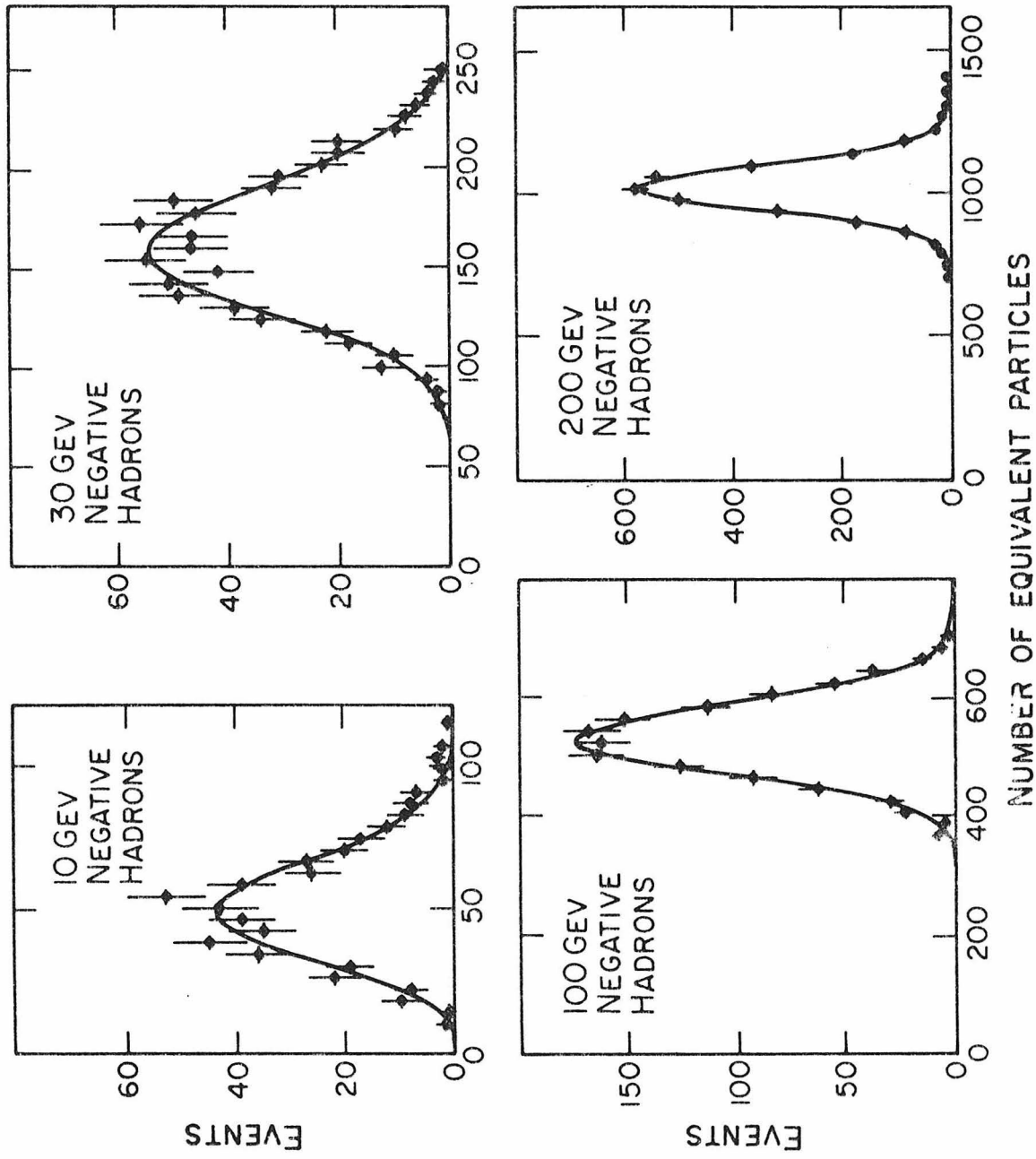

Figure 3-5: The hadron energy distributions, expressed in terms of the number of equivalent single-ionizing particles, measured in the test calorimeter at various hadron beam energies. Note that the distributions become narrower and more Gaussian as the beam energy increases.

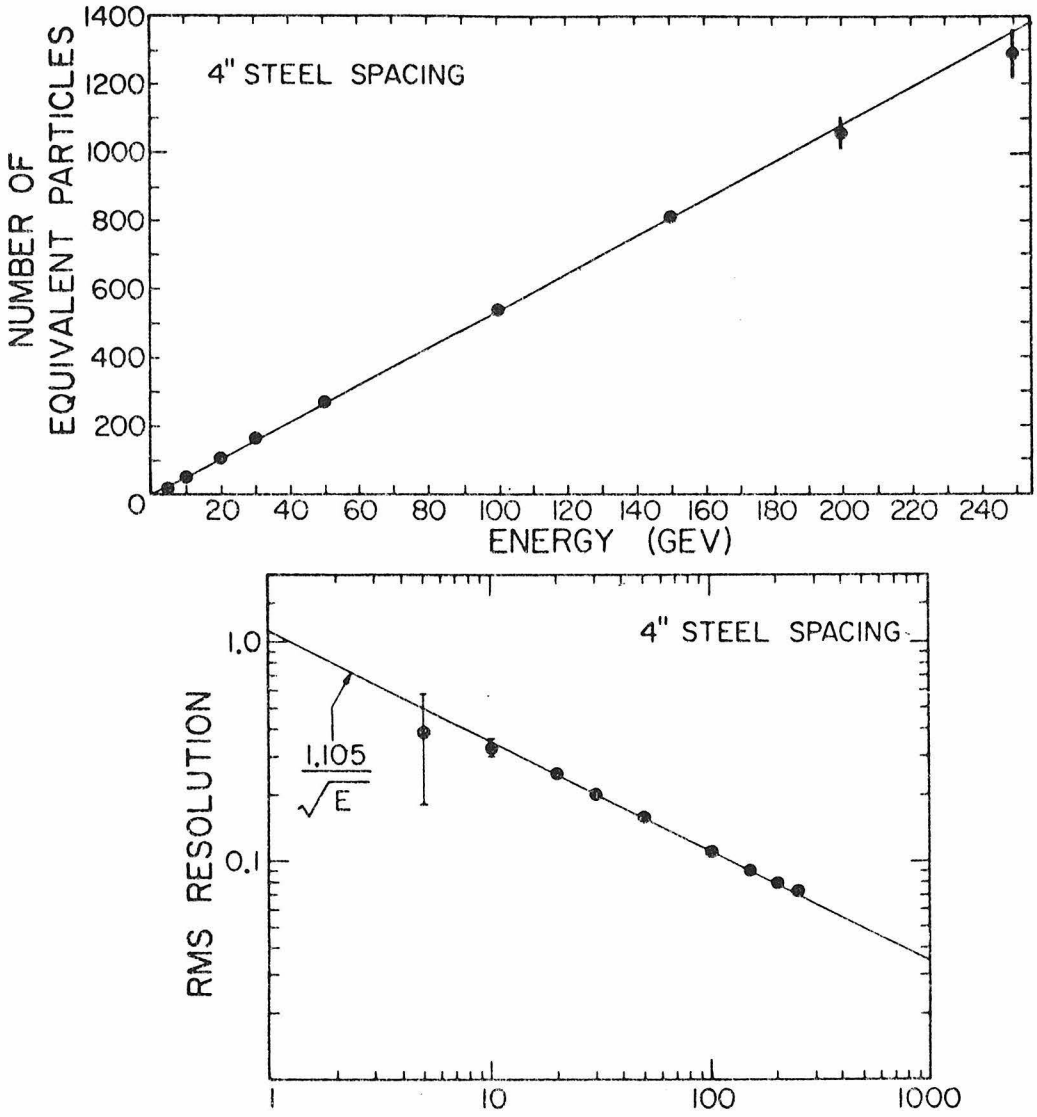

Figure 3-6: Hadron energy calibration and resolution measured in test calorimeter. Hadron energies in the neutral current experiment ranged from 12 to 180 Gev, with most showers in the 12 - 60 Gev range.

showers. The calibration of electromagnetic showers is about 30% higher than that of hadronic showers, since no energy is lost in nuclear fragments. If the relative π^0 component of neutrino-induced showers were different from that of hadron induced showers, there could be a difference in calibration. However, recent bubble-chamber studies[27] of high energy neutrino interactions indicate that neutrino-induced and hadron-induced showers are similar.

There are a few other minor differences between showers in the target calorimeter and test calorimeter. For example, the showers produced by neutrino interactions are in general produced at an angle with respect to the beam direction. This does not affect the calibration, since the shower passes through the same relative amounts of steel and scintillator, but the resolution is slightly worse due to the coarser sampling. This and similar small effects were included in the analysis, and are discussed in reference [28]. A broader discussion of calorimetry is found in reference [29].

The use of the narrow band beam in this experiment allowed the calorimeter calibration to be checked in a completely independent manner, by requiring the sum of measured hadron and muon energies to equal the beam energy. The results of the calibration using this constraint alone agreed with the previous result to within 5%, with 5% errors.

3.5 TRIGGERING

Two basic triggers, a "hadron" and a "muon" trigger, were used in the experiment. The muon trigger was formed by a coincidence of the trigger counters T1,T2, T3 on either side of the magnet (see figure 3-1), plus 2 out of 4 of the calorimetry counters nearest the magnet. This was the primary trigger for CC events with forward muons, and triggered on any event which produced a muon traversing the magnet. There were also background triggers due to cosmic rays and beam-associated muons which penetrated the shielding. These muons, in

general, lost most of their energy in the shielding, and those which entered through the front of the apparatus usually ranged out in the calorimeter. The ones which did produce muon triggers were usually those which missed the calorimeter and only triggered T1-T2-T3 by passing through the edges of the counters (missing the magnet). The inclusion in the trigger of the 2 out of 4 calorimetry counters reduced this background considerably, but didn't affect the efficiency for good CC events.

Neutral current events, of course, never produced muon triggers. A special "hadron trigger" was devised for this experiment to trigger on the energy deposition in the calorimeter, with a minimal penetration requirement. The apparatus was divided into 11 modules of 6 counters each (the 4 counters closest to the magnet were not included). The trigger required the total pulse height of the module -- i.e., the mixed signal of the 6 counters -- to be above a threshold, and also required at least two of the counters in the module to show at least single-ionizing signal. The threshold was set to correspond to a hadron shower of about 8 Gev, or 40 times single-ionizing.

The trigger efficiency was measured by taking all events which produced a muon trigger, and counting as a function of hadron energy the fraction that also produced a hadron trigger (see figure 3-7). The threshold was not sharply defined for several reasons. (1) The mixed signal of the 6 counters was not strictly proportional to hadron energy, since differences in calibration between counters (on the order of 10-15%) could be taken into account only in the analysis, and not in the trigger itself. (2) Events which occurred near the downstream end of a module might divide their energy between two modules, and therefore not give a trigger in either module even though the total (summed) shower energy was above threshold.

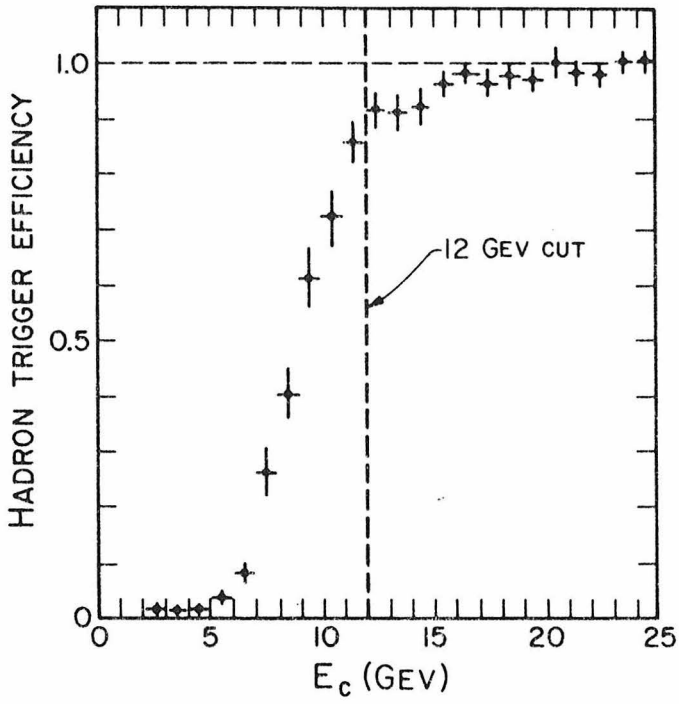

Figure 3-7: Hadron trigger efficiency as a function of measured hadron energy. Only data with $E_c > 12$ Gev, where the trigger is > 90% efficient, were used in the analysis.

The nominal 8-Gev threshold was determined by cosmic ray background levels. If the threshold had been set much lower, this background would have been intolerably high and would have caused a significant amount of dead-time in the experiment. This background will be discussed further in Chapter 5.

Since the trigger efficiency fell rather rapidly below 12 Gev, and since backgrounds became much worse and event identification more difficult, a cut was applied at 12 Gev in the final data analysis. Only events with $E_c \geq 12$ Gev were used.

3.6 SPARK CHAMBER SYSTEM

There were two sizes of spark chambers used in the calorimeter, nominally 5' by 5' and 5' by 10'. The two were almost identical in construction and operation, so only the larger size will be described here. The chambers were constructed from two reinforced aluminum panels, 65" by 125". Insulated ribbon cable, with wires spaced every 1 mm, was glued onto the surface of each sheet to form the two wire planes for x and y measurements in each chamber. The two sheets were glued to either side of a 3/8" thick plexiglas frame, leaving an interior volume of 3/8" x 60" x 120" for neon-helium gas. Gas was recirculated through the chambers and through a liquid-nitrogen purifying system.

One end of the ribbon cable on each sheet extended out beyond the plexiglas to a high-voltage or ground bus, and also to a magnetostrictive wire used for readout. Each chamber was pulsed by its own high-voltage pulser, which stored about 6 kv. When the chamber sparked, the x and y wires at the spark coordinates carried current. The pulse of magnetic field created by this current produced an acoustic pulse on the magnetostrictive wire at the point where the ribbon cable crossed the magnetostrictive wire. The position of the spark was measured by the time required for the acoustic pulse to travel to a transducer at the end of the magnetostrictive wire. Two reference fiducial pulses were generated at fixed points near the two ends of the magnetostrictive wire when the chamber was pulsed, and spark coordinates were measured relative to these fiducial marks.

The pulses produced by the sparks were converted to digitized coordinates through a scaler system. The first fiducial from each wire started 4 scalers counting with 20 Mhz frequency, and each succeeding pulse stopped one of the scalers. The system employed a center finding technique to precisely locate the peak of the pulse, and the resolution of the system was about .8 mm. There was a serious limitation, however, in that only 4 sparks could be recorded per

chamber. This was perfectly adequate for tracking muons, but produced a bias in measuring hadron shower position -- only the 4 sparks closest to the transducer were recorded. To minimize the effect of this, the wands were read out in opposite directions on adjacent chambers, alternating left and right, and up and down, throughout the calorimeter.

3.7 SPECTROMETER

The muon momentum in CC events was determined from the bend angle of the track passing through the magnet. The magnet was 8' long and 5' in diameter, with an 8" hole along the axis. Coils passed through the hole and around the perimeter to produce an azimuthal field. The bend of the track was therefore in the radial direction; the polarity of the magnet was set to focus μ^- during neutrino data taking and μ^+ during antineutrino.

The magnet was run near saturation, with the field dropping from 16 kilogauss near the center to 14 kilogauss near the edge. Field measurements have been made by a) measuring the current induced in a loop encircling radial segments of the magnet when the field is changed from positive to negative polarity, b) calculating the field from studies made with a sample of identical iron, and c) comparing the momentum measured for backward-going cosmic rays to the energy determined by their range in the calorimeter. Systematic errors are on the order of 5%.

The chambers on either side of the magnet were aligned using muons which missed the magnet. Since the magnet was round with a 30" radius, and the chambers were rectangular, muons passing through the corners of the chamber missed the magnet and were ideal for alignment measurements.

The bend angle of a muon passing through the magnet was approximately

$$\theta_B(\text{mrad}) = \frac{\cdot 3 \cdot B(\text{kg}) \cdot L(\text{cm})}{p_\mu(\text{Gev})} = \frac{1100}{p_\mu(\text{Gev})} \qquad (3\text{-}3)$$

The error, or smear, in angle due to multiple scattering through the magnet is given by

$$\theta_{ms}(\text{mrad}) = \frac{15}{p_\mu(\text{Gev})}\sqrt{\frac{L}{L_{rad}}} = \frac{176}{p_\mu(\text{Gev})} \qquad (3\text{-}4)$$

Since both θ_B and θ_{ms} are inversely proportional to the muon momentum, the error in momentum measurement due to multiple scattering was independent of p. Multiple scattering in the calorimeter immediately before the magnet also contributed a small error, and the total error was calculated to be $\pm$ 18%.

This resolution has been experimentally checked by comparing the azimuthal deflection angle of muons (due to multiple scattering alone) to the radial deflection angle (due to the field and to multiple scattering), and agrees with the results above (see figure 3-8). Other errors due to chamber resolution and uncertainties in alignment were negligible by comparison except at very high muon energies ($\geq$ 130 Gev).

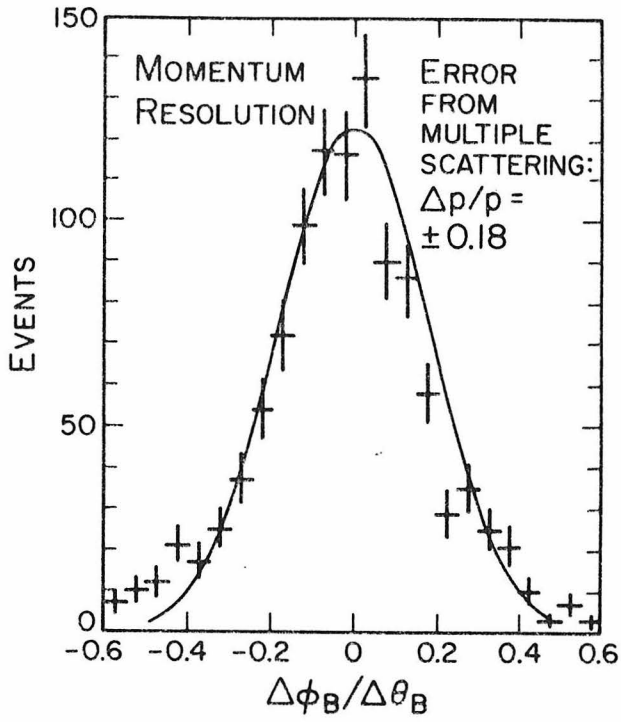

Figure 3-8: Resolution of muon energy measurement. The error due to multiple scattering is measured by comparing the azimuthal deflection (due to multiple scattering) to the radial deflection (due primarily to the field) as the muon passes through the magnet.

CHAPTER 4
EVENT ANALYSIS

4.1 EVENT RECONSTRUCTION

A typical CC event, reconstructed by an online analysis system, is shown in figure 4-1. The track of the muon through the spark chambers in the target-calorimeter and spectrometer is shown from both the side and top views. The energy deposition of the hadron shower, as measured by the pulse-height-analyzed signals of the calorimetry counters, is displayed in the upper part of the figure. The rows of dots immediately below this indicate a signal of at least one singly-ionizing particle measured by the counter at the corresponding location. The hadron energy of this event was measured to be 9 Gev and the muon energy 30 Gev, so this is evidently the interaction of a pion neutrino.

For comparison, a neutral current event is shown in figure 4-2. The sparks in the chambers define the interaction point to be very close to the center of the apparatus. Note that the range of the hadron shower is small, and both the scintillation counters and the chambers show that no charged particle penetrated very far through the steel. The measured hadron energy of the event was only 18.4 Gev. Since the typical incident neutrino energy is 50 Gev, this indicates that over half of the energy went into the final-state neutrino.

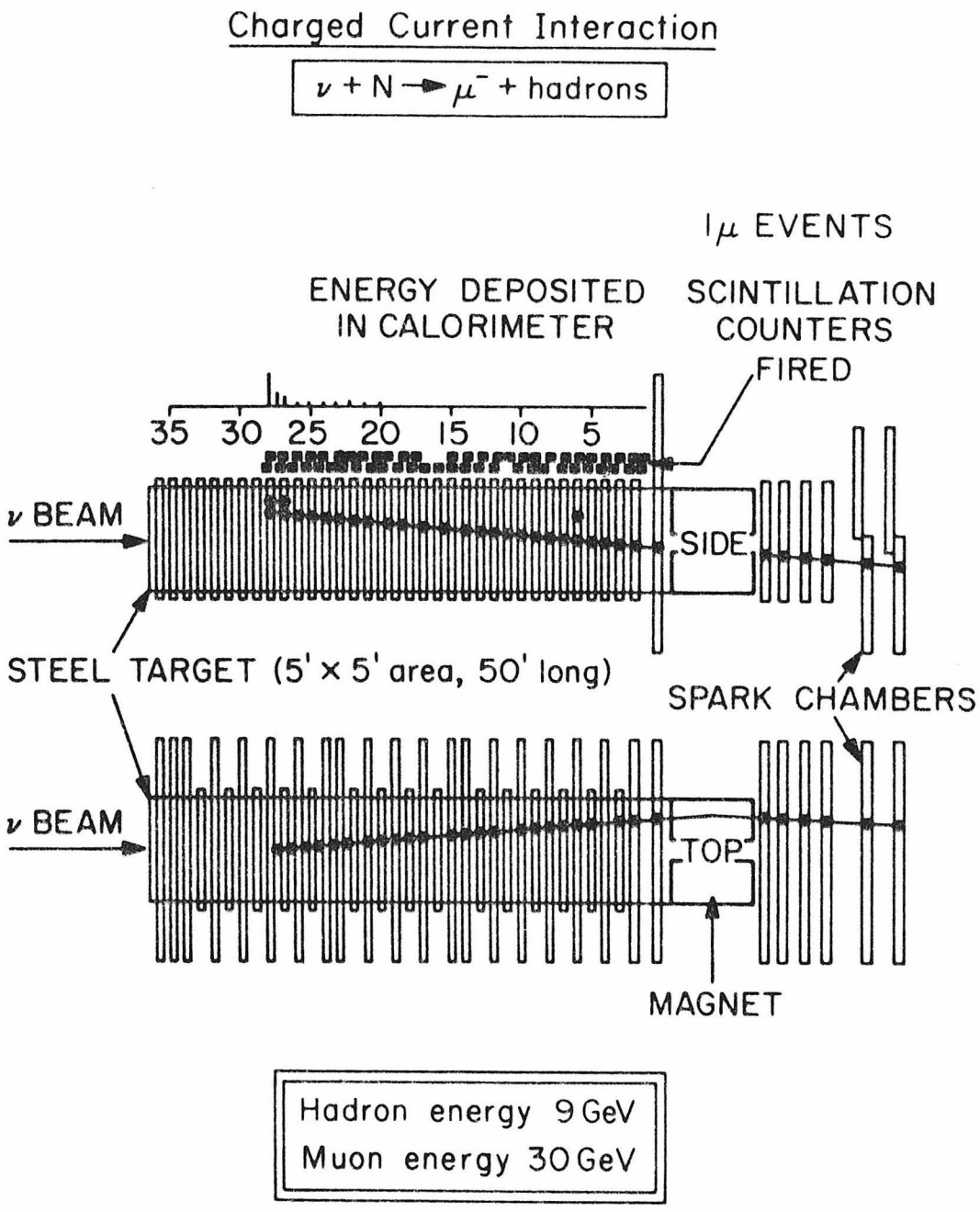

Figure 4-1: A typical Class 1 charged-current event, with focusing μ^- penetrating through the toroidal magnet.

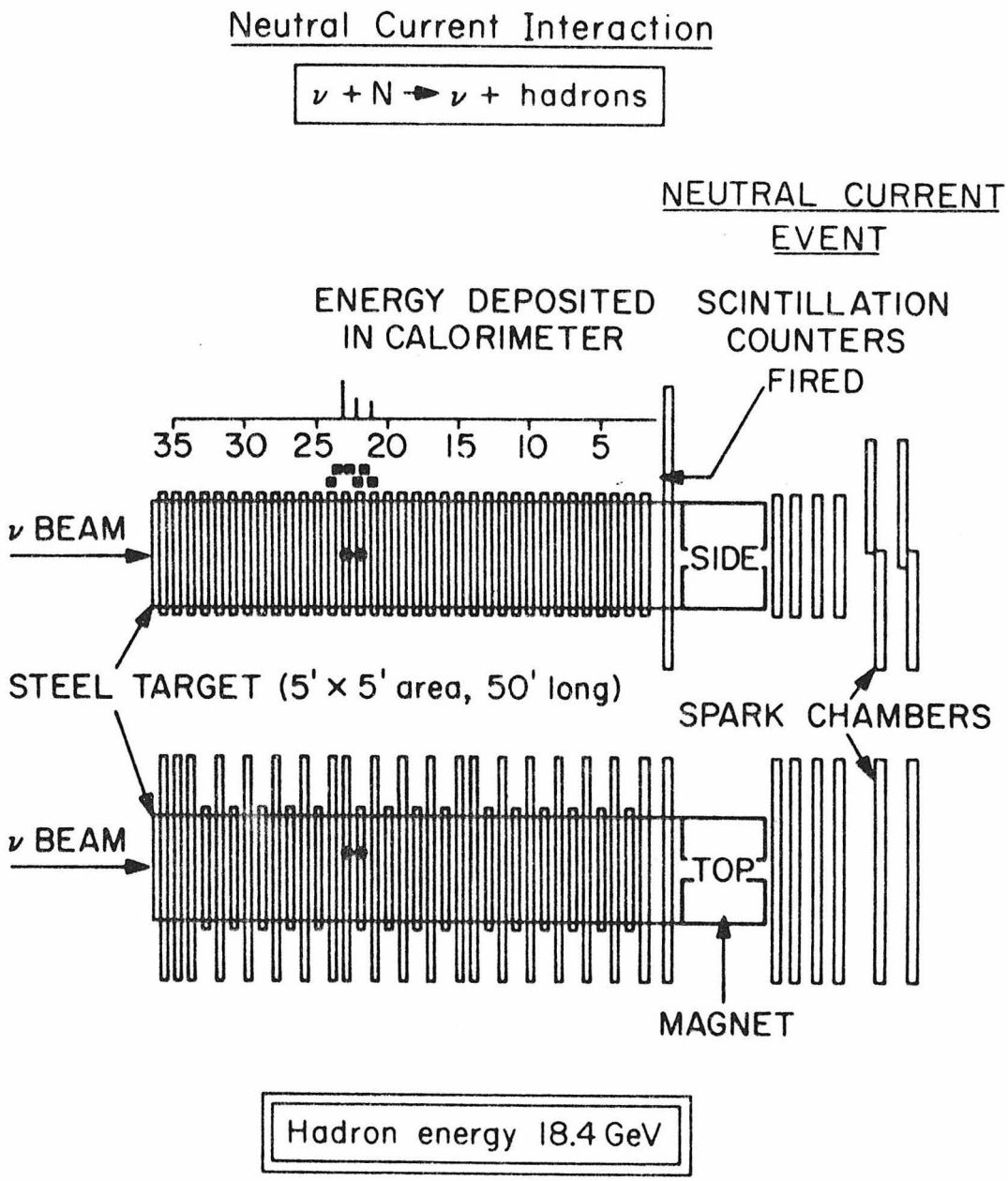

Figure 4-2: A good neutral current candidate. The spark chambers show that the interaction occurred near the center of the apparatus, so it is unlikely that there could have been an undetected final state muon. The small measured hadron energy indicates that a large fraction of the energy was unobserved, and presumably went into the final state neutrino.

4.2 MEASURED QUANTITIES AND RESOLUTIONS

For a CC event with muon passing through the magnet, the following quantities are measurable:

a) muon energy (E_μ)
b) muon production angle (θ_μ)
c) track vertex (T_x and T_y)
d) hadron shower vertex (V_x and V_y)
e) longitudinal position of interaction (z_I)
f) charged-particle penetration (P)
g) hadron shower energy (E_h)

The last four of these are also measured for NC events.

The muon energy in CC events was found by adding the muon momentum measured by the spectrometer to the ionization energy loss of the muon in the calorimeter (calculated from the total length traveled through steel). The ionization energy loss was 11.4 Gev for a muon passing through the entire calorimeter, so the muon momentum typically contributed the largest amount. The error in momentum measurement from multiple scattering was about 18% (see figure 3-8).

The error in muon production angle was also dominated by multiple scattering, and varied with muon momentum and track length. The typical error for a 30 Gev muon was ± 5 mrad, which is small compared to typical production angles of 100 mrad.

The longitudinal position of the interaction z_I was determined from the counters. A search for two successive counters having at least single-ionizing signal was made from the upstream end of the calorimeter, and the first of these defined the interaction point z_I. A similar search from the downstream end of the calorimeter determined the position at which the last charged particle left the calorimeter or stopped. The difference between these two positions was defined to be the penetration P of the event. A check was made for any break region between these two end positions, and if one was found the event was re-examined.

The transverse coordinates of the interaction were measured in two ways. The best measurement for CC events was obtained by extrapolating the muon track back to z_I; this defined the track vertex (T_x, T_y), and was measured for CC events only.

The second method of determining the vertex was to find the centroid of the sparks produced by the hadron shower. A search was made across the apparatus, in both x and y coordinates, for the region of maximum spark density in the 3 chambers following the interaction. A weighted mean of the sparks was found for each coordinate, with the sparks closest to z_I receiving the highest weight. This defined the "hadron vertex" (V_x, V_y). The precision of this vertex measurement was determined by comparing it to the (T_x, T_y) measurement for CC events with a clean muon track . The difference in vertex position measured by the two methods (see figure 4-3) was approximately ± 2.3", increasing from ± 2.0" at the lowest hadron shower energy to ± 2.6" at the highest. The vertex position was used only to make fiducial cuts

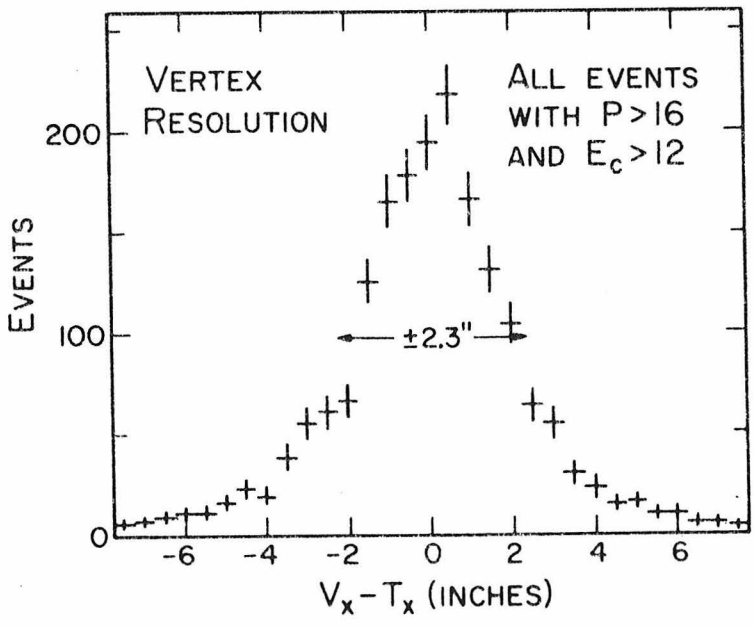

Figure 4-3: The resolution of the hadron shower vertex measurement is estimated by comparing it to the more accurate muon vertex. The difference between the two measurements indicates a resolution of ≤ 2.3".

on the data and to compare the NC and CC distributions as a function of position. The hadron vertex was used for these purposes for both NC and CC events so that all the data were treated the same way.

The most important measurement for neutral current events was that of hadron energy, since this was the only variable (other than position) measured. As discussed earlier, the hadron energy was determined by summing the signals of the 14 counters downstream of the vertex z_I. The observed signal was converted to a hadron shower energy by using the calibration obtained from the test calorimeter.

In CC events, the energy measured in the calorimeter also included a contribution from the final-state muon. The size of this contribution was determined by measuring the energy deposition of the muon in 14 counters well downstream of the shower, and was equivalent to 3.7 Gev of hadron shower energy. For NC events, the measured energy was all due to the hadron shower. Since CC and NC events cannot always be distinguished, for the purpose of discussing hadron energy measurements E_c will denote the energy observed in the calorimeter and E_h the actual hadron shower energy.

4.3 CUTS ON DATA

The hadron trigger was inefficient below 12 Gev (see figure 3-7), so all accepted hadron triggers were required to have $E_c > 12$ Gev. In addition to insuring good trigger efficiency, this cut also eliminated most of the triggers due to cosmic rays and background muons entering the apparatus from outside. In comparing NC and CC events, this cut was applied to all the data. In analyzing CC events alone (Chapter 6), events with good muon triggers but $E_c < 12$ Gev were also used.

Fiducial cuts were made 5" from the sides of the calorimeter, 144" from the downstream end, and 16" from the upstream end. Only events occurring within this volume were accepted. This eliminated any remaining background from charged particles entering the sides or

front of the detector, and also ensured full containment of the hadron shower. In the analysis of the CC data alone (Chapter 6), the track vertex (T_x, T_y) was used for this cut, but for all comparisons of CC and NC data the hadron vertex (V_x, V_y) was used for both NC and CC events, so that both sets of data were treated identically.

4.4 SEPARATION OF NC AND CC EVENTS

CC events were distinguished from NC events by the detection of a final state muon. However, for events with wide angle or low energy muons, it was difficult to distinguish the muon track from the hadrons in the chambers immediately downstream of the interaction. Even if a clear track was visible, it could not be unambiguously identified as a muon unless it penetrated through enough steel ($\geq$1.6 meters) to make the probability of its being a hadron negligibly small.

The most reliable and unbiased way to separate the events with muons from those without muons was by using the longitudinal penetration of the most penetrating charged particle produced in the interaction. Neutral current events should have penetrations typical of hadron showers (1.0 meter of steel). The penetration of CC events, on the other hand, is usually determined by the distance traveled by the muon before it leaves the calorimeter, and covers a wide range from short to long penetration; CC events with wide-angle muons have short penetration, and events with forward energetic muons have long penetration.

The counters, spaced every 10 cm (1 collision length) of steel, were used to measure penetration. The counters registering at least single-ionizing signal downstream of the interaction directly measured the penetration P in collision lengths. Figure 4-4 shows the penetration distribution of all events (NC and CC) for ν and $\bar{\nu}$. In both distributions the NC signal appears as a clear peak in the low-penetration region, well above the smooth distribution expected from CC events.

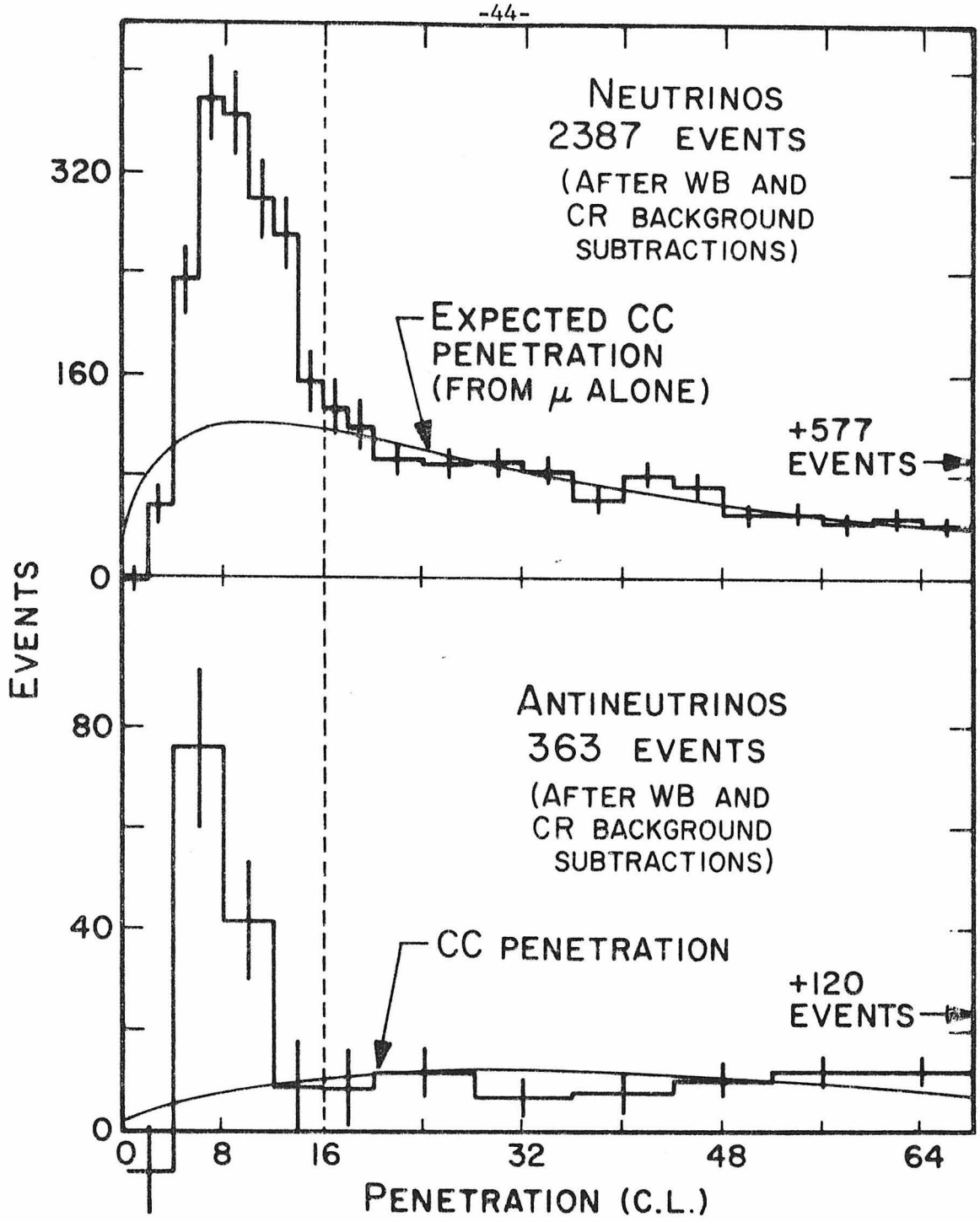

Figure 4-4: Penetration distributions of NC and CC events combined. NC events have short penetration (determined by the hadron cascade) and therefore appear as a peak in the low penetration region ($P \leq 16$). The smooth curves are the calculated CC distributions, normalized to all the data with $P > 16$ (including events with muons through the magnet, which are off scale in the plots above).

4.5 EVENT TOPOLOGIES

In order to better understand figure 4-4 and the assumptions that go into the calculation of the expected CC distribution, it is useful to divide the observed events into four topological classes (see figure 4-5).

Class 1 events are CC events with the muon passing through the magnet. Since the acceptance is highest for small angle muons, these events tend to occur at low x or y. All variables (p_μ, E_ν, as well as E_c, T_x, T_y, V_x, V_y) are measured.

Class 2 events have a clear muon track (penetration $\geq$ 16 counters), but the muon misses the magnet. P_μ and E_ν are therefore not measured.

Class 3 events have very wide angle muons, which not only miss the magnet but leave the calorimeter before traversing as much as 16 counters. The muons cannot clearly be identified, in most cases, so these events can be distinguished from NC events only on a statistical basis.

Class 4 events are NC events, which produce a hadron shower but no muon.

Before the total NC signal and the hadron energy distribution of NC events could be determined, the distribution of Class 3 events had to be estimated and subtracted from the distribution of all events with $P \leq 16$. This was done by extrapolating the Class 1 events (where x, y, and E_ν were all measured) and the Class 2 events (where only E_c and θ_μ were measured) into the Class 3 region.

These three different classes correspond to different values of θ_μ: Class 1 events tend to have small muon angles, Class 2 have moderate angles, and Class 3 have wide angles. An event occurring in the center of the calorimeter, for example, will be Class 1 if θ_μ is less than ~85 mrad, which is the angle subtended by the magnet, and

Class 1: Charged current event with muon through magnet. All quantities (vertex, E_h, θ_μ, E_μ) are measured.

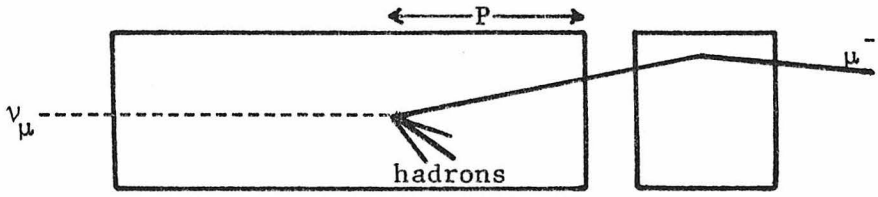

Class 2: Charged current event with muon penetrating through at least 16 counters (160 cm of steel), but missing magnet. Muon is clearly identified, but only muon angle θ_μ is measured and not muon energy.

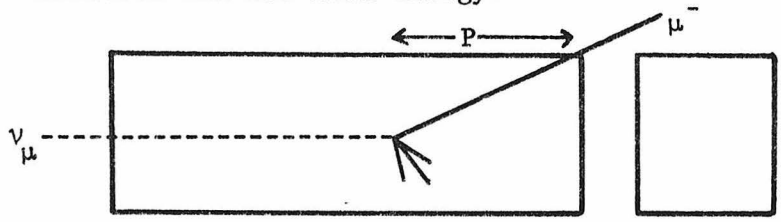

Class 3: Charged current event with muon either too low in energy or too wide in angle to be identified ($P \leq$ 16 counters).

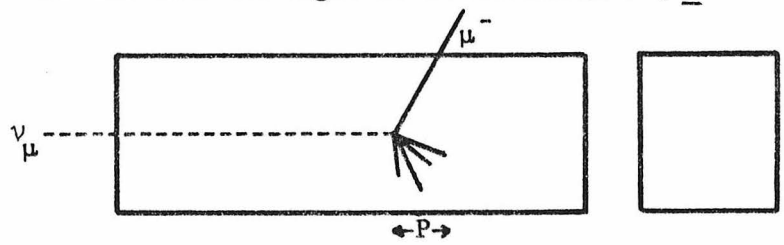

Class 4: Neutral current event. P is determined only by hadrons, so expect $P \leq 16$. Only penetration, vertex position, and hadron energy are measured.

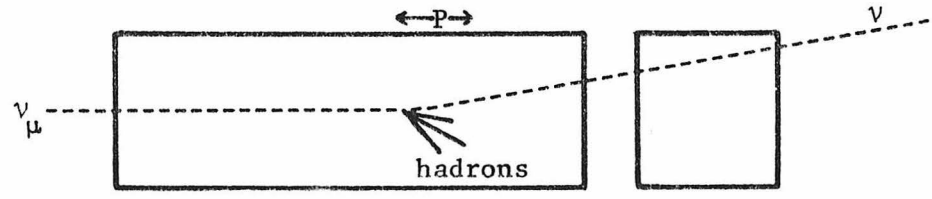

Figure 4-5: Topological classes of neutrino events.

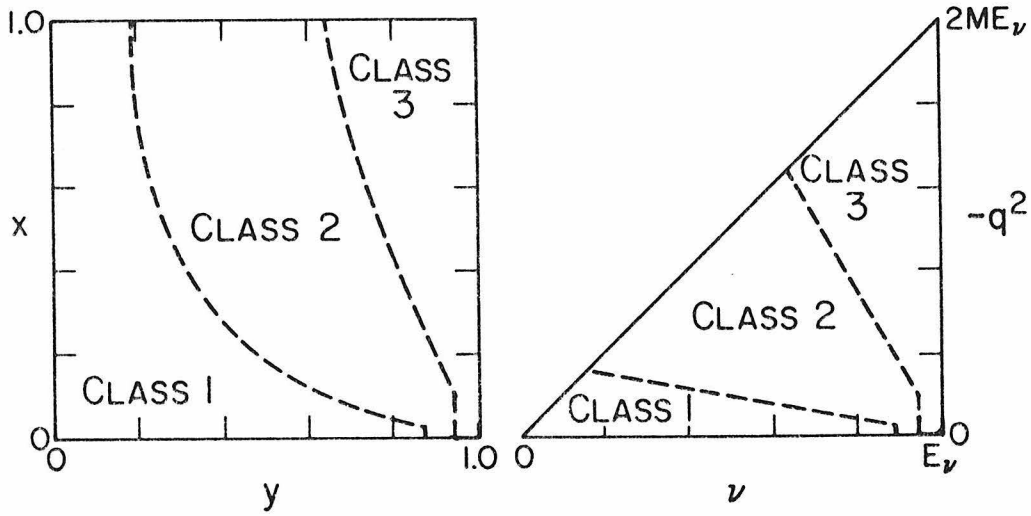

Figure 4-6: The approximate regions in x and y, and in q^2 and ν, populated by each of the three classes of CC events. Class 1 events have forward muons, and are characterized by small q^2 and small y. Class 2 events have moderately wide muon angles, and Class 3 are the events with very wide-angle or low-energy muons which are the CC background in the low penetration region.

will be Class 3 if θ_μ is wider than ~280 mrad. For a 60 Gev neutrino interaction occurring in the center of the apparatus, these angles define the boundaries shown in figures 4-6 below, which give a rough idea of the regions in x and y, and in q^2 and ν, that are populated by each of the 3 classes. Note that events with very low muon energy ($\leq$ 3 Gev) all lie in the Class 3 region, regardless of angle, since they ranged out before penetrating far enough to be distinguished from hadrons.

The true boundaries between classes were not so sharply defined, though, since the penetration of the muon depended on the transverse position of the interaction and the azimuthal muon angle, as well as on θ_μ. The apparatus had some acceptance for events up to production angles of 450 mrad (if the interaction occurred near the edge of the

apparatus and the muon pointed inward toward the center of the apparatus, rather than outward). The acceptance for such events was purely geometrical, and could be calculated as a function of interaction point and muon production angle.

4.6 OUTLINE OF DATA ANALYSIS

The analysis of the data is divided into three steps, which are discussed in the following 3 chapters. First, the data will be separated into the short-length ($P \leq 16$) and long-length ($P > 16$) regions, and possible backgrounds and corrections in each of these regions will be considered. The events with $P>16$ are almost all CC events (possible backgrounds from NC events with $P>16$ will be considered); the events in the $P\leq 16$ region include both CC and NC events.

Secondly, the events in the $P\geq 16$ region will be used to extrapolate the CC distributions in the $P\leq 16$ region. This extrapolation is necessarily somewhat model dependent, and different models of the charged-current interaction will be considered in Chapter 6.

Finally, the CC background will be subtracted from the $P\leq 16$ region to obtain the NC hadron energy distributions, which will be used to determine the coupling constants, V-A and V+A mixing, etc. of the neutral currents.

CHAPTER 5
CORRECTIONS, BACKGROUNDS, AND INEFFICIENCIES

5.1 RUNNING CONDITIONS

The data were taken during a 6-week period in August and September of 1974; 21.0×10^{16} protons were targetted with the beam tuned to focus positive hadrons (neutrino running), and 34.1×10^{16} with the beam set for negatives (antineutrino running). In addition, 6.4×10^{16} protons were used for closed-slit measurements focusing positives, and 14.9×10^{16} focusing negatives.

After the cuts in fiducial volume and hadron energy, there were a total of 2650 good triggers in the neutrino running and 574 in antineutrinos. In the neutrino data, 39% of these occurred for interactions in the $P \leq 16$ region, and in the antineutrino running the fraction was 42%. In neutrino running, about half of these short-length events were NC interactions and in the $\bar{\nu}$ data about 90% were NC. The determination of these fractions and the detailed separation of CC and NC events in this region will be discussed in Chapter 7.

Backgrounds from wide-band events and cosmic rays have been mentioned previously. The spectrum of each of these backgrounds was measured, and the normalized distributions were subtracted from the total data sample as shown in figures 5-1 and 5-2. Other corrections due to ν_e background, vertex-finding inefficiencies, and mistakes in penetration measurement are shown in figure 5-3. Each of these backgrounds and corrections will be discussed in detail in the

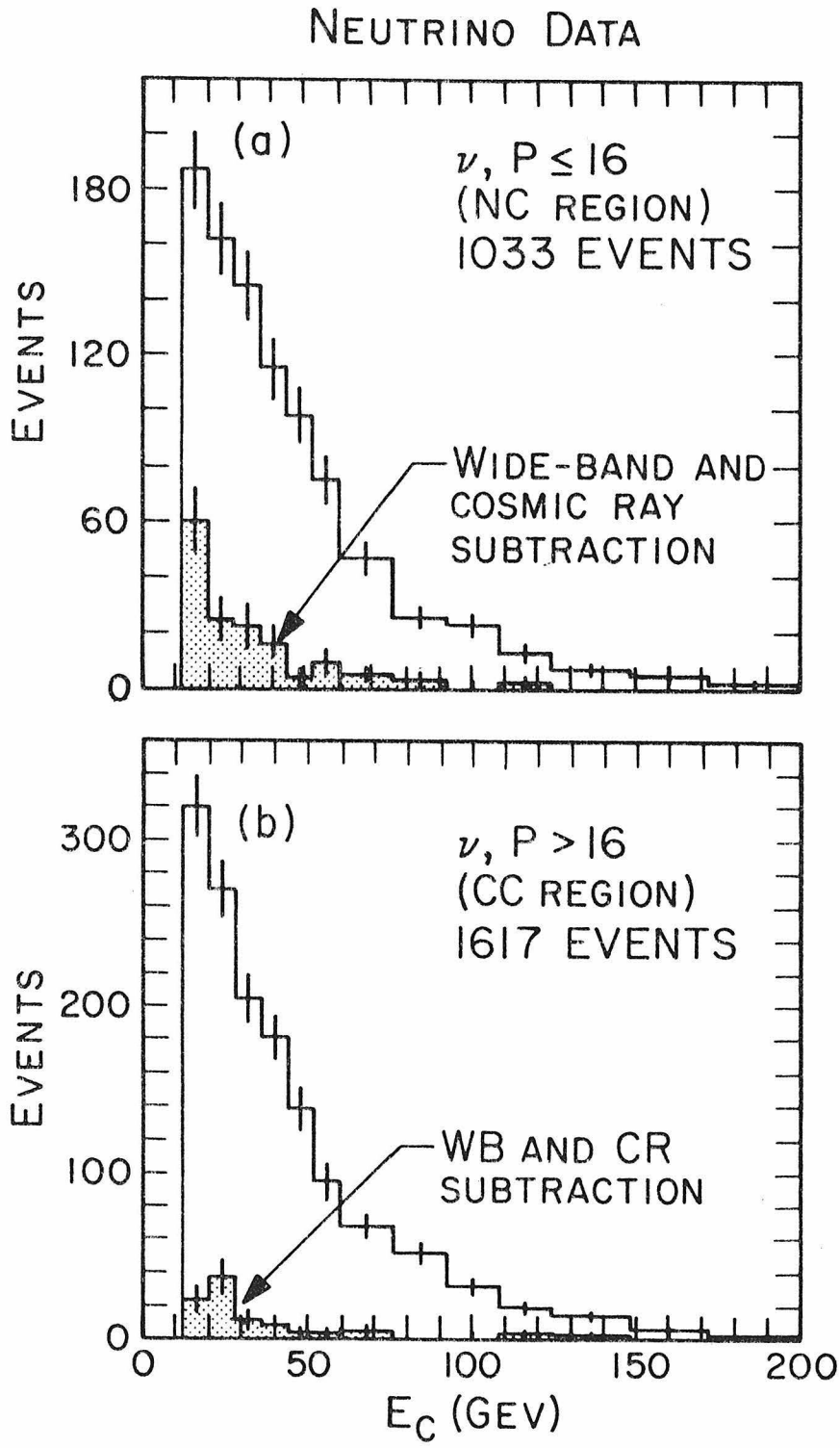

Figure 5-1: Raw neutrino data compared with the measured wide-band and cosmic ray backgrounds in both the long and short penetration regions.

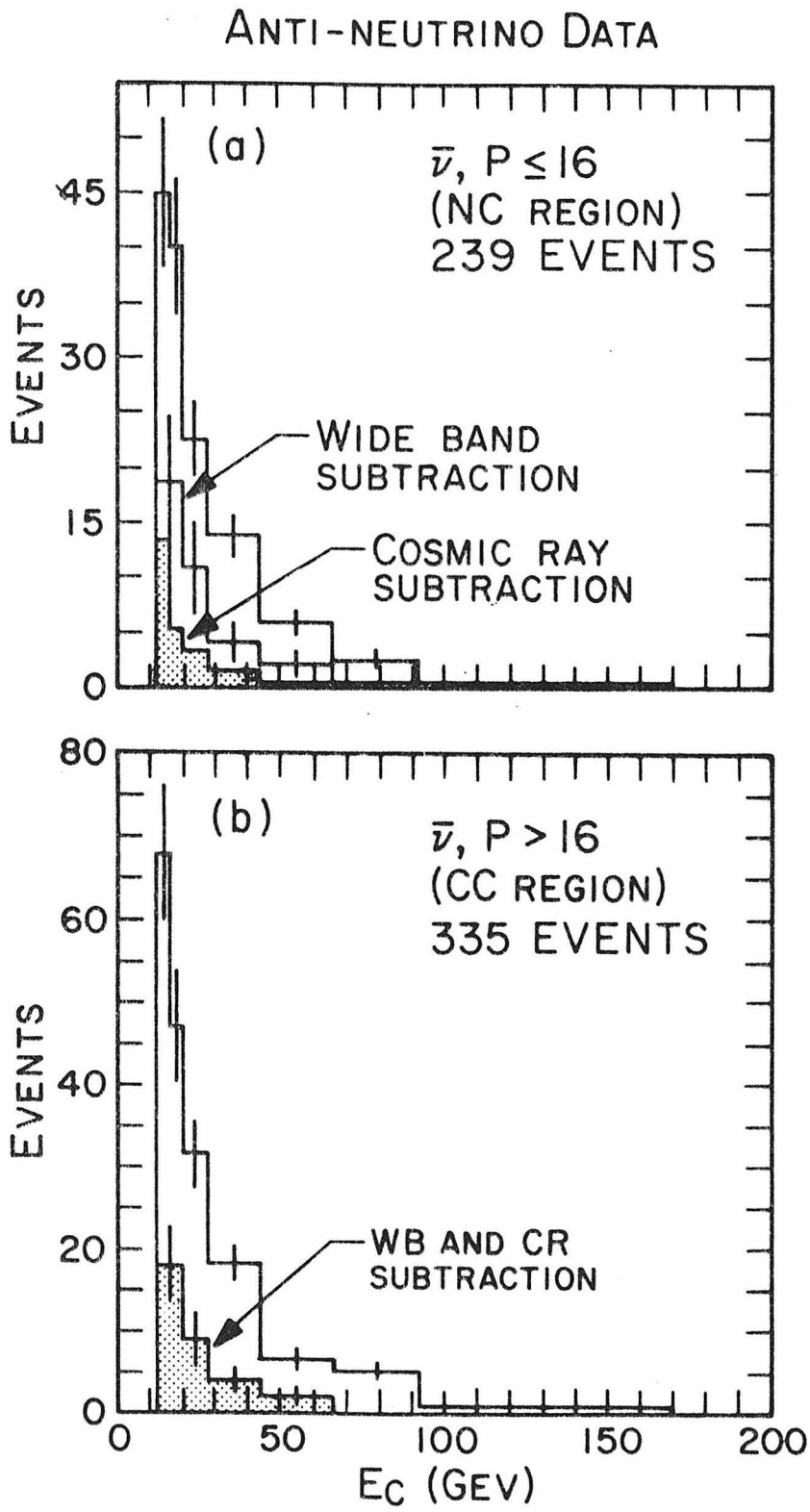

Figure 5-2: Raw antineutrino data compared with the measured wide-band and cosmic ray backgrounds in both the long and short penetration regions.

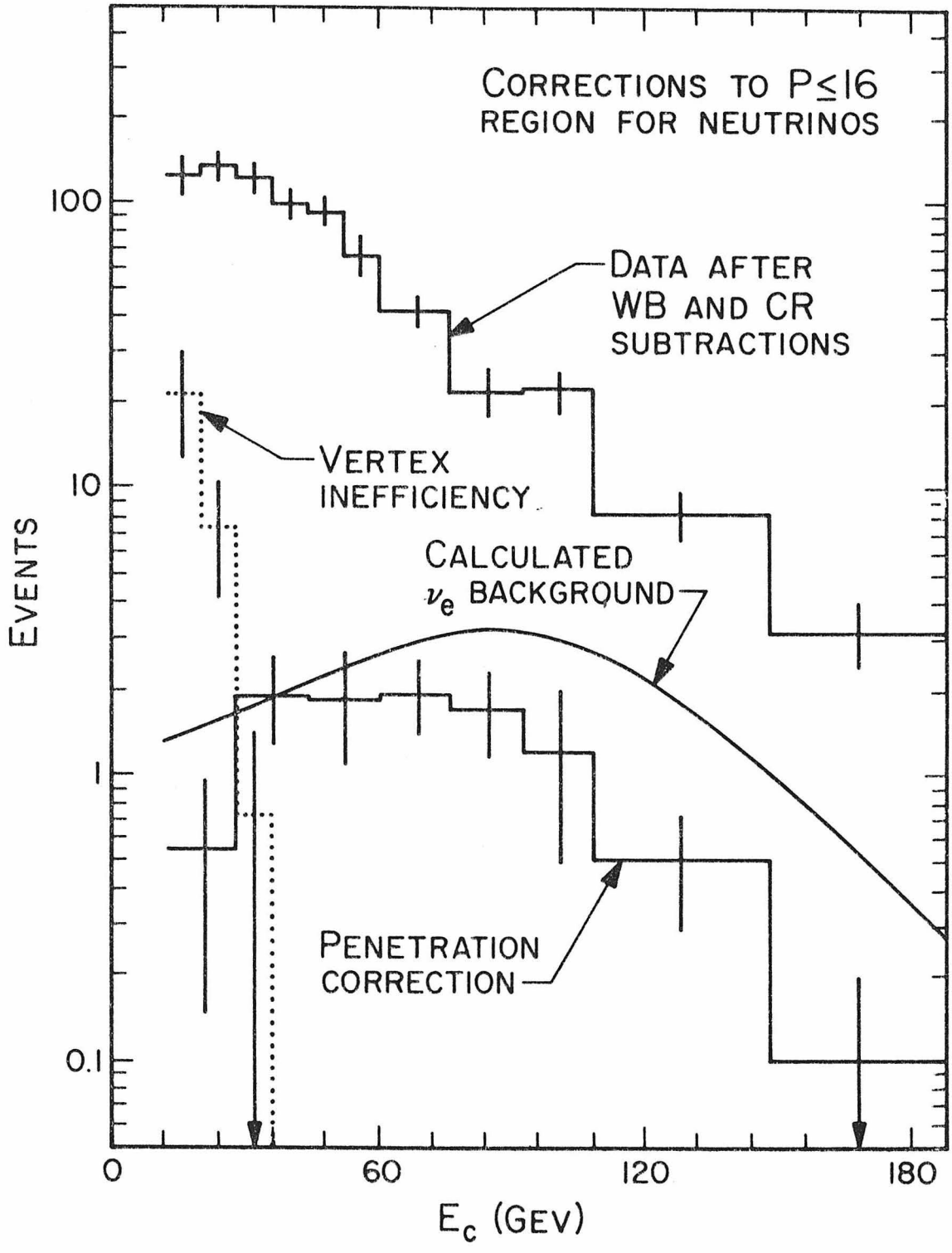

Figure 5-3: Corrections made to data in the low-penetration (P≤16) region. The "vertex inefficiency" and "penetration correction" curves are added to the data, while the ν_e background is subtracted.

remainder of this chapter.

5.2 WIDE-BAND BACKGROUND

As discussed in Chapter 2, there was a significant wide-band background neutrino flux which originated from decays occurring before the hadron beam was momentum selected. The decays occurred primarily in the region immediately after the target, where secondary fluxes were highest. In addition, there might have been contributions from upstream of the proton target, caused by the proton beam scraping collimators, magnets, or beam monitors, and there might have been a contribution from the proton beam dump. Since the production yields from a proton beam favor π^+ and K^+ over π^- and K^-, the wide-band flux from each of these sources presumably contained a significantly higher proportion of ν than $\bar{\nu}$.

The wide-band background was a potentially serious problem for a number of reasons. Since the wide-band flux was lower in energy than the narrow-band flux, the muons from wide-band CC interactions were lower in energy, wider in production angle, and more difficult to detect. The CC background in the $P \leq 16$ region was therefore relatively larger for wide-band events than for narrow-band events. Even more importantly, the wide band was not sign-selected, and therefore produced a significant "wrong-sign neutrino" background in the $\bar{\nu}$ running. Since the narrow-band fluxes were lower for $\bar{\nu}$ than for ν, and since the $\bar{\nu}$ cross-section was smaller than the ν cross-section, the wide-band background was relatively larger when the system was tuned for antineutrinos. It was of course impossible to distinguish between ν and $\bar{\nu}$ NC events from the final state particles, and was also impossible to distinguish between ν and $\bar{\nu}$ interactions for Class 2 and 3 events (where the muon sign was not measured). Since one of the great advantages of the narrow band beam was the ability to separate neutrino and antineutrino data, it was important to eliminate the wide-band background.

Fortunately, the design of the narrow band focusing system made it possible to directly measure the wide-band background originating from all of the sources mentioned above. This was done by running the experiment with the momentum slit closed. Since all the wide-band neutrinos originated from decays upstream of the momentum slit, the closed-slit running isolated the background flux from the narrow band beam. The beam and targetting conditions, triggering requirements, and data analysis were identical in the closed-slit and open-slit running. The final closed-slit data was multiplied by the ratio of incident proton fluxes (open slit/closed slit) and subtracted from the open-slit distributions.

The relative normalization between open-slit and closed-slit data was measured by a SEM upstream of the proton target, which monitored the incident proton flux. This measurement was checked by counting the number of Class 1 events with wrong-sign muons produced in open-slit versus closed-slit running. Since these events presumably came only from wide-band background, the rate should have been the same for open slit as for closed slit data. The measured rates agreed within the statistical error of 25%.

The total wide-band background accounted for 7% of the ν data and 30% of the $\bar{\nu}$ data. These rates were larger than expected by about a factor of two. This was a particularly serious problem for antineutrinos, where the subtraction introduced a significant statistical error of $\pm$8% into the data.

The measured wide-band rates were checked against the Hagedorn-Ranft flux predictions[23] for secondary hadrons (see figure 5-4). The calculated Hagedorn-Ranft flux normalizations were modified to agree with previous flux measurements in the narrow band beam[21]. The predicted closed-slit rates, normalized relative to the open-slit data, were about a factor of two lower than the measured rates. However, in addition to a 20% uncertainty in normalization, the Hagedorn-Ranft predictions were for a thin target and neglected

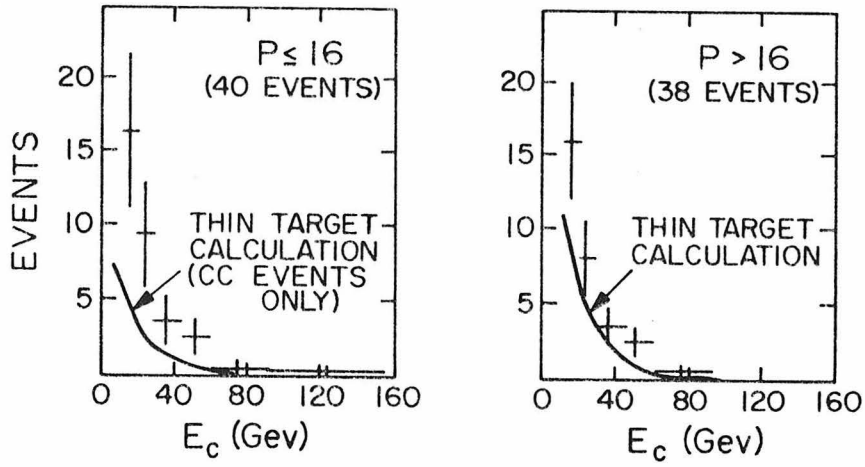

Figure 5-4: Measured wide-band backgrounds (focusing negatives). The thin-target calculation, normalized to the open-slit data, clearly underestimates the event rate.

secondary interactions within the target. Since the actual proton target was a foot-long bar of aluminum, secondary interactions of hadrons in the target were important, tending to produce more low-energy hadrons and thus to increase the wide-band flux at low energy. Hadrons produced by secondary interactions in the collimators immediately downstream of the target, as well as interactions of the proton beam upstream of the target, might also have been important contributors (see Chapter 2). It is therefore not surprising that the thin-target calculation underestimates the measured closed-slit rates.

We have considered trying to completely calculate the wide-band flux and include it as part of the beam. But due to the uncertainties discussed above, this has been abandoned. Even if the magnitude of the flux could be reliably calculated , the analysis of the wide-band events would be much more uncertain than that of the narrow band events. The CC subtraction is larger because of the lower energy, and considerably more uncertain due to uncertainties in the spectral shape of the flux. Also, the relative CC background in the $P \leq 16$ region differs by a factor of three between ν and $\bar{\nu}$ events, so the

uncertainty in relative ν and $\bar{\nu}$ fluxes would introduce an additional error. But the most important problem would be the separation of ν and $\bar{\nu}$ NC events. A clean separation of neutrino and antineutrino events was crucial to this experiment, and the ability to physically isolate the ν and $\bar{\nu}$ fluxes was one of the most important features of the narrow band beam. We therefore have not used the calculations of wide-band flux at all, but have used the directly measured closed-slit distributions to empirically subtract the wide-band background in both the $P \leq 16$ and $P > 16$ regions.

5.3 COSMIC RAY BACKGROUND

The second largest background was due to cosmic ray muons. In order to minimize trigger biases in the NC data, the hadron shower trigger (i.e., the energy deposition trigger) had to be made very unrestrictive, as described in section 3.5. There was consequently a considerable number of background triggers from cosmic ray muons, which entered the apparatus at steep angles and exited after going through only a few counters. Although cosmic rays entered the apparatus from outside the fiducial volume, most of them had such steep angles that they were inside the fiducial volume before passing through a spark chamber. These in general went through only one or two spark chambers in all; in most cases the track could not be reconstructed, and these cosmic ray triggers could not be clearly distinguished from neutral current interactions.

Most of the cosmic rays did not deposit enough energy to survive the 12 Gev cut in hadron energy, and most of the remaining ones did not produce a good vertex. But since the initial rates were very high (accounting for approximately half the total trigger rate), the final cosmic ray subtraction was still significant.

Cosmic ray backgrounds were monitored continually during the run. In addition to the ordinary beam gate of ~ 400 sec, a separate gate of 1 msec was opened between beam cycles to isolate and measure CR rates.

All cuts and event requirements were the same for both gates. The live-time was measured separately for beam gate and cosmic ray gate, and the ratio was used to normalize the CR data to the total beam data. Since statistics were virtually unlimited, the cosmic ray background could be measured extremely well and errors introduced by the subtraction were consequently small. The total background subtraction in the short-penetration region accounted for $7.2 \pm .3\%$ of the triggers in the neutrino run and $14.3 \pm .6\%$ for antineutrinos.

5.4 ELECTRON NEUTRINO BACKGROUND

An electron neutrino interacts through $\nu_e + N \rightarrow e^- +$ hadrons (CC event). Since the electron showers in the steel, no final state lepton is observed and ν_e events therefore look like NC events. All the energy is visible in a charged-current ν_e event, however, so the typical calorimeter energy distribution is higher for ν_e events than for the NC interactions of ν_μ's.

In addition to the CC interaction, μ-e universality requires that there be a neutral current interaction $\nu_e + N \rightarrow \nu_e + X$ which must also be included in the ν_e background subtraction. This contribution was estimated using preliminary values of the NC coupling constants, and accounted for about 20% of the total ν_e subtraction.

The ν_e flux comes principally from K_{e3} decays, and therefore was larger in the ν running than in the $\bar{\nu}$. The calculation of the ν_e fluxes was straightforward and depended only on the K_{e3} branching ratio and the kaon fluxes. Muon-electron universality was assumed, and the number of ν_e interactions was calculated as a fraction of the $\nu_{\mu(K)}$ interactions.

The calculated ν_e background, as a function of measured calorimeter energy, is shown in figure 5-3 for neutrinos. The distribution for antineutrinos is similar but smaller due to the smaller K^-/π^- flux ratio. The total subtraction amounted to about

9.2% of the final NC signal for neutrinos and 3.5% for antineutrinos.

5.5 NEUTRON BACKGROUND

In some neutral current experiments (such as the Gargamelle bubble chamber experiments) neutrons are a potentially serious problem[30], but they have a negligible effect in the Caltech experiment. At Gargamelle, neutrons originating from neutrino interactions in the magnet surrounding the chamber could penetrate well into the low-density chamber before interacting; since no final state lepton was produced, the events looked like NC events.

The Caltech detector is a high density material surrounded by low density, and consequently this background source is small. Moreover, in order for a neutron to trigger the apparatus it would have to have high energy (>12 Gev). It would have to be unaccompanied by charged particles, or else the veto counters would prevent a trigger. Finally, since the calorimeter is steel, neutrons would not penetrate very far, and the interaction would not survive the fiducial cuts on the sides and upstream end of the calorimeter.

5.6 VERTEX CORRECTIONS

In order to produce a good hadron vertex (V_x, V_y), an event had to produce charged particles which penetrated through at least two spark chambers. This created a bias between NC and CC events with very small hadron showers, since the CC events always had a high-energy muon which penetrated, while the NC events did not. If the hadron shower of a neutral current event was absorbed too quickly in the steel, no vertex was found and the event was rejected.

The size of this effect, as a function of hadron shower energy, was calculated with a Monte-Carlo program which generated hadron showers of a given energy and traced the cascades through a steel calorimeter. The detection efficiency for observing the shower in two

spark chambers was calculated as a function of hadron energy, with spark chamber inefficiency taken into account.

The total correction to the NC signal was found by multiplying this calculated inefficiency into the measured hadron energy distributions for neutral currents (after the short-length CC events had been subtracted). The correction for neutrinos was 30 ± 9 events (7% of the NC signal), and was 9 ± 6 events for antineutrinos (10% of the NC signal). The relative correction was slightly larger for antineutrinos because the NC hadron energy distribution was more peaked at low energy due to the differences in incident flux spectra.

This correction was checked by repeating the calculation as a function of penetration P, rather than E_h. For fixed P, the number of spark chambers penetrated depended only on whether the event occurred, for example, immediately before or immediately after a spark chamber. No Monte-Carlo was necessary for this calculation, since the vertex probability for fixed P was found simply by counting spark chambers within the penetration region. For example, a shower with P = 3 had to penetrate through either 1 or 2 chambers, with equal probability. The measured penetration distributions were multiplied by this vertex probability to give the total subtraction. Errors were larger this way due to limited statistics in the very small P region, but the agreement with the first method was almost exact.

5.7 MISTAKES IN PENETRATION MEASUREMENT

The calculation of the penetration distribution for CC events (figure 4-3) assumed that the penetration was the distance travelled by the muon through the calorimeter. This was not always true.

For example, if there was any back-scattering of hadrons from the vertex, the measured penetration was the total back-scattering distance plus the forward penetration of the muon or hadrons. This would tend to move events from the $P \leq 16$ region into the $P > 16$ region.

This effect has been pointed out by Yodh et al.[31], who have measured back scattering in very high-energy cosmic ray showers.

We have calculated the size of this effect by extrapolating Yodh's data down into the energy range of the hadron showers in this experiment. We estimate 38% of our hadron showers back-scatter through one counter, and 6% through two. This means that 38% of the events with measured penetration of 17, and 6% with penetration of 17 or 18, should in fact be in the $P \leq 16$ region. We have also searched the data for events which show anomalously low energy in the first one or two counters (as expected from back-scattering), and found evidence of back-scattering in 44% of the events. The total correction was 14 ± 4 events in the neutrino data and 1 ± 1 event in the antineutrino data. The effect is somewhat smaller for antineutrinos since the average hadron energy is less and the fraction of events with P=17 is also less.

A second source of error is due to very high-energy hadron showers which penetrate through more than 16 counters. If there is not also a muon penetrating this far, then these events in fact belong in the $P \leq 16$ region.

A search through the data was made for events with very penetrating hadron showers; all events were examined which had $P > 16$ and in which the shower had not fallen below 2.5 times single-ionizing after 10 counters. If the shower appeared to extend beyond 16 counters and there was no evidence of a muon, the event was assumed to belong in the $P \leq 16$ region. A total correction was made of 15.5 ± 8.0 events in the neutrino data, and 2.5 ± 1.0 in the antineutrino data. The large error comes from ambiguous events where it was not clear whether the most penetrating particle (beyond 16 counters) was a hadron or muon.

Other possible sources of error in penetration measurement (due to counter inefficiency, noise pickup in the amplifiers, uncertainties in counter position, etc.) were studied, and the total correction from

all of these was -8 ± 12 events for neutrinos and -1 ± 1 for antineutrinos.

Combining all of these sources together, the total correction due to mistakes in penetration measurement was 22 ± 15 events for neutrinos (5% of the NC signal), and 3 ± 2 for antineutrinos (3% of the NC signal). The corrections were made as a function of hadron energy, as shown in figure 5-3.

5.8 SUMMARY

The backgrounds discussed in this chapter are summarized in the table on the next page. In dealing with all of these, we have tried insofar as possible to rely on direct measurements rather than Monte-Carlo calculations. The electron neutrino subtraction is the only one which relied solely on a Monte-Carlo calculation, and the uncertainties in it were small.

The most serious background was the wide-band contribution to the $\bar{\nu}$ data. Not only did the subtraction introduce a significant statistical error in the $\bar{\nu}$ data, but the necessity of spending a large fraction of the running time in measuring this background further limited the time spent in data taking.

Possible ways of reducing this and other errors are discussed in Chapter 9.

Table 5-1. Ratios of background events to total recorded events in the $P \leq 16$ region.

	Neutrino	Antineutrino
Directly measured backgrounds:		
Wide band	.077 ± .018	.384 ± .074
Cosmic rays	.072 ± .003	.143 ± .006
Total	.149 ± .018	.527 ± .074
Estimated backgrounds and errors:		
ν_e events	.041 ± .004	.014 ± .003
Vertex inefficiency	-.029 ± .009	-.038 ± .025
Penetration error	-.021 ± .015	-.013 ± .008
Total	-.009 ± .018	-.037 ± .026

CHAPTER 6
CHARGED-CURRENT ANALYSIS

6.1 INTRODUCTION

Before the neutral currents data could be analyzed, the charged current contribution to the short penetration region had to be determined and subtracted. The CC data were also used to determine the incident neutrino fluxes, and thus to normalize the NC data. Both of these steps were somewhat dependent on the assumed form of the charged current interaction.

Early experiments[18,19,32], particularly at low ($\leq$ 40 Gev) energies, are consistent with a scaling model of the neutrino-nucleon interaction (described below). More recently, there have been some indications[33,34] that this picture may have to be modified at higher energies.

In this chapter we will compare several radically different kinds of models, both scaling and non-scaling, to the CC data to see which models are allowed and what restrictions the data imposes on these models. In order to draw definitive conclusions about possible scale-breaking in the charged-current interactions, however, one needs normalized flux measurements, good event acceptance, and good statistics for at least several different high energies. Because of the limitations in flux normalization and statistics, the CC data from this experiment do not clearly differentiate between scaling and non-scaling models.

Our primary emphasis in this chapter will be only to see which possibilities are consistent with the CC data. The possible effects of these different model assumptions on the neutral current analysis will be examined in the subsequent chapter.

6.2 MONTE CARLO PROGRAM

In order to compare these models to the CC data, we have constructed a Monte-Carlo program to simulate the neutrino interactions in the apparatus. The neutrino flux over the calorimeter was calculated as outlined in Chapter 2. Interactions were generated with probability proportional both to the predicted cross-section and to the flux, calculated as a function of transverse position across the calorimeter.

A comparison of the Monte-Carlo calculation to the observed transverse position distributions of Class 1 CC neutrino events (in which the muon momentum was measured) is shown in figure 6-1. Since the spatial distribution of events from π-decay neutrinos is expected to have a narrower width than that of the ν_K events (see chapter 2), the events are divided into low and high energy groups (ν_π and ν_K). The fits for the ν_π and ν_K events were separately normalized to the data in each plot. The effect of the steering angle during the neutrino running is evident.

The measured energy in the final state of Class 1 events was obtained by adding the measured hadron and muon energies. The calculated Monte-Carlo distributions, with all resolution and acceptance effects included, are compared to the data in figure 6-2. The two-peak structure of the narrow band beam is clearly evident. Note that the size of the high-energy band relative to the low-energy band is much larger for ν than for $\bar{\nu}$; this is due to the low K^- fluxes in antineutrino running, and to the suppression of ν_π events caused by the steering in the neutrino running.

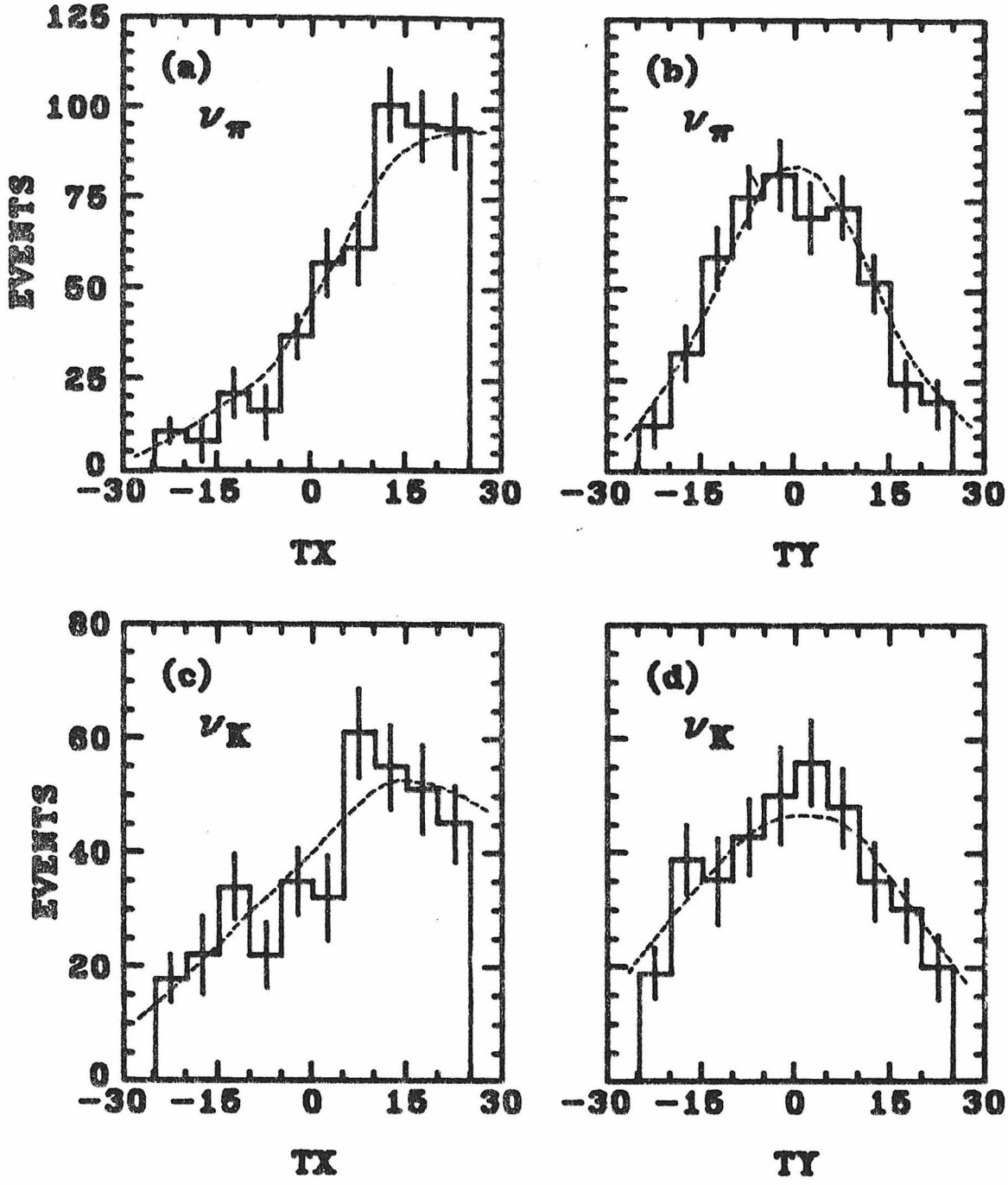

Figure 6-1: The spatial distributions of Class 1 neutrino events are compared to the Monte-Carlo calculation. The data are divided into low-energy (ν_π) and high-energy (ν_K) regions; note that the ν_π's form a narrower peak than the ν_K's. The beam is steered 1 mrad to the right, giving a higher proportion of ν_K's and better acceptance for very wide-angle muons.

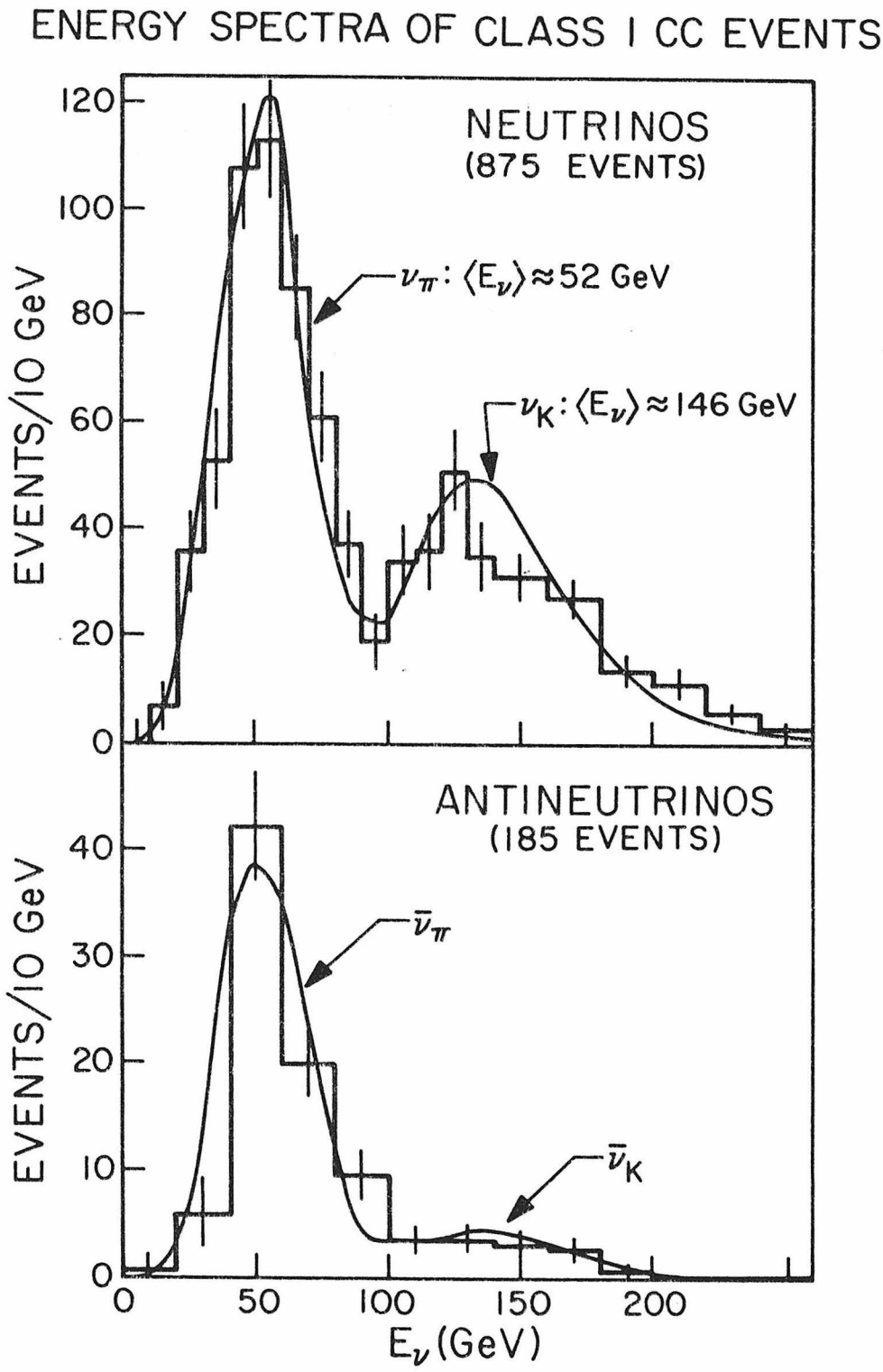

Figure 6-2: The ν_π and ν_K peaks of the narrow band beam are clearly evident in the ν and $\bar{\nu}$ spectra above. The neutrino energy is measured from $E_\nu = E_\mu + E_h$; the curve is the Monte-Carlo calculation.

The relative π and K fluxes were adjusted to give a best fit to the observed events in each of the models considered in this chapter. Because of this, the position and total energy distributions of Class 1 events are very insensitive to variations in the particular models chosen for the CC events. They therefore provide good constraints, or checks, on the shapes of the calculated flux spectra.

The scaling variables x and y for each Monte-Carlo event were generated according to an assumed differential cross-section. This is the point at which the model-dependent assumptions were introduced. The measurable variables such as E_c, p_μ, and θ_μ were calculated from x, y, and E_ν. The muon was traced through the calorimeter and magnet to determine acceptance, and trigger probabilities were generated by Monte-Carlo techniques. The variables corresponding to measurable quantities were "smeared" according to the measured resolutions of the apparatus. The Monte-Carlo therefore incorporated all the acceptance and resolution effects of the apparatus, so the final Monte-Carlo distributions of measured quantities can be compared directly to the data.

6.3 SCALING MODEL ASSUMPTIONS

We have used a scaling quark-parton model[15] as the simplest and most basic representation of CC interactions. This model assumes that the nucleon is composed of point-like spin-1/2 constituents which interact with the neutrino through a V-A coupling. Since the structures of neutron and proton are related by charge symmetry, the ν and $\bar{\nu}$ differential cross-sections for an isoscalar target are closely related, and are given by (see Appendix A):

$$\frac{d^2\sigma^\nu}{dxdy} = \frac{G^2 M E^\nu}{\pi} \left[Q(x) + \bar{Q}(x) (1-y)^2 \right] \qquad (6\text{-}1a)$$

$$\frac{d^2\sigma^{\bar{\nu}}}{dxdy} = \frac{G^2 M E^{\bar{\nu}}}{\pi} \left[Q(x) (1-y)^2 + \bar{Q}(x) \right] \qquad (6\text{-}1b)$$

$Q(x)$ and $\bar{Q}(x)$ represent the momentum distributions of quarks and antiquarks in the nucleon.

The point-like structure of the nucleon is also probed by the e-p and e-n scattering experiments at SLAC[15,35]. In parton models, the structure functions measured in e-d and ν-d experiments are related by

$$F_2^{e-d}(x) \propto F_2^{\nu-d}(x) = Q(x) + \bar{Q}(x) \qquad (6\text{-}2)$$

The e-d experiments have much better resolutions and statistics than neutrino experiments, and give a better measure of $F_2(x)$. We have therefore used the SLAC-MIT (Bodek) fit[36] for the shape of $F_2(x)$.

The e-d experiments cannot distinguish between quarks and antiquarks, however; these produce the same scattering in electromagnetic interactions, although they produce quite different effects in neutrino scattering. The $\bar{Q}$ distribution used in our analysis was parameterized as a product of $F_2(x)$ and an exponential (see figure 6-3):

$$\bar{Q}(x) = \frac{1}{2} F_2(x)\, e^{-\lambda x} \qquad (6\text{-}3a)$$

$$Q(x) = F_2(x) - \bar{Q}(x) \qquad (6\text{-}3b)$$

This parameterization has the important features that it concentrates antiquarks at low x and obeys the constraint $Q(0)=\bar{Q}(0)$. The total fraction of antiquarks in the nucleon is determined by λ.

The shapes of the x-distributions of both $Q(x)$ and $\bar{Q}(x)$ have no effect at all on the neutral current distributions. Since only the hadron energy is measured in NC events, the NC distributions are effectively integrals over x. Only the relative sizes of the

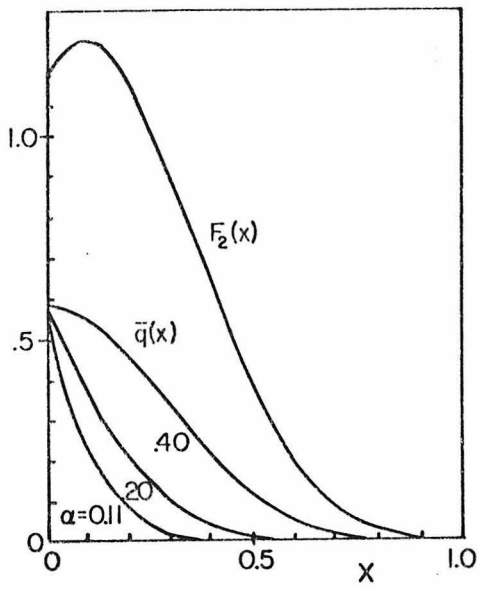

Figure 6-3:

Assumed parametrization of x-dependence

$F_2(x) = q(x)+\bar{q}(x) = \sum_{i=3}^{7} c_i(1-x)^i$

$c_3 = 3.276$
$c_4 = -7.168$
$c_5 = 31.22$
$c_6 = -44.56$
$c_7 = 18.384$

$\bar{q}(x) = \frac{1}{2}e^{-bx} F_2(x)$

$\bar{Q}$ component

$\alpha \equiv \frac{\int \bar{q}(x)dx}{\int F_2(x)dx}$ $\quad 0 \le \alpha \le 0.5$

integrals $\int Q(x)dx$ and $\int \bar{Q}(x)dx$ are important, and not their shapes.

This is also largely true of the CC distributions. The shapes of $Q(x)$ and $\bar{Q}(x)$ do affect the acceptance and angular distribution of the muon to some extent, but the y-dependence is more important. The muon angle can be expressed as a function of x and y as

$$\sin^2\left(\frac{\theta_\mu}{2}\right) = \frac{M}{2E_\nu}\,\frac{x\,y}{1-y} \qquad (6\text{-}4)$$

Because of the (1-y) term in the denominator, the distribution in y is the most important determinant of not only the measured hadron energy and y distributions, but also of the angle distribution of the muon. This means that both the hadron energy distributions and also the muon penetration distributions are more sensitive to variations in the y dependence than to variations in the x dependence.

The most important parameter in determining the CC distributions in a scaling model is thus the relative antiquark fraction $\bar{Q}/(Q+\bar{Q})$, which determines the relative amount of $(1-y)^2$ scattering. For this reason, we have used

$$\alpha \equiv \frac{\int \bar{Q}(x)\,dx}{\int [\,Q(x)+\bar{Q}(x)\,]\,dx} \qquad (6\text{-}5)$$

as a "shape parameter" to parameterize the CC distributions, and have varied α by varying λ in equation 6-3 (as indicated in figure 6-3).

Equation (6-3a) is not meant to be a "best fit" to the shape of the antiquark distribution, and the actual distribution may be different. For example, this parameterization violates the Gross-Llewellyn-Smith sum rule[37]. But the sum rule depends strongly on the form of $\bar{Q}(x)/x$ as $x \to 0$. Because of the extra factor of x in the denominator, the sum rule is extremely sensitive to $\bar{Q}(x)$ in the very low x region ($x \to 0$), while the measured distributions are not. We have tried other shapes for the $\bar{Q}(x)$ distribution, such as $\bar{Q}(x)=\alpha F_2(x)$, and the predicted distributions were not sensitive to the shape of $\bar{Q}$ for fixed α.

In a scaling model, α can be related to the total cross section ratio $\sigma_{\bar{\nu}}/\sigma_{\nu}$ by integrating equations 6-1:

$$\frac{\sigma^{\bar{\nu}}_{CC}}{\sigma^{\nu}_{CC}} = \frac{1+2\alpha}{3-2\alpha} \qquad (6\text{-}6)$$

Total cross-section measurements have been made by several experiments at energies below 60 Gev. The measured $\sigma_{\bar{\nu}}/\sigma_{\nu}$ ratios and the corresponding values of α calculated from equation 6-6 are listed in the table below.

Experiment	Energy range	$(\sigma_{\bar{\nu}}/\sigma_{\nu})_{CC}$	α
Caltech[19]	≈38 Gev	.40 ± .11	.07 ± .11
HPWF[38]	10 - 60 Gev	.41 ± .11	.08 ± .10
Gargamelle[18]	1 - 10 Gev	.38 ± .02	.05 ± .02

6.4 COMPARISON OF THE CC DATA TO THE SCALING MODEL

The parameter α, regarded as a shape parameter, can be fit to the data of this experiment in a variety of ways (e.g., from the angle distribution, hadron energy distribution, or y distribution). The most sensitive determination would come from the y distributions, but y could not be measured for Class 2 events (events in which the muon missed the magnet). The method used was to fit simultaneously the low- and high-energy y distributions of Class 1 events and the E_h distribution of Class 2 events. Flux normalizations were adjusted to give minimum chi-square for each value of α. This procedure included all the available y and E_h information, as well as the relative numbers of Class 1 and Class 2 events.

The antineutrino distributions were considerably more sensitive than the neutrino distributions to changes in α, and the value of α obtained by fitting the $\bar{\nu}$ data was thus less sensitive to systematic errors in acceptance, assumed x-distributions, etc. The best value obtained by fitting α to the low energy $\bar{\nu}_{\pi}$ data alone was $\alpha = .17$ (+.12,-.06), and we regard this as the best determination of the antiquark fraction $\bar{Q}/(Q+\bar{Q})$, in a scaling model, from this data. This is somewhat higher than the values indicated by the total cross-section experiments, but is not inconsistent with them.

The θ_{μ} distributions were not used in the fit, except to the extent that they influenced the relative number of Class 1 and Class 2 events. A comparison of the data to the angular distributions predicted by the assumed differential cross-sections therefore provides a good check on the validity of the fit. Figure 6-4 shows this comparison for all the events with P>16 (Class 2 as well as Class 1 events).

A detailed comparison of the Class 1 events to the scaling model with $\alpha = .17$ is made in figures 6-5 through 6-8. Figures 6-5(a,b) and 6-6(a,b) compare the x and y distributions for ν_{π} and ν_K events. In a scaling model, these should be independent of energy except for

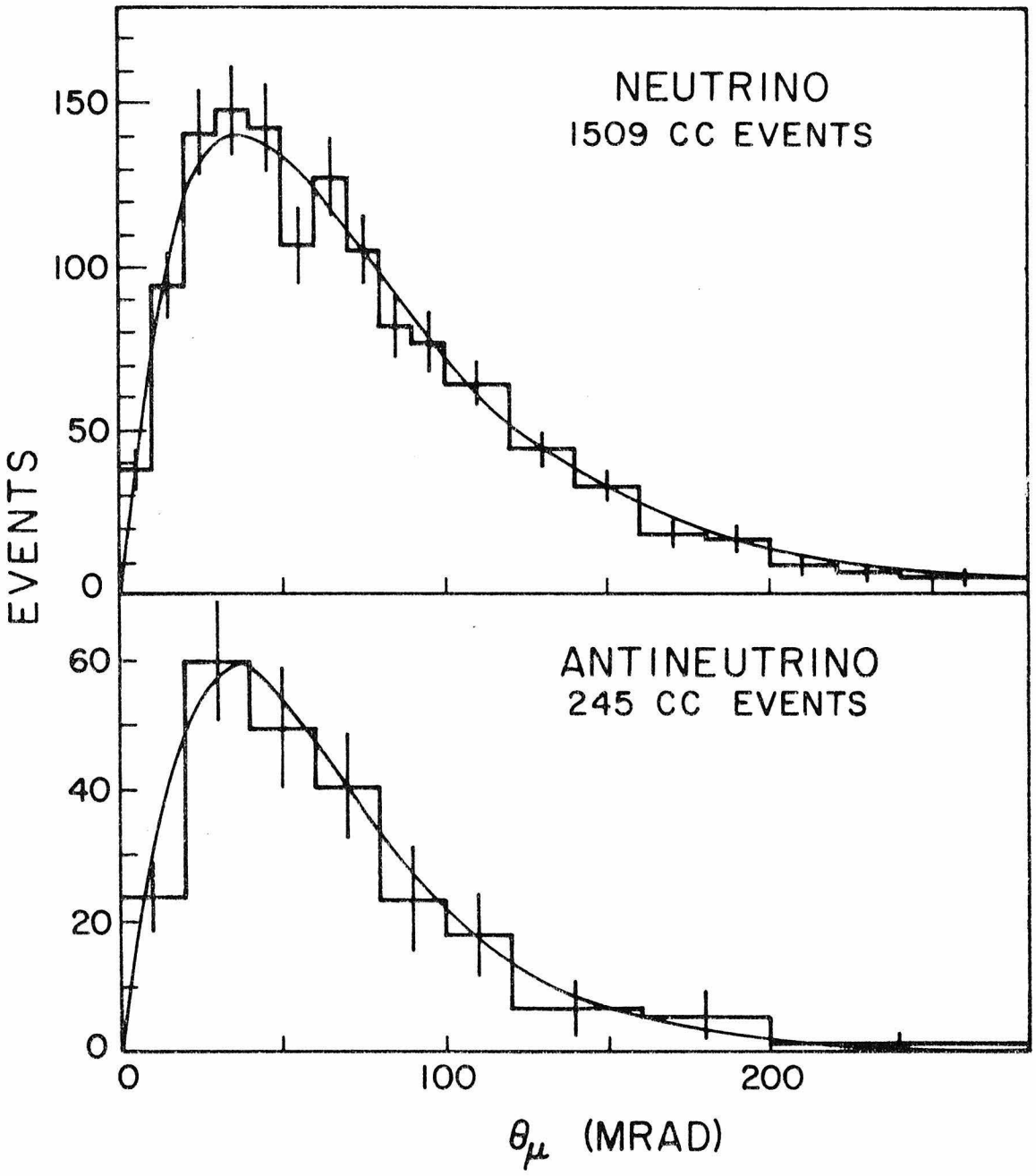

Figure 6-4: The muon production angle (θ_μ) distributions of both ν and $\bar{\nu}$ events are compared to the curves calculated from a scaling model of the CC interaction. The curves use α=.17, obtained by fitting the y and E_h (not θ_μ) distributions. All Class 1 and 2 events (i.e., all events in which θ_μ was measured) are included in the plots.

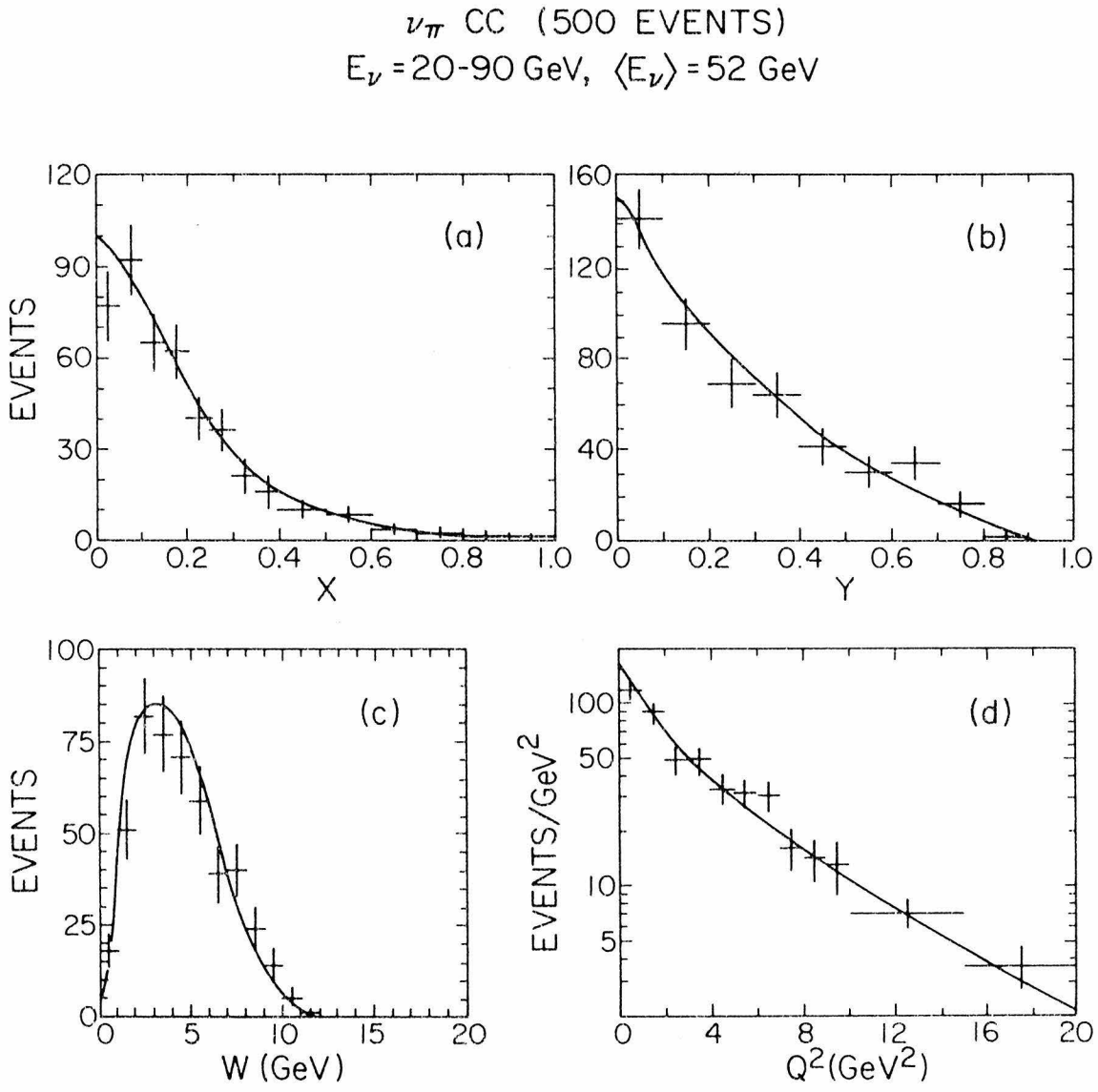

Figure 6-5: The measured distributions of Class 1 ν_π events are compared to the shapes calculated in a scaling model with $\alpha = .17$. In these and the following figures, the calculated curves include the effects of acceptance and resolution; the normalization of the curves is adjusted to give the best fit to the data.

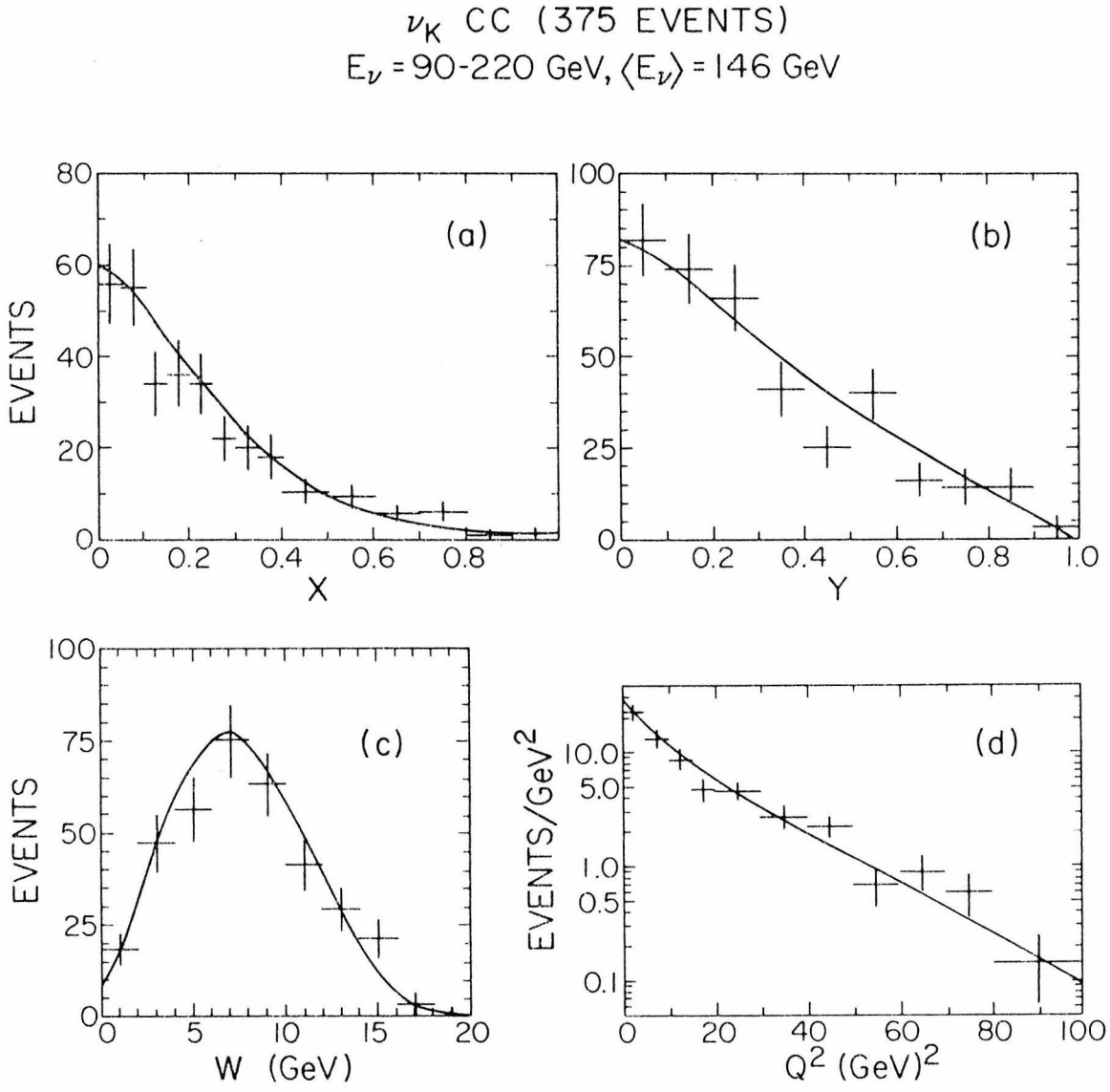

Figure 6-6: The measured distributions of Class 1 ν_K events are compared to the scaling model calculations. These distributions are the ones most sensitive to scale-breaking effects in the neutrino charged currents; they show no indications of any anomalous behavior.

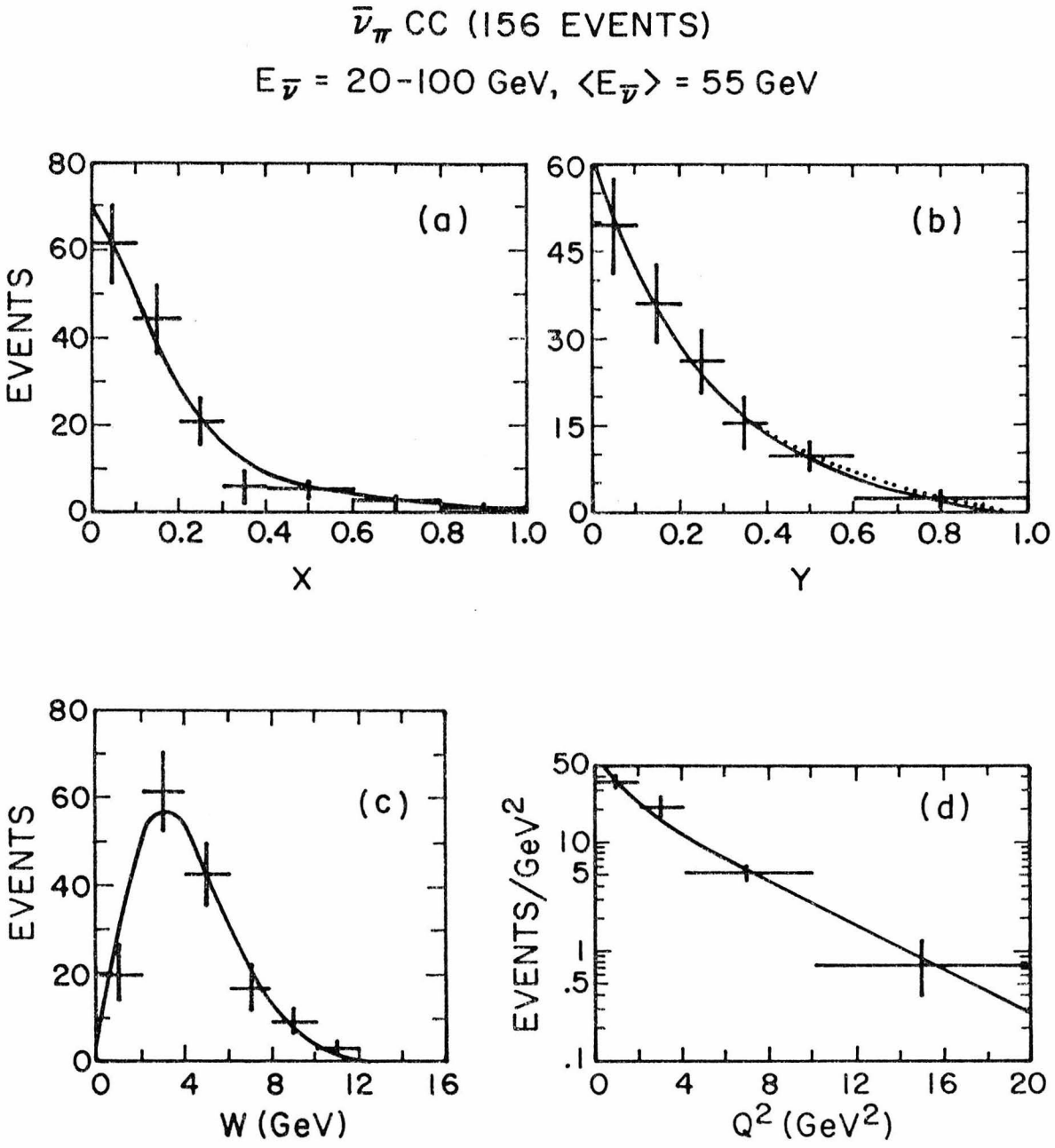

Figure 6-7: The Class 1 $\bar{\nu}_\pi$ data are compared to the scaling model with $\alpha = .17$.[π] The agreement is quite good; however, B-quark production would have a rather small effect on the shapes of these distributions. The deviation from scaling expected from the production of a 5 Gev B quark is indicated by the dotted curve in the y distribution.

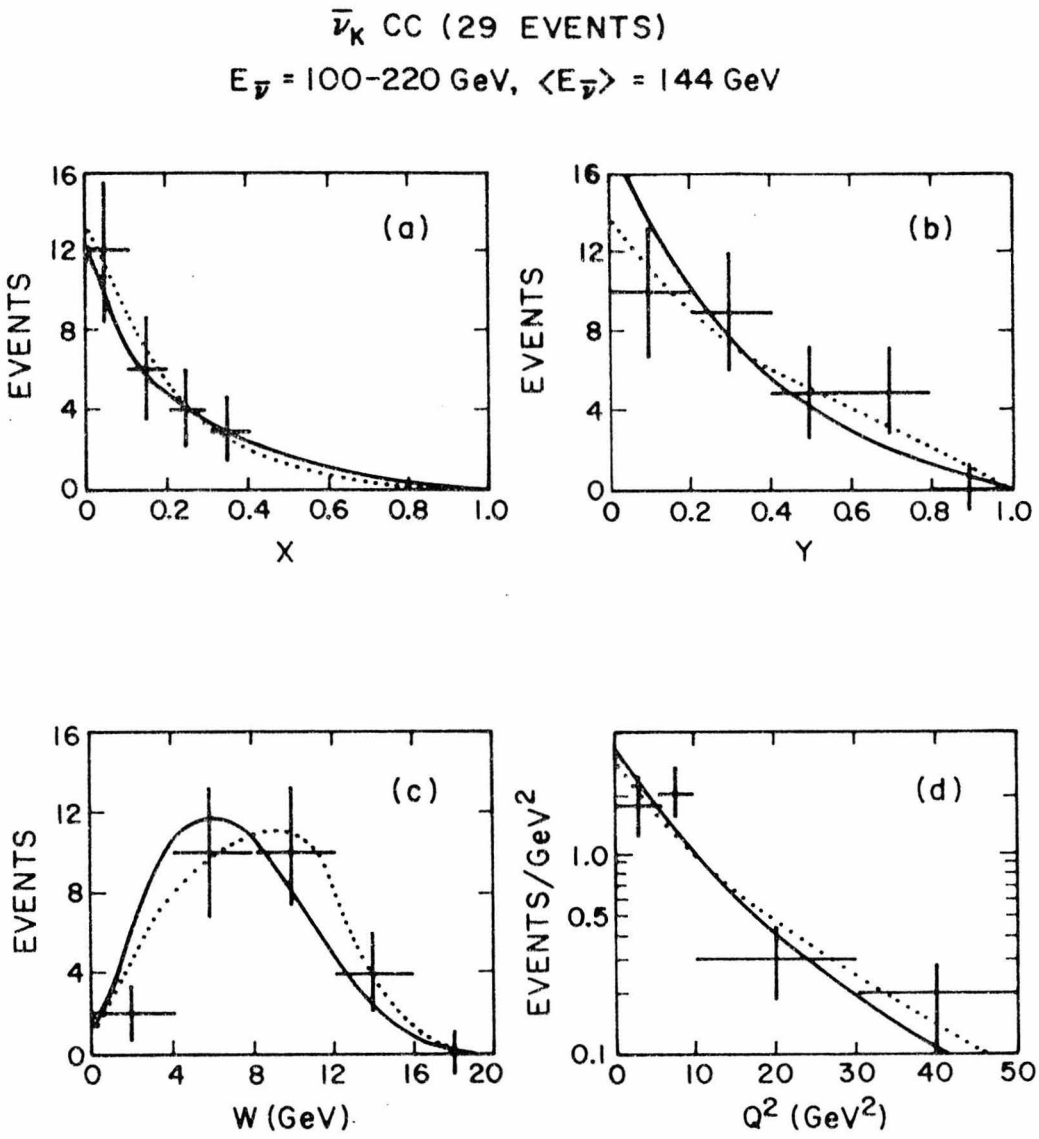

Figure 6-8: The Class 1 $\bar{\nu}_K$ data are compared to the distributions expected from both the scaling model with $\alpha = .17$ (solid curves) and the B-quark model with $M_B = 5$ Gev (dotted curves). In both cases, the flux normalization is adjusted to give the best fit to the data. The agreement with the B-quark model is somewhat better, but the statistics are too low for the comparison to be conclusive.

differences in acceptance. Figures 6-5(c,d) and 6-6(c,d) compare the W and Q^2 distributions, where $Q^2 = 4 E_\nu E_\mu \sin^2(\theta_\mu/2)$ is the square of the momentum transfer, and $W = (2ME_h - Q^2 + M^2)^{1/2}$ is the effective mass of the hadron system produced by the interaction. These distributions are sensitive to different kinds of scale breaking. For example, a low-mass W-boson propagator should decrease the number of events at large Q^2. This data rules out a W^+ mass of $\leq$ 10 Gev (similar and higher limits have been set by previous CC experiments[39]). New particle thresholds would be most apparent in the W distribution. There is no indication of either kind of variation from scaling in the neutrino events. It should be emphasized, though, that the relative K/π flux normalization is fitted to the data, so the only indication of a scaling violation would be a difference in shape, not normalization, between the data and the curves.

The agreement with a scaling model is not as good in the case of antineutrinos. In particular, the y-distribution for high-energy antineutrinos indicates a higher value of α due to the relative flatness of the measured distribution (see figure 6-8). This is only an indication, however, since it is based on only 29 events due to the low K^- fluxes. Also, since the $\bar{\nu}$ fluxes are dominated by the low-energy $\bar{\nu}_\pi$, there could be systematic effects due to the misidentification of a $\bar{\nu}_\pi$ event as a $\bar{\nu}_K$ event. For example, if a mistake is made in calorimetry giving an anomalously large value of E_h, a $\bar{\nu}_\pi$ event with low y could look like a $\bar{\nu}_K$ event with large y. The $\bar{\nu}_K$ events have been studied carefully, however, and there is no evidence, from either the events themselves or from the calorimetry studies, of any systematic effects of this kind.

6.5 MODEL WITH NON-SCALING α

In order to explore possible non-scaling effects, we have also tried fitting the data by letting α vary independently for low energy and high energy events, but otherwise using the form of equation 6-1. The best values obtained were α=.17 for ν_π and $\bar{\nu}_\pi$, and α=.30 for ν_K and $\bar{\nu}_K$. The ranges in α ($\pm$1 standard deviation limits) obtained by independently fitting each of the energy bands of ν and $\bar{\nu}$ are tabulated below.

	Allowed Ranges in α (from CC data)	
	Low energy (~55 Gev)	High energy (~145 Gev)
Neutrino	.0 - .20	.18 - .34
Antineutrino	.10 - .28	.32 - .50

This non-scaling model fits both the ν and $\bar{\nu}$ data better than the scaling model, but the difference was small for neutrinos and not statistically significant. The strongest indication of a possible scaling violation comes from the high-energy antineutrino data.

6.6 B-QUARK MODEL

A high-y anomaly[33] for high-energy antineutrino events has been reported by the Harvard-Penn-Wisconsin-Fermilab neutrino experiment. In particular, they see an excess of events in the high-y region relative to the low-y region, well above what one would expect from a scaling model. This is qualitatively similar to the effect that we see. It is difficult for us to make a direct comparison to their data, however, since they used a wide-band beam and the spectrum, running conditions, and acceptances were quite different.

A fit to the HPWF data, using a non-scaling model of hadrons with right-handed heavy quarks, has been made by Barnett [40]. We have compared a similar model to our data, and obtain results consistent

with Barnett's fit to the HPWF data.

The model assumes that a new doublet of right-handed quarks exists, called the "top" (T) and "bottom" (B) quarks (in Barnett's notation, these are u' and d'). Although these quarks are not found in the nucleon, they can be produced through the charged-current ν-quark interactions:

$$\begin{aligned} \nu + d &\rightarrow \mu^- + T \\ \bar{\nu} + u &\rightarrow \mu^+ + B \end{aligned} \qquad (6\text{-}7)$$

where u, d are the familiar "up" and "down" quarks. The couplings between (d,T) and (u,B) are right-handed (V+A), so the d→T and u→B interactions contribute a positive-helicity component to the total ν-N and $\bar{\nu}$-N cross-sections. The strength of the coupling is the same as the (u,d) coupling.

This model produces a rather radical violation of scaling. At very high energies, well above the threshold for producing the new quarks, the ν and $\bar{\nu}$ cross-sections approach equality. Nearer threshold, the new quark production would occur predominantly at large y. The effect of the T-quark would consequently be small, since the positive-helicity distribution is $(1-y)^2$ for neutrinos. But the effect of the B-quark on the $\bar{\nu}$ distributions could be very large.

Applying this B-quark model to the Caltech data and assuming α=.06 (in agreement with the low-energy Gargamelle data) gives a good fit to the $\bar{\nu}$ data. In particular, the B-quark contributes events at large y and large E_h, and this is the same effect seen in the data. The distributions obtained with a 5 Gev mass are shown, in addition to the scaling curves, for the $\bar{\nu}_K$ data in figure 6-8 (the effect on the $\bar{\nu}_\pi$ distributions is small, as shown in figure 6-7(b)). The y distributions are consistent with a B-quark in the range of 4-6 Gev.

6.7 SUMMARY

Both the model with the right-handed B-quark and the model with left-handed currents but energy-dependent α (increasing with energy) fit the antineutrino data better than a pure scaling model. However, until we have good flux normalization, better statistics, and a surer understanding of the CC behavior at high energies, we cannot rule out any of these models.

This uncertainty in the charged-current cross-sections creates an additional uncertainty in the neutral current data. The effects of each of these different models on the NC data will be explored in the next chapter.

CHAPTER 7
NEUTRAL CURRENT ANALYSIS: V AND A COUPLINGS

7.1 THEORETICAL CONSIDERATIONS

In this chapter the neutral current interactions are assumed to have the differential form

$$\frac{d\sigma^{\nu}}{dy} = \bar{E} \left[g_n + g_p (1 - y)^2 \right] \qquad (7\text{-}1a)$$

$$\frac{d\sigma^{\bar{\nu}}}{dy} = \bar{E} \left[g_n (1 - y)^2 + g_p \right] \qquad (7\text{-}1b)$$

where $\bar{E} = \frac{G^2 M E}{\pi} \int_0^1 F_2(x)\, dx$; g_n and g_p are the coupling constants for negative- and positive-helicity scattering. This is the scaling distribution expected if only V and A couplings exist and if neutral currents couple only to spin-1/2 partons. The scaling variable x, which is not measured in NC interactions, has been integrated out of the equations.

These equations are identical in form to the analogous equations for CC cross-sections (equation 6-1) integrated over x. However, equations 7-1 do not require the assumption of neutron-proton charge symmetry, nor are they valid only for an isoscalar target. They are true for any target if the neutral current is hermitian[9,42]. Even if the charged currents violate charge-symmetry by the production of new quarks in models such as Barnett's, the neutral currents would still scale and equations 7-1 would still hold true.

Other forms of the neutral current distribution are possible in more general coupling schemes, and some of these will be considered in Chapter 8.

7.2 PARTIAL NC/CC RATIOS

Before the neutral current events could be studied, the NC events had to be separated from the CC events in the $P \leq 16$ region (these were the Class 3 CC events, with wide-angle undetected muons). The distributions of these "fake neutral current events" were calculated using the Monte-Carlo program described previously. CC events were generated from the flux shapes and spectra shown in Figures 6-1 and 6-2 and using the physics assumptions discussed in section 6-3. The ratio of "fake NC events" ($P \leq 16$) to observable CC events ($P > 16$) was calculated as a function of hadron energy with the Monte-Carlo; this ratio was then multiplied by the number of actually observed CC events with $P > 16$ at each hadron energy E_c to obtain the distribution of charged-current "fakes". The resulting distribution of "fakes" was subtracted from the events with $P \leq 16$ to obtain the NC distribution, and was added to the $P > 16$ events to obtain the corrected distribution of all CC events. This procedure is illustrated in figure 7-1, using the scaling model of the charged currents with $\alpha = .17$ to calculate the subtraction of short-length CC events. The fractions $\epsilon_{\nu,\bar{\nu}}$ of CC events which lay in the $P \leq 16$ region were calculated to be

$$\epsilon_{\nu} = .224 \pm .008 \qquad (7\text{-}2a)$$

$$\epsilon_{\bar{\nu}} = .104 \pm .011 \qquad (7\text{-}2b)$$

The ratio of NC to CC neutrino events obtained in this manner is plotted as a function of interaction point in the calorimeter in figure 7-2. If the neutral current cross-section scales with energy, these ratios should be approximately uniform, as indicated in the figures. Since the subtraction of CC events with $P \leq 16$ is greater near

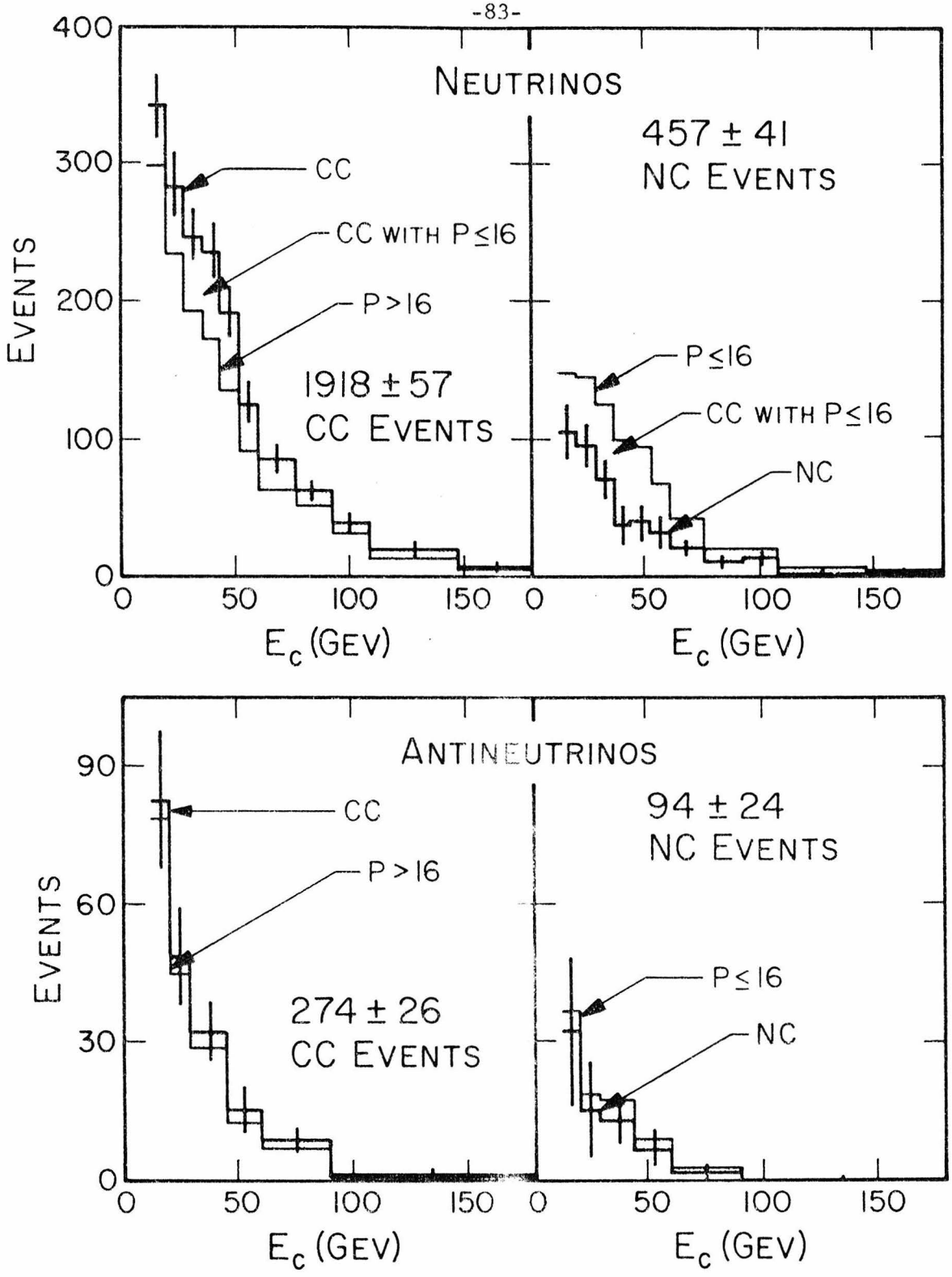

Figure 7-1: The corrected CC and NC distributions are compared to the uncorrected distributions of $P > 16$ and $P \leq 16$ events. The shaded areas represent the Class 3 CC events (with low penetration) calculated from the scaling model.

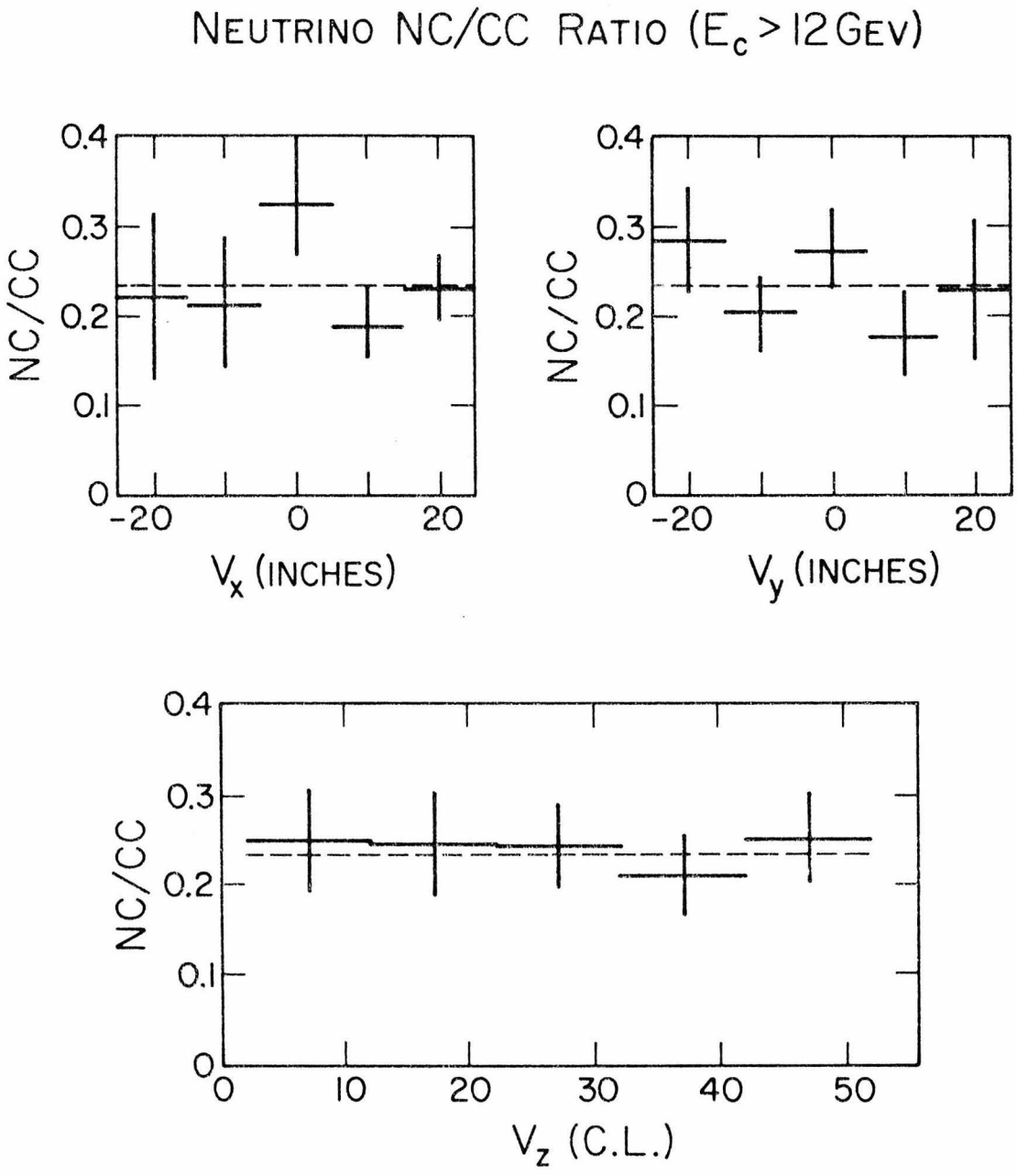

Figure 7-2: The ratio of NC to CC events is plotted as a function of position of the hadron vertex in the calorimeter. Both transverse and longitudinal projections are shown (the longitudinal position is measured in collision lengths). Backgrounds from CC events with missed muons or from neutrons, had they existed, would have appeared near the edges of these plots.

the edges of the calorimeter, the flatness of the plots in figures 7-2a and 7-2b provides a check on the separation of NC and CC events. Backgrounds from neutrons or cosmic rays would also produce an increase in NC/CC near the edges of the plots.

The NC/CC ratios of total observed events were R_{ν}^{obs} = .238 ± .022 and $R_{\bar{\nu}}^{obs}$ = .34 ± .09. These ratios only include the data above E_c = 12 Gev, however, and the extrapolation to zero hadron energy would be different for NC and CC events if the shapes of the hadron energy distributions were different. In addition, the calorimeter energy E_c measured in CC events received a 3.7 Gev contribution from the muon. The cut in hadron energy was therefore different for CC and NC events, since the true hadron energy of a CC event was $E_h = E_c - 3.7$ Gev, while $E_h = E_c$ for NC events. These partial ratios of events above E_c = 12 Gev are therefore not quantitatively very significant.

Moreover, the ratios of NC to CC events depend on the CC cross-sections. If there were scale-breaking effects in the charged currents at high energy, these ratios might change as a function of E_ν even though the NC interaction scaled. Ideally, the neutral currents should be analyzed independently of the charged currents insofar as this is possible.

7.3 METHOD OF DETERMINING THE NC COUPLING

Equations 7-1 can be rewritten in terms of an overall neutral current coupling constant g_{nc} and the fractional positive-helicity coupling P:

$$\frac{d\sigma^{\nu}}{dy} = \overline{E}\, g_{nc} [\, (1 - P) + P\,(1 - y)^2\,] \qquad (7\text{-}3a)$$

$$\frac{d\sigma^{\bar{\nu}}}{dy} = \overline{E}\, g_{nc} [\, (1 - P)\,(1 - y)^2 + P\,] \qquad (7\text{-}3b)$$

This parameterization is useful since it isolates the coupling

strength g_{nc} from the coupling structure, which is determined by the positive-helicity component P (see Appendix B). P is therefore the parameter in which we are most interested.

In a narrow band beam, the E_h distributions of neutrino events reflect the y-distributions, since $E_h = E_\nu y$. In principle, P could be determined by fitting the relative amounts of flat and $(1-y)^2$ components in the E_h distributions. In practice, the width of the neutrino energy bands as well as the resolution in hadron energy measurement tended to smear the structures of the E_h distributions expected from the pure negative-helicity and pure positive-helicity couplings, and made it more difficult to extract information from the shape of the measured distributions. A more powerful determinant of P was the ratio of the total ν and $\bar{\nu}$ neutral current signals. P is related to the cross-section ratio by

$$\frac{\sigma^{\bar{\nu}}_{NC}}{\sigma^{\nu}_{NC}} = \frac{1 + 2P}{3 - 2P} \qquad (7\text{-}4)$$

obtained by integrating equations 7-3. Since this ratio increases by a factor of 9 as P changes from 0 to 1, it is very sensitive to the size of the positive-helicity component.

The relative normalizations of the ν and $\bar{\nu}$ fluxes were therefore important, since they were needed to normalize the ν and $\bar{\nu}$ data. The positions and shapes of the low- and high-energy bands in the incident neutrino spectra were calculated from the optics of the narrow band beam as described in Chapter 2. The sizes of these bands were determined by fitting them to the measured CC data (Class 1 and Class 2 events) as described in Chapter 6.

When the incident neutrino and antineutrino spectra had been determined in this way, they were used to generate two sets of hadron energy distributions: a pure negative-helicity distribution ($d\sigma/dy \propto 1$ for neutrinos and $d\sigma/dy \propto (1-y)^2$ for antineutrinos) and a pure

positive-helicity distribution ($d\sigma/dy \propto (1-y)^2$ for ν and $d\sigma/dy \propto 1$ for $\bar{\nu}$). The neutrino and antineutrino neutral current data were then simultaneously fitted by a linear combination of these pure N and pure P hadron energy distributions. The fitted coefficients were just the positive- and negative-helicity coupling constants g_n and g_p of equation 7-1.

The Monte-Carlo program used to generate these neutral current hadron energy distributions was the same one used to generate the CC distributions shown in Chapter 6. The measured resolutions in hadron energy and the effect of the 12 Gev cut in E_h were of course included in the calculation. All statistical errors in flux calculations and background subtractions were also included.

7.4 NC COUPLING IN A SCALING MODEL WITH $\alpha = .17$

The flux ratios and CC subtraction depended somewhat on the particular model used to fit the CC data. We will first use the best fit of $\alpha = .17$ in the scaling model, and will consider this case in some detail. Other values of α and other models will be considered in section 7-5.

The calculated CC subtractions in the scaling model were shown in figure 7-1. The corresponding hadron energy distributions of CC and NC events are compared in figure 7-3. The dashed curve through the CC data is the distribution calculated from the scaling model, with $\alpha = .17$. The solid curve through the NC data is the best fit assuming the form of equation 7-3, and corresponds to P = .36; for comparison, the dotted curve is the distribution expected for pure negative-helicity coupling (P=0).

The two features of shape and relative normalization mentioned above are clear in this figure. The best fit, with P = .36, fits the shape of both the ν and $\bar{\nu}$ data better than the pure N coupling does. But the more important factor is the relative normalization of the ν

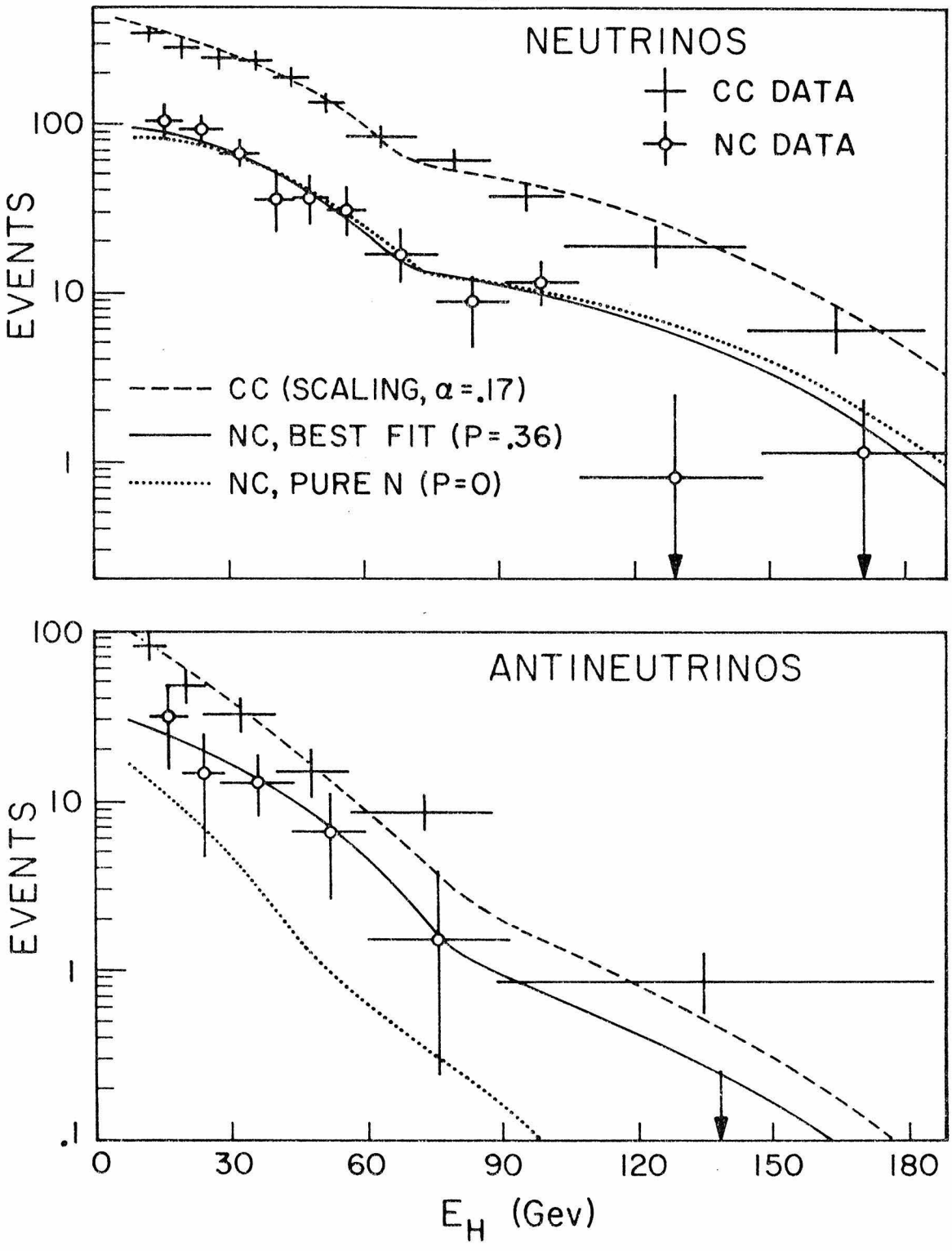

Figure 7-3: The best fits to NC and CC data in the scaling model are shown for both ν and $\bar{\nu}$. Normalization is determined by Class 1 and 2 CC data. For comparison, the best NC fit for a pure negative-helicity coupling is also shown.

and $\bar{\nu}$ events. A smaller value of P would predict too few $\bar{\nu}$ events relative to the ν events, and a larger value of P would predict too many.

The ratios of neutral to charged current total cross-sections, extrapolated to zero hadron energy under the assumption of scaling with $\alpha = .17$, were

$$R^{\nu}_{obs} = .266 \pm .024 \qquad (7\text{-}5a)$$

$$R^{\bar{\nu}}_{obs} = .395 \pm .077 \qquad (7\text{-}5b)$$

The best values obtained for the NC coupling constants under these assumptions were

$$g_n = .199 \pm .023 \qquad (7\text{-}6a)$$

$$g_p = .110 \pm .037 \qquad (7\text{-}6b)$$

or in terms of g_{nc} and P,

$$g_{nc} = .309 \pm .035 \qquad (7\text{-}7a)$$

$$P = .357 \pm .092 \qquad (7\text{-}7b)$$

P can be expressed in terms of the antiquark component α and the V+A component β (see Appendix B):

$$P = \alpha + \beta - 2\alpha\beta \qquad (7\text{-}8)$$

A pure vector coupling would require $P = \beta = 1/2$ (independent of α). If the coupling were pure V-A, then the P component would be due solely to antiquarks in the nucleon, so $\beta = 0$ and $P = \alpha$. If the coupling were pure V+A, then $\beta = 1$ and $P = 1-\alpha$.

These three possible kinds of coupling are compared to the best fit values of g_n and g_p in figure 7-4. Pure V+A is clearly ruled out, and the best fit lies approximately midway between V and V-A (1.6 standard deviations from pure V and 2.0 from pure V-A). The data therefore do not support either a pure V or a pure V-A coupling scheme, but neither of these can be conclusively ruled out.

Pure V and pure V-A couplings are attractive because of their apparent simplicity (i.e., "purity"), but in general the neutral current is expected to couple through a mixture of V+A and V-A. In the Weinberg-Salam model[10], which is the most familiar of the gauge theories, the V+A and V-A couplings (g^+ and g^-) in ν-N scattering are both expressed[43] in terms of a single parameter $\sin^2\theta_W$:

$$g^- = \frac{1}{2} - \sin^2\theta_W + \frac{5}{9}\sin^4\theta_W \qquad (7\text{-}9a)$$

$$g^+ = \frac{5}{9}\sin^4\theta_W \qquad (7\text{-}9b)$$

(These formulas neglect the effect of the Cabibbo angle and the small possible contribution from strange and charmed quarks.) This only allows pure V-A if $\sin^2\theta_W = 0$, and allows A only if $\sin^2\theta_W = 1/2$.

The g_n and g_p couplings are given in terms of these by

$$g_n = (1-\alpha)\, g^- + \alpha\, g^+ \qquad (7\text{-}10a)$$

$$g_p = (1-\alpha)\, g^+ - \alpha\, g^- \qquad (7\text{-}10b)$$

Equations 7-9 and 7-10 define a Weinberg curve in the g_n-g_p plane, as shown in figure 7-4. Fitting the Weinberg angle to the NC data gives a best value of

$$\sin^2\theta_W = .331 \pm .057 \qquad (7\text{-}11)$$

It is clear from the figure that the Weinberg theory is perfectly

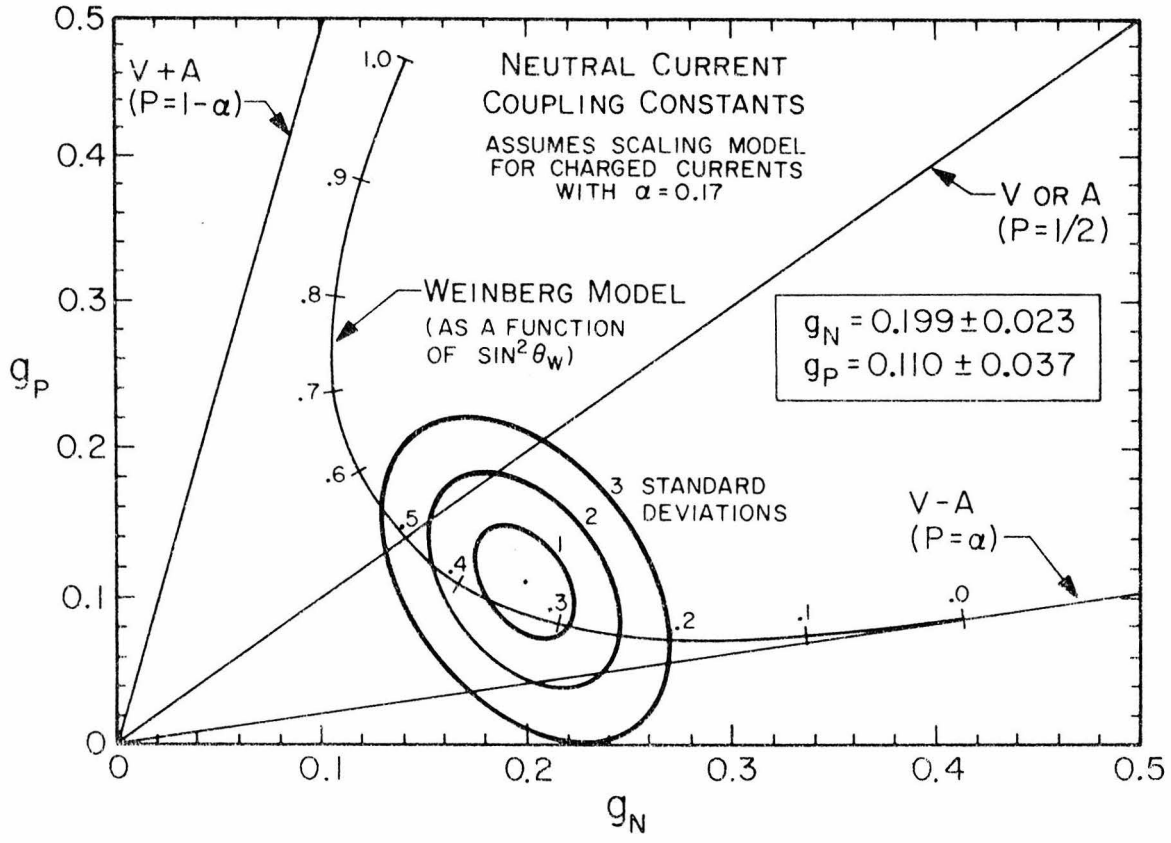

Figure 7-4: The negative- and positive-helicity coupling parameters, obtained by fitting the neutral current E_h distributions of figure 7-3, define a point in the plot of g_n versus g_p above. The elliptical contours surrounding the point indicate the statistical error.

The straight lines corresponding to pure V-A, pure V or A, and pure V+A coupling are drawn for comparison. None of these gives a good representation of the data; the best fit lies halfway between V-A and V.

The curve predicted by the Weinberg theory is also drawn, and agrees with the data for $\sin^2\theta_W = .33 \pm .06$.

consistent with the data and gives a better fit than either pure V or pure V-A.

7.5 DEPENDENCE ON CC ASSUMPTIONS

The errors given above include only the statistical errors in the data (both NC and CC) and the systematic errors discussed in Chapter 5. They do not include systematic errors due to uncertainties in the assumptions made about the charged currents. The charged currents have entered into the calculation of P and g_{nc} in only two ways: (1) in the determination of the CC subtraction parameters ϵ_ν and $\epsilon_{\bar{\nu}}$, and (2) in the determination of the fluxes F_ν and $F_{\bar{\nu}}$. With any particular model of the CC events, each of these quantities can be calculated from the CC data. To be as general as possible, we have tried using several different classes of models, each of which has a free parameter which is fitted to the data. The uncertainties in the CC subtractions and in the fluxes are determined by the precision with which the parameters are determined in these models.

The three models used, which were discussed in Chapter 6, are (a) scaling model, with free parameter α; (b) non-scaling model, with $\alpha_\pi = .17$ and variable α_K; and (c) B-quark model, with $\alpha = .06$ and M_B as the variable parameter. In figures 7-5 the possible variations in ϵ_ν, $\epsilon_{\bar{\nu}}$, and $F_{\bar{\nu}}/F_\nu$ are shown for each of these models.

Note that the CC subtraction is larger for neutrinos than for antineutrinos. This is because the antineutrino y-distribution is predominantly $(1-y)^2$, and there are fewer events at large y and hence at large angle.

Scaling model

As α increases in the scaling model, the short-length CC subtraction becomes larger for antineutrinos and smaller for neutrinos (figures 7-5a and 7-5b), since the antiquarks contribute a flat-y

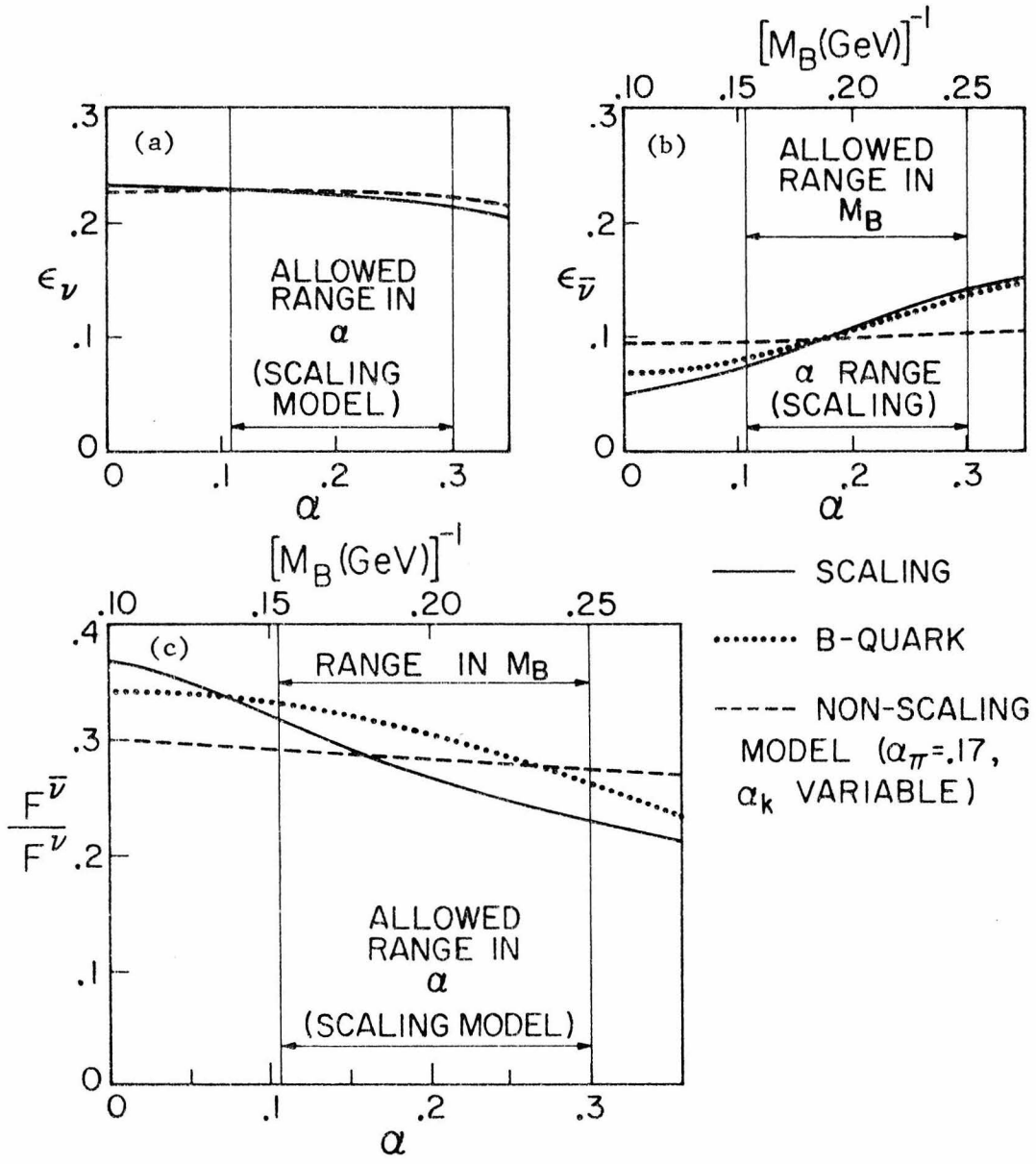

Figure 7-5: The fractions of CC events with "missed muons" ($P \leq 16$) and the ratios of incident fluxes (weighted with energy) calculated from each of the three classes of models are compared above.

$$\epsilon_{\nu,\bar\nu} = \frac{\text{CC events with } P \leq 16}{\text{all CC events}} \quad \text{and} \quad F^{\nu,\bar\nu} = \left[\int E\,\rho(E)\,dE\right]^{\nu,\bar\nu}$$

The curves from the B-quark model are plotted as a function of M_B (upper axis), and the scaling and non-scaling curves are plotted as functions of α and α_K, respectively (lower axis). The axes are chosen so that the allowed regions of the variable parameters overlap.

component to $\bar{\nu}$ and a $(1-y)^2$ component to ν. The change in ϵ is much greater for antineutrinos since the $\bar{\nu}$-$\bar{Q}$ cross-section is three times greater than the $\nu - \bar{Q}$ cross-section. This difference is due solely to the difference in y distributions.

The change in calculated flux ratios occurs for this reason also. As α increases, the $\bar{\nu}$ cross-section increases as $1+2\alpha$ due to the higher cross-section of the antiquarks. The calculated flux must decrease by the same factor in order to give the same total number of observed events. The neutrino cross-section varies by a much smaller relative amount, again due to the cross-section difference between $\nu - \bar{Q}$ and $\bar{\nu} - \bar{Q}$.

The effect of changing α thus has a much greater effect on the $\bar{\nu}$ distributions, and on $\epsilon_{\bar{\nu}}$ and $F_{\bar{\nu}}$, than it has on the ν-distributions.

Non-Scaling α

In this model, α_π and α_K are allowed to vary independently. However, the dependence of $\epsilon_{\nu,\bar{\nu}}$ and $F_{\nu,\bar{\nu}}$ on α_K is very weak. For fixed α_π, the non-scaling model gives almost the same results as the scaling model.

In the antineutrino distributions, this is due to the small size of the $\bar{\nu}_K$ flux relative to the $\bar{\nu}_\pi$ flux. The neutrino distributions, which are not very sensitive to changes in α in the scaling model, are even less sensitive to changes in α_K alone. The muon detection efficiency for ν_K events is less sensitive than the ν_π events to changes in α, and the $\bar{\nu}_K$ events account for less than half of the total signal. Varying α_K alone therefore has relatively little effect on either the efficiencies or fluxes.

This indicates that the values determined for P and g_{nc} are not very sensitive to the very high energy (>80 Gev) behavior of the charged currents. The more important uncertainties are in the $\bar{\nu}$ distributions in the range $E \approx 40$-60 Gev.

B-quark model

This model affects only antineutrino CC distributions, but affects them in a very drastic way. At asymptotic energies production of B-quarks would dominate the $\bar{\nu}$ interactions; because of the difference in y distributions, B-quark production would be three times greater than d-quark production as $E_{\bar{\nu}} \rightarrow \infty$.

In the 40-60 Gev range, threshold effects play a major role. The B-quarks are produced mainly at large y, and therefore have an effect similar to antiquarks in that they increase the $\bar{\nu}$ cross-section and also increase the CC subtraction for $\bar{\nu}$. If the B-quark mass is lower, the threshold is reduced and the effects become larger. The effects on $\epsilon_{\bar{\nu}}$ and $F_{\bar{\nu}}/F_{\nu}$ of B-quark production and antiquark scattering are compared in figures 7-5b and 7-5c.

In all of these models, a decrease in $F_{\bar{\nu}}/F_{\nu}$ corresponds to an increase in $\epsilon_{\bar{\nu}}$ for antineutrinos. This correlation is important, since the two changes affect the value of P in opposite ways, and tend to cancel. That is, an increase in $\epsilon_{\bar{\nu}}$ decreases the total number of $\bar{\nu}$ NC events, and therefore decreases the calculated $\bar{\nu}$ cross-section; but a decrease in $F_{\bar{\nu}}$ requires a higher cross section to produce the observed number of NC events, and therefore increases the calculated $\bar{\nu}$ cross-section. The variation in ϵ_{ν} is smaller in all of these models.

The total variations in P and g_{nc} are shown in figures 7-6a and 7-6b. The CC analysis places limits on α of (.11,.28) and on M_B of (4,6) Gev; the approximate ranges of these variations are indicated in the figures. Figure 7-6b shows that larger values of α and smaller values of M_B give slightly higher values of P. This indicates that the flux variations in the models are somewhat more important than the variations in efficiency. In any case, the model-dependent variations in P and g_{nc} are considerably smaller than the statistical uncertainties.

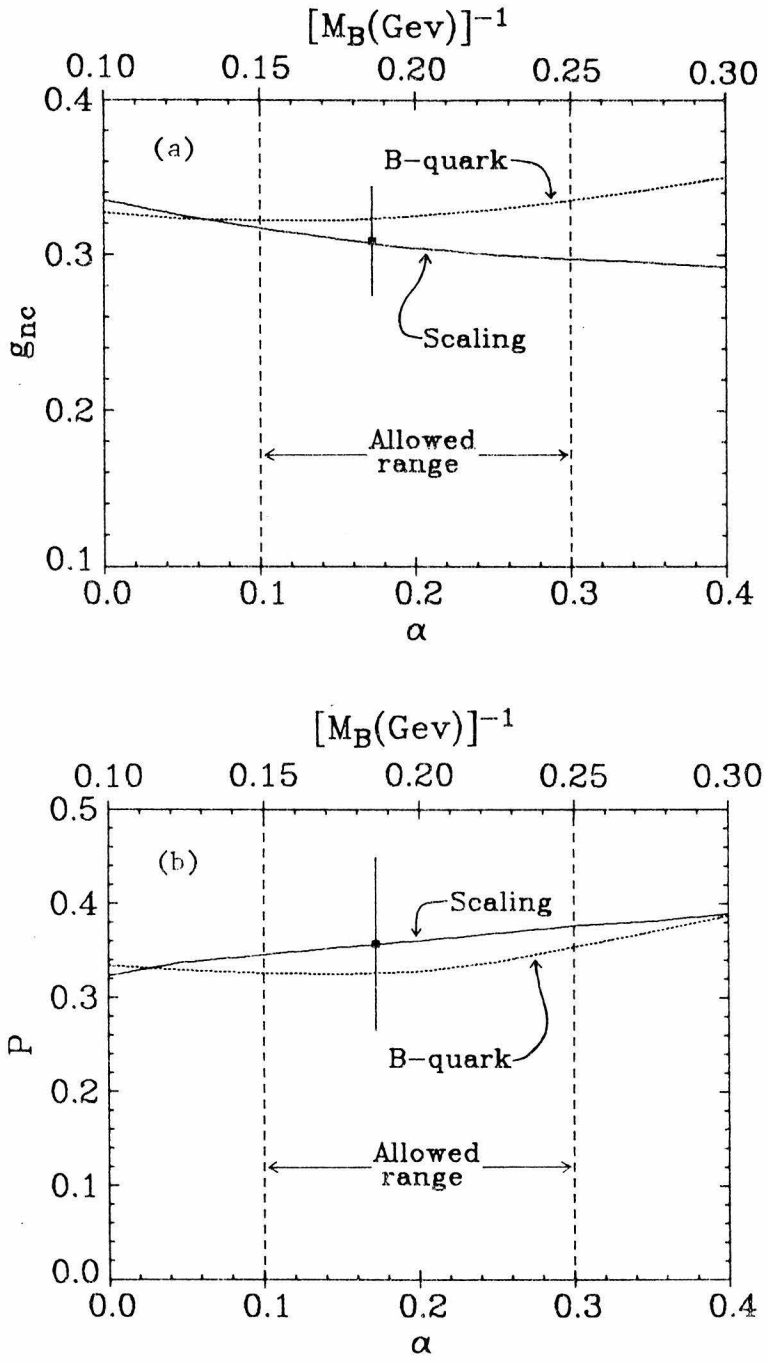

Figure 7-6: The variations in g_{nc} and P obtained with the scaling and B quark models are plotted as functions of the variables α and M_B. The statistical error for the scaling point with α=.17 is drawn for comparison. The models with $\alpha_\pi \neq \alpha_K$ (not drawn) give results almost identical with the scaling model using the same value of α_π (independent of α_K).

Other variations in the charged currents were considered. For example, the shape of the x-distribution was varied by multiplying the expression for $F_2(x)$ from e-N scattering by an extra factor of $(1-x)$. Using $F_2'(x) = F_2(x)\ (1+b(1-x))$ in place of $F_2(x)$, b was varied to see if ϵ_ν for neutrinos might be sensitive to variations in the x-dependence. Within the limits of $b = \pm.5$ imposed by the measured x distributions of Class 1 events, the variation in muon detection efficiency was less than that obtained by varying α. This result was anticipated for the reasons discussed in section 6-3.

7.6 MODEL-INDEPENDENT ANALYSIS

If the charged-current distributions are represented by any of the models discussed above, then the best values of P and g_{nc} can be read directly from figures 7-6a and 7-6b. It is not in fact necessary for the details of the models to be correct -- if the values of ϵ_ν, $\epsilon_{\bar{\nu}}$, and $F_{\bar{\nu}}/F_\nu$ obtained from them are correct, then the resulting values of P and g_{nc} are also correct.

However, one would like to be able to analyze the neutral current data without recourse to specific charged-current models. We can do this, to an extent, by restricting ourselves to particular kinematic regions in calculating fluxes and efficiencies. In this section, we will use only the wide-angle data in estimating efficiencies, and use only the low-y data in calculating fluxes. This reduces the model dependence considerably, but produces larger statistical errors and somewhat larger total errors in P and g_{nc}, since less information is used.

Internal estimate of muon detection efficiency

About half of the inefficiency in muon detection is purely geometrical. For example, a CC interaction producing a wide-angle muon near the edge of the apparatus may be clearly identifiable (P>16) if the azimuthal angle of the muon points back toward the center of

the apparatus. The same event would be in the $P \leq 16$ region if the azimuthal muon angle were rotated by 180°, so that the muon escaped out the side of the apparatus before passing through enough steel. This part of the detection inefficiency can be calculated from the data by azimuthally rotating the muon production angle of each CC event in the $P \geq 16$ region about the beam direction, and calculating the detection efficiency for that event. This method in fact generates a distribution of "azimuthally missed" short-length events from the observed wide angle long-length events.

Not all of the missed muons were included in this calculation since very wide-angle muons ($\theta_\mu > 450$ mrad) were never detected at all, and even events with moderately wide-angle muons (>300 mrad) which occurred near the center of the apparatus were also never detected. The Monte-Carlo program was used to estimate the fraction of the total CC subtraction at each hadron energy that was not accounted for by the azimuthal rotation. The "azimuthally missed" distribution was corrected accordingly, as a function of hadron energy.

This method has two very nice features: (1) the part of the subtraction obtained by rotating events is totally independent not only of the physics assumptions, but also of the assumed energy and spatial distributions of the beam, and (2) the remaining part of the correction uses the data at moderately large y and θ_μ to estimate the data at very large y and θ_μ; any slow deviations from the assumed θ_μ and y dependence are therefore automatically taken into account.

The only drawback to this extrapolation procedure was that it depended on the very wide-angle CC data. Since the first part of the muon track was always obscured by the hadron shower, these were the events in which it was most difficult to find the muon track. In about 15% of the events which might have contributed to the azimuthal extrapolation, the muon track was unsatisfactory -- either it did not extrapolate back to the vertex, had too large a spark scatter, or had

too few sparks for a track to be found. These events could not be directly used in the extrapolation; they were assumed to have the same efficiency as the events with good tracks, and the azimuthal extrapolation was corrected accordingly.

The regions of large y populated by the P>16 data and by the azimuthally extrapolated events are shown in figure 7-7, calculated in the scaling model with $\alpha = .17$. The only region of y which depended strongly on the Monte-Carlo extrapolation was the region of very large y (y>.8).

The total subtraction of short-length CC neutrino events calculated in this manner was 404 ± 32, as compared to 430 ± 14 in the scaling model calculation. The azimuthal extrapolation and the total correction are shown in figure 7-8. The resulting partial NC/CC ratios obtained by this procedure were

$$R_{\nu} = .255 \pm .030 \qquad (7\text{-}12a)$$

$$R_{\bar{\nu}} = .30 \pm .11 \qquad (7\text{-}12b)$$

which are consistent with the values obtained from the scaling model (see section 7-2). The statistical errors resulting from the azimuthal extrapolation were larger, since only a fraction of the data was used to calculate the inefficiency.

Flux ratios from y-intercepts

The calculated flux ratio $F^{\bar{\nu}} / F^{\nu}$ varied in the different CC models because the ν and $\bar{\nu}$ cross-sections varied as a function of α and M_B. The cross-sections at y = 0, however, have a more basic symmetry that is respected by all of these models:

$$\left.\frac{d^2\sigma^{\nu}}{dxdy}\right|_{y=0} = \left.\frac{d^2\sigma^{\bar{\nu}}}{dxdy}\right|_{y=0} = \frac{G^2 M E}{\pi} F_2(x) \qquad (7\text{-}13)$$

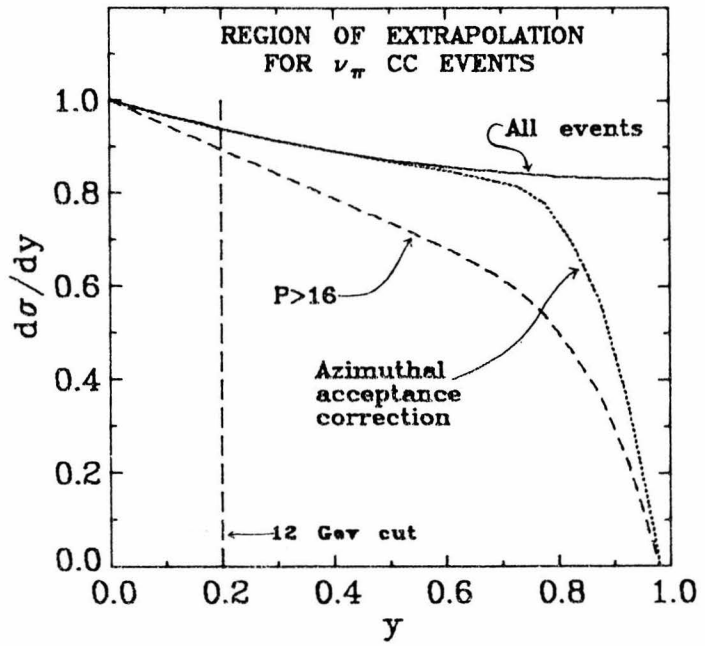

Figure 7-7: The acceptances in y are compared for P > 16 events and P > 16 events plus the azimuthal correction.

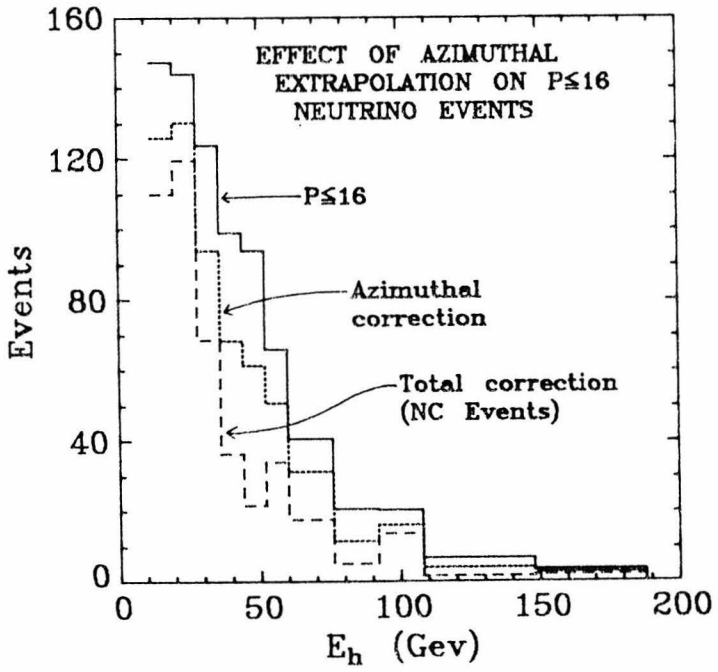

Figure 7-8: Comparison of the effects of the azimuthal and total corrections to the low-penetration region.

This relation is clearly satisfied by the scaling model for any value of α, as seen from equation 6-1; it also would not be affected by B-quark production since y must be fairly large to be above the threshold for B-quark production. In fact, from equation (A-5), it can be seen that (7-13) is valid if neutron-proton charge symmetry is valid in the low-y region, even if the parton model, scaling, and the Callan-Gross relation all fail.

Proton-neutron charge symmetry in the weak interaction is not exact, and is broken at the 5% level by strange-particle production (see Appendix A). As an approximate symmetry in the low y region, though, it is very fundamental [44], and has been experimentally verified in the region of low q^2 and ν by both the Caltech[19] and Gargamelle[18] experiments.

It should be noted that a violation of this symmetry, based on data obtained by the HPWF group, has been reported by D. Cline[45]. The violation occurs in the region of small x ($x<.1$), where the $\bar{\nu}$ cross-section is reported to be smaller than the ν cross-section by at least a factor of 2 over all y (including $y \rightarrow 0$). This result has been very controversial, and is in apparent disagreement with the Caltech[34] and Gargamelle data. In any case, the reported violation occurs only in the low x region; the y-distributions of all the data together are consistent with the shape of a scaling distribution with 10% antiquarks[44].

The Caltech group has recently completed a normalized total cross-section CC experiment covering a wide range of incident neutrino energies. A preliminary analysis of a fraction of this data shows no indication of a violation of charge symmetry at low y, and confirms equation 7-13 at the 20-30% level at energies up to 100 Gev[46]. The complete analysis of this data should provide a test of charge symmetry at the 10% level.

For the present, therefore, we have assumed that charge symmetry is valid in the low y region, and have used only the CC data in the region $0 \leq y < .2$ to determine the flux normalization of the neutral current data. This method of determining fluxes is not unrelated to the model-dependent methods, since the fluxes calculated from the models also used the low y data and assumed equation 7-13; but using only the data at low y frees us from having to assume a specific model to fit the charged current distributions and cross-sections. The statistical errors are of course somewhat larger.

The flux ratios obtained from the low-y region of the CC data were

$$F_{\pi}^{\nu} \; / \; F_{K}^{\nu} \; / \; F_{\pi}^{\bar{\nu}} \; / \; F_{K}^{\bar{\nu}} \;\; = \;\; 1.00 \; / \; .57 \; / \; .43 \; / \; .044 \qquad (7\text{-}14)$$

where $F_{\pi}^{\nu} = \int E_{\pi}^{\nu} \, \rho(E_{\pi}^{\nu}) \, dE_{\pi}^{\nu}$, etc. These are the ratios of the y intercepts of figures 6-5 through 6-8, with ~20% corrections due to differences in spectral shape and acceptance, and to minor differences in the event criteria used in the CC analysis.

Combining this method of determining fluxes with the azimuthal extrapolation to determine acceptances for wide-angle muons, the NC distributions can be determined and normalized with relatively little dependence on models. These distributions are shown in figure 7-8. The values of P and g_{nc} obtained by fitting these distributions with equation 7-3 are

$$g_{nc} = .32 \pm .05 \qquad (7\text{-}15a)$$

$$P = .38 \pm .13 \qquad (7\text{-}15b)$$

which are consistent with all of the values obtained with the different CC models. Statistical errors are larger in this model-independent analysis since less information is used.

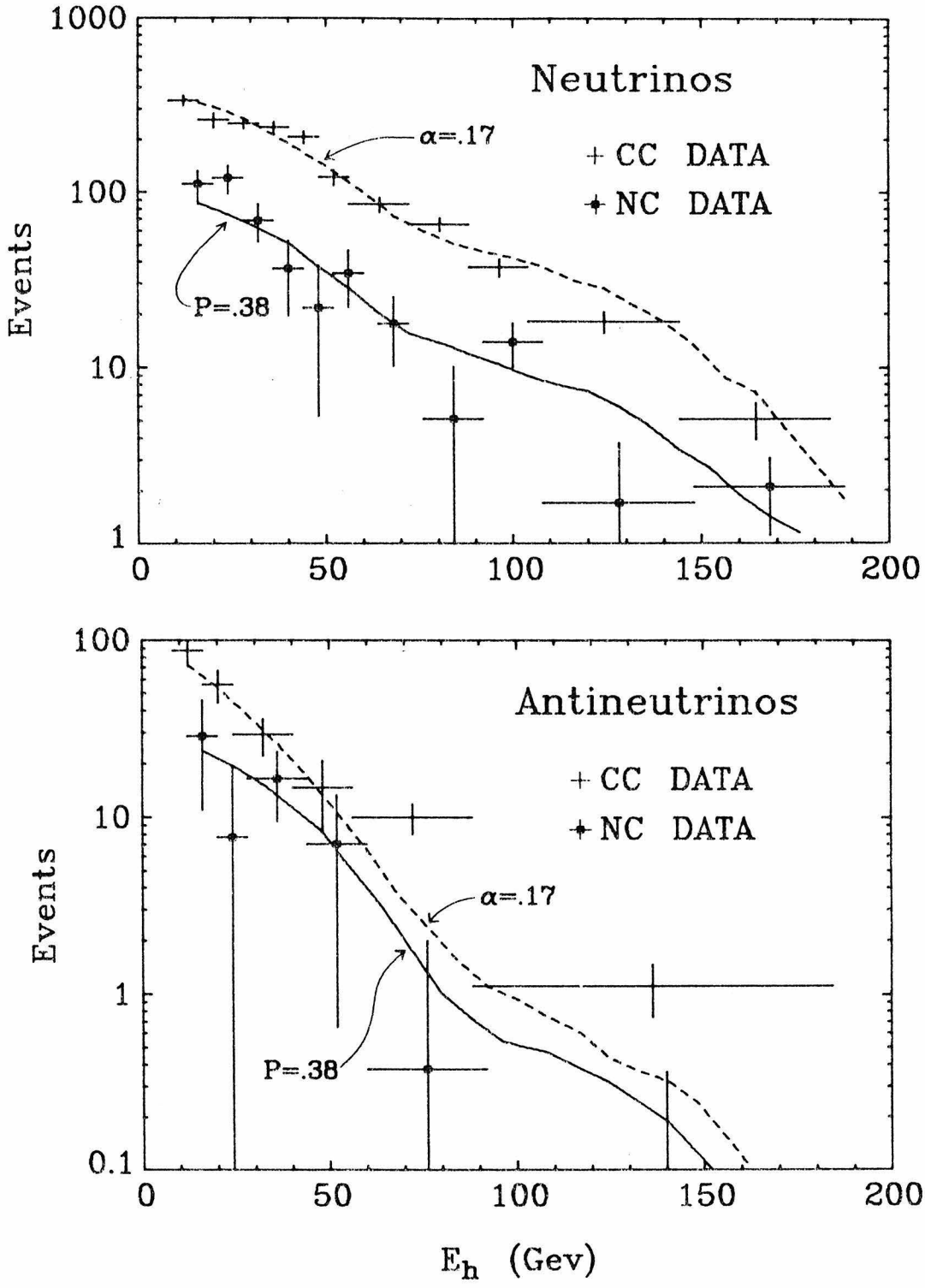

Figure 7-8: The NC and CC distributions obtained using the model-independent techniques of azimuthal extrapolation for part of the CC subtraction and y-intercepts for normalization are compared to the scaling predictions. The best fit to the NC distributions gives $P = .38 \pm .13$.

7.7 CONCLUSIONS

The distributions we have measured are consistent with a scaling neutral current which couples through a combination of V and A. The values of g_{nc} and P obtained with the scaling model of charged currents ($\alpha = .17$) lie approximately in the center of the ranges indicated by both the charged current models and model-independent analysis, and we use these as our nominal "best values" of the coupling. Taking into account both the model dependent and model independent analyses, we conclude that

$$g_{nc} = (.31 \pm .02) \pm .02 \qquad (7\text{-}16a)$$

$$P = (.36 \pm .04) \pm .09 \qquad (7\text{-}16b)$$

The inner errors are the systematic errors obtained by varying the charged-current assumptions, and the outer errors are the statistical errors (primarily due to the $\bar{\nu}$ distributions). As more becomes known about the charged currents, slight modifications might be made to these values by using the model-dependent variations shown in figure 7-6.

To compare the value of P in equation (7-16b) to a pure V-A coupling requires a knowledge of the antiquark fraction α. Pure V-A would require $\alpha = .36 \pm .10$. This is 1 - 2 standard deviations away from the range of α obtained from the ν_{μ} and $\bar{\nu}_{\mu}$ data. If we assume that the fractional antiquark component for neutral currents (α_{nc}) is the same as for charged currents (α_{cc}), then the comparison of the data to pure V-A can be read directly from figure 7-6b.

However, the best fit to α_{cc} from this data is higher than that expected from low energy experiments. A possible explanation for this is that the charged currents deviate from scaling through the production of B-quarks or through some similar mechanism. If this is the case, the antiquark fraction α_{nc} would still be expected to be independent of energy, even though the "effective α_{cc}" obtained by

fitting the charged-currents with a scaling model would increase with energy. The best measure of α_{nc} might then be the value of α_{cc} obtained in the low energy experiments (.06-.10), and a pure V-A coupling would predict $P = \alpha_{nc} \approx .06-.10$. The value of P obtained in this experiment is more than two standard deviations away from this range in all the models tried.

The data therefore do not support a V-A coupling in any of the models used.

The comparisons to pure V and pure A are less model-dependent, since these couplings require P=.5 regardless of the value of α_{nc}. The value of P determined in this experiment lies about 1.2 - 2.0 standard deviations away from P=.5 in all of the different CC models used.

In general, the Weinberg model (as defined by equations 7-9 and 7-10) agreed more closely with the data than either pure V or pure V-A. In all of the CC models tried, the Weinberg theory agreed with the neutral current distributions to within better than 1.25 standard deviations; in the scaling model, with $\alpha \geq .17$, the agreement was better than .5 s.d. The best fit to $\sin^2\theta_W$ was within the range .30-.34 in all of these models. The best value for the Weinberg parameter determined from the data of this experiment is therefore

$$\sin^2\theta_W = .33 \pm .07 .$$

7.8 COMPARISON TO OTHER EXPERIMENTS

Two other deep-inelastic neutral current neutrino experiments have been carried out, by the Gargamelle collaboration and by the HPWF group at Fermilab. The results of these and the Caltech experiment all appear to be reasonably consistent, although errors are large in each experiment.

Results are usually quoted as ratios of observed NC/CC events, but since the type of neutrino beam, the incident neutrino energy range, and the cut in E_h differ for all of these experiments, these ratios are not the most meaningful ones to compare. The most important number in determining the type of coupling is the positive-helicity component P or, equivalently, the cross-section ratio $\sigma^{\bar{\nu}}_{nc} / \sigma^{\nu}_{nc}$. This ratio, as well as the partial NC/CC ratios R^p_ν and $R^p_{\bar{\nu}}$ are compared for each of the experiments in the tables below. Since there has been a great deal of recent activity in these experiments, and since there is a time lapse between analysis and publication, the most recent published results of each of the experiments differ from their most recent results announced at conferences or in preprints. Both sets are included in tables 7-1 and 7-2 below.

Table 7-1: Published neutral current ratios.

Experiment	R^p_ν	$R^p_{\bar{\nu}}$	$\sigma^{\bar{\nu}}_{NC} / \sigma^{\nu}_{NC}$
Gargamelle[4]	$.22 \pm .03$	$.43 \pm .12$	Not given ($\approx .66 \pm .20$)
HPWF[7]	$.11 \pm .05$	$.32 \pm .09$	Not given ($\approx 1.2 \pm .6$)
Caltech-Fermilab[6]	$.22 \pm .11$	$.33 \pm .16$	Not given ($\approx .6 \pm .4$)

Table 7-2: Most recently announced results.

Experiment	R_{ν}^{p}	$R_{\bar{\nu}}^{p}$	$\sigma_{NC}^{\bar{\nu}} / \sigma_{NC}^{\nu}$
Gargamelle[47]	$.22 \pm .03$	$.55 \pm .07$	Not given ($\approx .69 \pm .16$)
HPWF[48]	$.29 \pm .04$	$.39 \pm .10$	$\leq .61 \pm .25$ Best fit: $.48 \pm .20$
Caltech-Fermilab (this thesis)	$.24 \pm .02$	$.34 \pm .09$	$.75 \pm .15$

Several qualifications need to be made with regard to these tables. In the right-hand column, the values in parentheses are my own calculation, and not that of the experimental groups. The Gargamelle collaboration has not quoted ratios of $\sigma_{nc}^{\bar{\nu}} / \sigma_{nc}^{\nu}$, but they have fitted the Weinberg model to their data and found $.30 < \sin^2\theta_W < .46$ from the ν data and $\sin^2\theta_W < .48$ from the $\bar{\nu}$ data. I have used $\sin^2\theta_W = .38 \pm .08$ and their most recent value of $\alpha = .10 \pm .03$ to compute $\sigma_{nc}^{\bar{\nu}} / \sigma_{nc}^{\nu}$ from equations 7-9 and 7-10. An analysis that does not assume the Weinberg theory might give a higher value for this cross-section ratio.

The HPWF collaborators also have not given the extrapolated NC/CC ratios, but have compared their data to various coupling schemes by requiring consistency between the extrapolated and predicted $\sigma_{nc}^{\bar{\nu}} / \sigma_{nc}^{\nu}$ ratios. They assume a 5% antiquark component, and obtain a best fit of "V-.8A" for the coupling. Assuming this value for the coupling gives them a cross-section ratio of $\sigma_{nc}^{\bar{\nu}} / \sigma_{nc}^{\nu} = .48 \pm .20$ (the error here does not include the error in the determination of the coupling parameter). In addition, they have compared their data to pure V and V-A couplings and are .9 standard deviations from V-A and 3.5 standard deviations from pure V.

There are two very noteworthy features of the results in table 7-2. In all three experiments, $R^p_{\bar{\nu}} > R^p_{\nu}$. In a V-A coupling scheme, these ratios should be equal if the charged-currents scale. If the anti-neutrino charged-current cross-section is increasing with energy (due to B-quark production or a similar mechanism), then the ratios should be equal at low energy but we should find $R^p_{\bar{\nu}} < R^p_{\nu}$ at higher energy. $R^p_{\bar{\nu}} > R^p_{\nu}$ indicates that the coupling is not pure V-A, but has a V+A component as well. On the other hand, if the coupling were pure V or pure A we would expect the cross-sections $\sigma^{\bar{\nu}}_{nc}$ and σ^{ν}_{nc} to be equal. All of the cross-section ratios in table 7-2 are at least 1.5 standard deviations less than 1; this indicates that the V-A component is larger than the V+A component.

Taken together, these three experiments give a strong indication that the NC coupling is neither pure V nor pure V-A, but a mixture of V-A and V+A with V-A dominating.

CHAPTER 8
MORE GENERAL COUPLING SCHEMES

In the previous chapter, we assumed that the neutral current scattering is only off of spin-1/2 partons, that only V and A couplings exist, and that the cross-sections σ_{nc}^{ν}, $\sigma_{nc}^{\bar{\nu}}$ scale. The data are consistent with these assumptions, but also allow the possibility of some more general coupling schemes. In this chapter, we will briefly examine some of the possibilities. In particular, we will try fitting the NC data with scalar, pseudoscalar, and tensor couplings, consider scattering off of scalar partons, and look for possible evidence of a Z_0 propagator.

8.1 POSSIBLE (1-Y) TERM

Scattering off scalar partons, in either charged or neutral currents, would produce a (1-y) component in the differential cross-section in addition to the constant and $(1-y)^2$ terms discussed previously. If the scalar partons were all neutral (or in general, were of only one charge), then they could not contribute to the charge-changing interaction, but could contribute to the neutral currents. This would allow a more general form of the NC interaction:

$$\frac{d\sigma^{\nu}}{dy} = \frac{G^2 M E}{\pi} \left[g_n + g_s (1-y) + g_p (1-y)^2 \right] \qquad (8\text{-}1a)$$

$$\frac{d\sigma^{\bar{\nu}}}{dy} = \frac{G^2 M E}{\pi} \left[g_n (1-y)^2 + g_s (1-y) + g_p \right] \qquad (8\text{-}1b)$$

In addition, it has been suggested that the neutral currents could couple through scalar, pseudoscalar, or tensor currents[13]. These are "helicity-flipping" couplings, and produce a right-handed final state neutrino (a new particle, if the neutrino is massless), rather than the usual left-handed one. A pure scalar or pure pseudoscalar coupling would produce a y^2 distribution for both ν and $\bar{\nu}$, and a pure tensor coupling would produce a $(2-y)^2$ distribution. In general, a combination of S, P, and T couplings, including interference terms, can produce the general distributions (8-1).

The best three-parameter fit to the NC distributions, assuming charged-current scaling with $\alpha = .17$ and using the form of equation (8-1), is compared to the data in figure 8-1. The special cases of pure S (or P) and pure T are also shown. A pure scalar coupling does not reproduce either the shape or relative normalization of the data, and is ruled out at the level of 6 standard deviations. A pure tensor coupling, however, fits the shape very well and in fact gives a slightly better overall fit than V and A couplings.

The best three-parameter fit to the NC distributions from equation 8-1 yields

$$g_n = .07 \pm .07 \qquad (8\text{-}2a)$$

$$g_s = .40 \pm .19 \qquad (8\text{-}2b)$$

$$g_p = -.02 \pm .07 \qquad (8\text{-}2c)$$

(The errors are of course correlated.) This fit violates a positivity constraint that $g_p \geq 0$, but only by a trivial amount. The important point is that a large (1-y) component is allowed.

This appears to be quite different from the earlier two parameter fit which gave $g_n = .199 \pm .023$ and $g_p = .110 \pm .037$. The two-parameter fit was consistent with the data, giving a χ^2 of 14.4 for 16 degrees of freedom. But the three-parameter fit, with a (1-y)

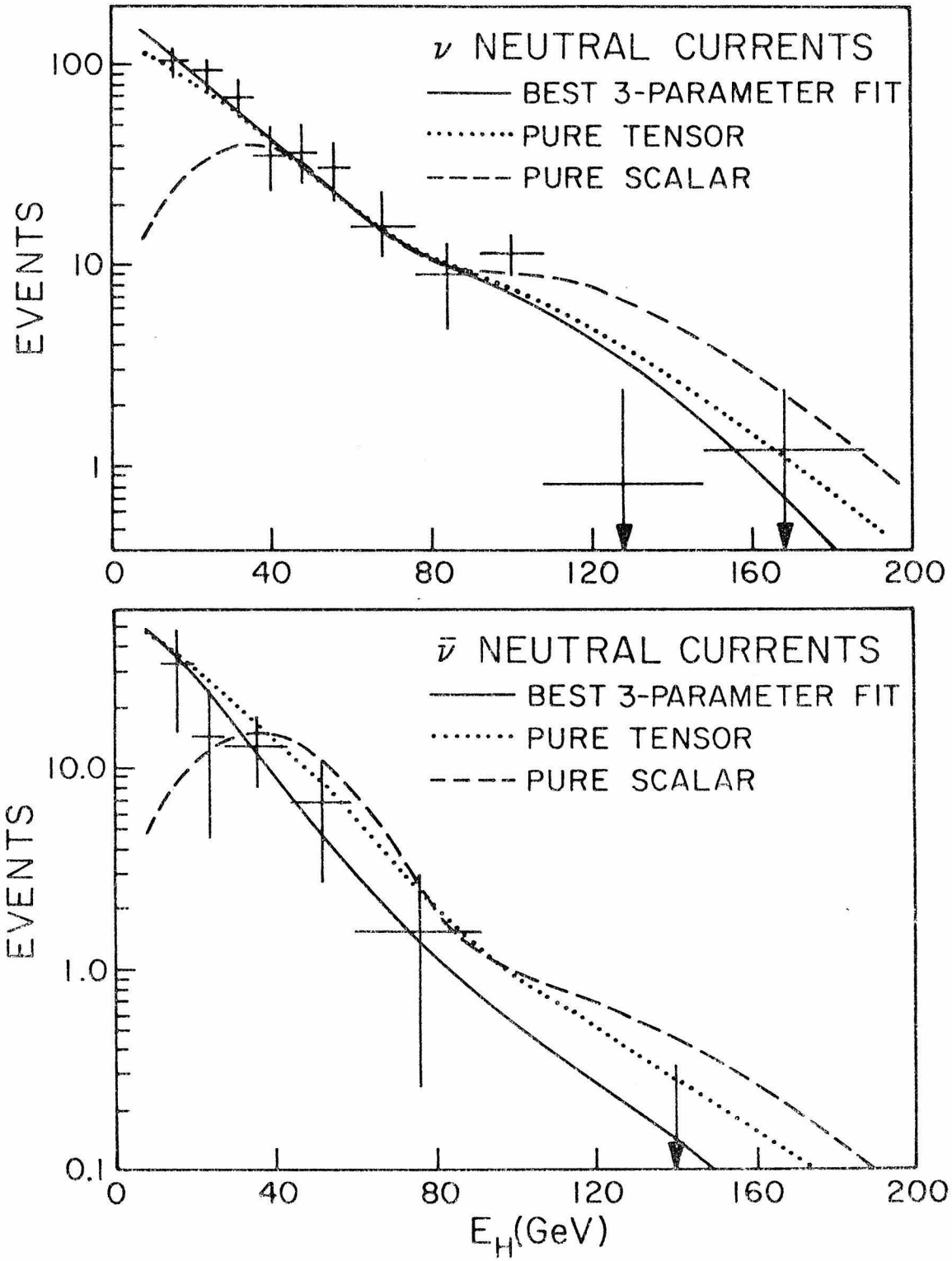

Figure 8-1: The NC data is compared to the distributions expected from tensor and scalar couplings, as well as to the best fit using the general form of equation 8-1.

term, gives a surprisingly good fit with $\chi^2 = 7.8$.

In fact, the fits are similar in most important respects. The total cross-section ratios in the two fits are similar, and agree within statistical error as shown in the table below. The three-parameter fit gives slightly larger values for both R_ν and $R_{\bar{\nu}}$ due to the increase in the extrapolation below E_h = 12 Gev. The most important difference between the fits lies in the shape of the predicted E_h distribution for neutrinos (the statistical errors in the antineutrino distribution are too large to give much sensitivity).

Table 8-1: Comparison of cross-section ratios of two and three parameter fits

	2-par. fit	3-par.fit
$\sigma^{\bar{\nu}}_{nc} / \sigma^{\nu}_{nc}$	.750 ± .141	.786 ± .173
$\sigma^{\nu}_{nc} / \sigma^{\nu}_{cc}$	.266 ± .024	.298 ± .028
$\sigma^{\bar{\nu}}_{nc} / \sigma^{\bar{\nu}}_{cc}$	.40 ± .08	.46 ± .08

Inspection of figure 7-3, which compares the best fit assuming only V and A couplings to the NC data, shows that the neutrino NC data falls somewhat faster with increasing hadron energy than the fit (the data is higher at low E_h and lower at high E_h). Fitting the ν distribution with a higher value of P would give a better fit to the shape of the neutrino data, but would predict a higher neutral current cross-section in the antineutrino data than that observed. This is because a larger $(1-y)^2$ component in the neutrino distribution forces a larger flat component in the antineutrinos.

This restriction no longer holds if a (1-y) term is included, since it contributes equally to the ν and $\bar{\nu}$ distributions and doesn't require events at larger y in either case. In fact, a large (1-y) component fits the shape of the data very well.

The data, therefore, are consistent with a large (1-y) component, which would be a departure from the expected V and A couplings. It should be emphasized, however, that the data are also consistent with only V and A couplings. The evidence in favor of the (1-y) term comes only from the shape of the neutrino E_h distribution, and not from the relative $\sigma_{nc}^{\bar{\nu}} / \sigma_{nc}^{\nu}$ normalization. The shape of the distribution is more sensitive to possible systematic errors than is the total measured number of events. For example, this shape depends critically on the number of NC events at large hadron energy. This is the region most sensitive to the CC subtraction and the K/π flux ratio. If there are deviations from scaling in the CC distributions, and in particular if the CC cross-section does not rise linearly, then this might somewhat distort the shape obtained for the NC distributions.

The values of g_{nc} and P calculated previously are not very sensitive to the large E_h region. In fact, the values obtained by fitting only the data below 60 Gev are

$$g_{nc} = .33 \pm .04 \qquad (8\text{-}3a)$$

$$P = .34 \pm .10 \qquad (8\text{-}3b)$$

which are within the quoted systematic errors of the earlier results.

8.2 POSSIBLE Z_0 PROPAGATOR EFFECTS

A deviation from the expected scaling behavior of neutral currents could occur because of the presence of a Z_0 propagator. If the Z_0 had low mass, then the NC cross-section would be altered at high energies:

$$\frac{d\sigma^2}{dxdy} = \left.\frac{d\sigma^2}{dxdy}\right|_{M_Z \to \infty} [\, 1 - M_Z^2 / q^2 \,]^{-2} \qquad (8\text{-}4)$$

This would reduce the cross-section at large E_h, and would cause the NC cross-section to decrease as a function of incident neutrino energy.

We have tried fitting our data with a Z_0 propagator (assuming only V and A couplings), but do not have much sensitivity to the Z_0 mass. We can fit the data with a large Z_0 mass and a small coupling constant ($g_{nc} \approx .3$), or with a small Z_0 mass and large coupling constant. From the shape of the E_h distributions alone, we can rule out Z_0 masses of less than 3 Gev at 90% confidence level.

But if there were a Z_0 with low mass, the cross-section measured at very low incident neutrino energy, where q^2 is low and the Z_0 has little effect, should be much higher than those measured in this experiment. The Gargamelle collaboration, which has observed NC events at low (1-11 Gev) energies, quote NC/CC cross-section ratios[49] of

$$R_\nu = .224 \pm .026$$
$$R_{\bar{\nu}} = .39 \pm .11$$

These are the ratios of total cross-sections, not observed events, and were obtained by the Gargamelle group by extrapolating the observed data (with $E_h > 1$ Gev) to $E_h = 0$. The Weinberg model, with a Weinberg angle of $\sin^2\theta_W = .38$, was used for this extrapolation.

These values are consistent with the high-energy Caltech ratios of $R_\nu = .266 \pm .024$ and $R_{\bar{\nu}} = .40 \pm .08$ (assuming scaling CC cross-sections with $\alpha = .17$).

In order to determine the sensitivity of these two experiments to Z_0 propagator effects, we have used the Caltech data to "predict", as a function of Z_0 mass, what the NC/CC ratios should be at very low neutrino energy (where the effects of the Z_0 propagator are small).

The calculation was made by fitting the best values of g_n and g_p, with the effects of the propagator included, to the Caltech data. These values of g_n and g_p were then used to calculate the NC/CC ratios expected at low energy where the propagator has little effect.

If we assume a Z_0 mass of 10 Gev, for example, then the coupling constants calculated from the Caltech data are $g_n = .28$ and $g_p = .13$, and the corresponding ratios at low energy are $R_\nu = .370 \pm .034$ and $R_{\bar{\nu}} = .51 \pm .10$. The calculated curve of R_ν versus M_Z is shown below. The corresponding curve for $R_{\bar{\nu}}$ is similar, but errors are larger.

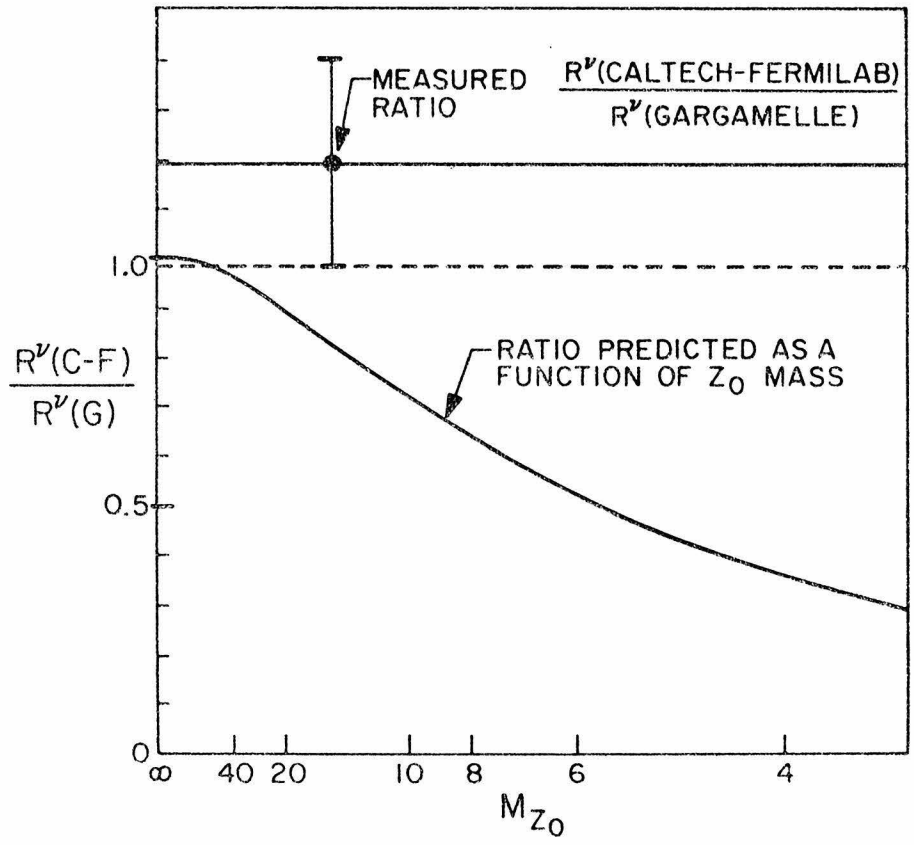

Figure 8-2: The ratio of the Gargamelle and Caltech measurements of R_ν is compared to the ratio expected if there is a Z_0 propagator. The measured ratio is represented by the solid horizontal line at the top, with the error indicated by the dashed line. The smooth curve, calculated from the Caltech data alone, shows the expected ratio as a function of Z_0 mass.

This calculation neglects possible non-scaling effects in the charged current total cross-section, and also neglects the small effects that the Z_0 propagator might have on the Gargamelle data. Nevertheless, it appears very unlikely (at >90 % confidence level) that there could be a Z_0 propagator with mass $\leq$10 Gev, or that comparable non-scaling effects could appear in the NC/CC ratios.

8.3 OTHER POSSIBILITIES

There are other possible kinds of interaction that could contribute to the neutral current signal. For example, a scalar or tensor coupling to scalar partons could produce a non-scaling neutral current interaction. The production of neutral heavy leptons with subsequent decays into neutrino plus hadrons could also produce muonless events. And the neutral current would not be hermitian if the final state particle is not a muon neutrino. All of these effects would produce NC events which are not of the form assumed here.

Because of the good agreement between the Caltech and Gargamelle data we can be sure that non-scaling effects are not major contributors to the neutral current signal. The assumptions of hermiticity and scaling are the simplest and most natural, and are in complete accord with the data. But if evidence of non-scaling effects should appear at higher energies, or if later and more precise experiments show a deviation from the relative shapes predicted by hermiticity, these assumptions would have to be reconsidered.

CHAPTER 9
CONCLUSIONS

9.1 SUMMARY OF NEUTRAL CURRENT RESULTS

This experiment has provided us with three major conclusions about the neutral current coupling in neutrino-nucleon interactions:

1) The close agreement between the NC/CC ratios found in the Caltech experiment and those found by the Gargamelle experiment at low energy provides strong evidence that both experiments are seeing the same kind of interaction, and that the interaction scales, at least approximately, over an incident neutrino energy range of from ~6 to ~60 Gev.

2) The hadron energy distributions of the neutral current events are consistent with a combination of V and A couplings, but do not support either pure V or pure V-A. The best determination of the coupling parameters is

$$g_{nc} = .32 \pm .03$$

$$P = .36 \pm .10$$

This value of the positive-helicity component lies approximately halfway between V ($P = .5$) and V-A ($P \approx .17$). In addition, a pure scalar coupling can be ruled out; however, the data do not exclude a large (1-y) component, which could result from a combination of scalar and tensor couplings.

3) These coupling parameters agree very well with the predictions of the Weinberg-Salam model, and indicate a Weinberg angle of

$$\sin^2\theta_W = .33 \pm .07$$

This is consistent with the ranges allowed by other experiments, involving both purely leptonic as well as semileptonic interactions (see reference [47]).

But the errors are still large, particularly in the antineutrino distributions. It is very clear that future experiments can provide a much more accurate determination of the coupling parameters and a more stringent test of the Weinberg model and similar theories.

9.2 PRESENT LIMITATIONS AND FUTURE IMPROVEMENTS

The most important source of error in this experiment was the statistical error due to the limited number of antineutrino events. The total errors in the coupling parameters could be reduced by a factor of two by accumulating 4 or 5 times more $\bar{\nu}$ events, and with no other changes to either the experimental or analysis techniques. Higher statistics would not only reduce the statistical error in the neutral current distributions, but would also better define the charged-current behavior.

In addition, there are several improvements that are being made, or have already been made, to the beam, detector, and to our knowledge of charged currents.

For example, the subtraction of wide-band background events was an important contributor to the statistical error in this experiment. The effect was two-fold, since the subtraction of this background from the open-slit data introduced a significant statistical error, and measuring the closed-slit backgrounds also required a considerable

fraction of the beam time. A new focusing system has been approved for the narrow band beam which will significantly reduce the wide-band background. This will be done by targetting the proton beam at 12 mrad, rather than the present 6 mrad, so that the wide band flux will be directed away from the neutrino detector. This means that the wide-band subtraction will be smaller and less beam time will be needed for closed-slit studies. The new beam will also have somewhat better acceptance so that rates will be higher, and will allow a wider range of secondary beam energies.

A second important step concerns measurements of the charged current interactions. The Caltech group completed a total cross-section experiment in October of 1975 which included several different beam energies ranging from 80 to 230 Gev for both neutrinos and antineutrinos. When this data has been analyzed, it should significantly improve our understanding of the charged currents. It will not directly improve our knowledge of the very wide angle events, since the acceptance in the total cross-section experiment was the same as in the neutral current experiment. The new data should, however, provide two very important pieces of information which are relevant to further neutral current studies:

(1) Since the hadron fluxes were directly measured during the experiment, the data will be externally normalized (with 5-10% errors). These cross-section measurements will provide a basis for normalization of future neutral current studies. By using the charged current data of future neutral current runs, combined with the measured partial cross-sections over the regions where the experiment has 100% acceptance, the normalization can be determined in a way that is totally independent of any assumptions about the CC distributions.

(2) Since the CC experiment included very high energy antineutrino data, with 10 times the statistics of the neutral current run, it should provide a good measurement of the form of

possible scale-breaking effects. This information will clearly be relevant in determining the shape of the angular distribution of CC events at lower energies.

Finally, a number of changes have been made to the Caltech detector. The experiment has been moved into a new building, and the 5' diameter spectrometer has been replaced by three 11' diameter magnets. In addition, the 5' by 5' target calorimeter will be replaced by a similar apparatus measuring 10' by 10'. The acceptance of the new apparatus will therefore be far superior to the old one. By defining a fiducial volume over only the central 5' by 5' area of the new apparatus, the fraction of events with "missed muons" will be reduced by at least a factor of two. The uncertainties in extrapolation will be reduced even more.

It has now been almost exactly four years since the first neutrino event was observed at Fermilab by the Caltech group, and three years since the first neutral current event was observed. We can be certain that the information regarding both charged and neutral currents will be greatly expanded and improved over the next three years. It is not too optimistic to believe that within a similar time scale this will lead to a unified theoretical description, or at least a much deeper understanding, of both charged and neutral current couplings.

APPENDIX A
BASIC THEORETICAL FRAMEWORK OF ν-N SCATTERING

It is generally assumed[14] that the effective Lagrangian for semi-leptonic weak interactions is given by

$$\mathcal{L}_{eff} = \frac{G}{2} J^{\dagger}_{(\ell)\alpha} J^{\alpha}_{(h)} + h.c. \qquad (A\text{-}1)$$

where $J_{(\ell)\alpha} = \bar{\psi}_{\ell}(x)\gamma_{\alpha}(1-\gamma_5)\psi_{\ell'}(x)$, with $\ell = \mu$, e and $\ell' = \nu_{\mu}$, ν_{e}. The $\nu + N \rightarrow \mu^{-} + X$ cross-section is then proportional to a product $m_{\mu\nu} W^{\mu\nu}$ of leptonic and hadronic tensors, averaged over initial polarizations and summed over final states. The leptonic part is easily calculated. With k = initial neutrino momentum and q = momentum transfer,

$$\Sigma\bar{\Sigma}\, m^{\nu,\bar{\nu}}_{\mu\nu} = 4[2k_{\mu}k_{\nu} - (q_{\mu}k_{\nu} + k_{\mu}q_{\nu}) + \tilde{q}\cdot\tilde{k}g_{\mu\nu} \pm i\epsilon_{\sigma\rho\mu\nu}q^{\sigma}k^{\rho}] \qquad (A\text{-}2)$$

The hadronic part cannot be directly evaluated, but from its tensor structure we can write its most general form in terms of six structure functions $W_i(q^2,\nu)$:

$$\Sigma\bar{\Sigma}\, W_{\mu\nu} = -g_{\mu\nu}W_1(\nu,q^2) + \frac{p_{\mu}p_{\nu}}{M^2}W_2(\nu,q^2) - i\frac{\epsilon_{\mu\nu\rho\sigma}p^{\rho}q^{\sigma}}{2M^2}W_3(\nu,q^2) \qquad (A\text{-}3)$$

$$+ \frac{q_{\mu}q_{\nu}}{M^2}W_4(\nu,q^2) + \frac{p_{\mu}q_{\nu}+q_{\mu}p_{\nu}}{2M^2}W_5(\nu,q^2) + i\frac{p_{\mu}q_{\nu}-q_{\mu}p_{\nu}}{2M^2}W_6(\nu,q^2)$$

where p is the nucleon momentum and $\nu = q\cdot p/M_N$ is the energy transfer in the lab. Multiplying these two tensors together and neglecting terms with coefficients of order $(m_{\mu}/M_N)^2$, we obtain

$$\frac{d^2\sigma^{\nu,\bar{\nu}}}{dq^2 d\nu} = \frac{G^2}{16\pi ME^2}\left(\Sigma\bar{\Sigma}\ m_{\mu\nu}W^{\mu\nu}\right) \qquad (A\text{-}4)$$

$$= \frac{G^2}{4\pi ME^2}\left(-q^2\cdot W_1^{\nu,\bar{\nu}}(\nu,q^2) + \left[2E(E-\nu)+\frac{q^2}{2}\right]\cdot W_2^{\nu,\bar{\nu}}(\nu,q^2)\right.$$

$$\left. \pm \frac{q^2}{M}\left(E-\frac{\nu}{2}\right)\cdot W_3^{\nu,\bar{\nu}}(\nu,q^2)\right)$$

To put this in a somewhat more familiar form, transform to the scaling variables $x = -q^2/2M\nu$ and $y = \nu/E_\nu$, and substitute

$$W_1^{\nu,\bar{\nu}}(\nu,q^2) \to F_1^{\nu,\bar{\nu}}(\nu,q^2), \quad \frac{\nu}{M}W_i^{\nu,\bar{\nu}}(\nu,q^2) \to F_i^{\nu,\bar{\nu}}(\nu,q^2) \quad \text{for } i \neq 1$$

Then

$$\frac{d^2\sigma^{\nu,\bar{\nu}}}{dxdy} = \frac{G^2ME}{\pi}\left(xy^2\cdot F_1^{\nu,\bar{\nu}}(\nu,q^2) + \left[1-y-\frac{M}{2E}xy\right]\cdot F_2^{\nu,\bar{\nu}}(\nu,q^2)\right.$$

$$\left. \mp xy\left(1-\frac{y}{2}\right)\cdot F_3^{\nu,\bar{\nu}}(\nu,q^2)\right) \qquad (A\text{-}5)$$

We are probably on safe ground at this point. To proceed any further, we need to make several assumptions which may be ultimately proved wrong, but which are at least approximately correct at low energies.

Assumption 1 -- Charge symmetry[14]: Since the neutron and proton form an isospin doublet, the inclusive interactions

$$\nu + (n,p) \to \mu^- + X \qquad \text{and} \qquad \bar{\nu} + (p,n) \to \mu^+ + X'$$

can be transformed into one another by a) a rotation in isospin space and b) a charge conjugation operation. This will be valid only if X, X' are also related by an isospin rotation -- i.e., if the weak interaction has SU(2) symmetry. This is expected to hold true for strangeness-conserving reactions, but is broken at the 5% level by strangeness-changing reactions (i.e., by the Cabibbo mixing of d and s quark states). In a model with charm, this symmetry is recovered above charm threshold, so in both charmed and uncharmed models the relation is good to at least the 5% level. It is consistent with all

experimental data below 30 Gev[18,19,32]. But if there are quark states of higher mass the symmetry could be badly broken at very high energy[33,34,40].

With this assumption, $F_i^{\nu p}(q^2,\nu) = F_i^{\bar{\nu}n}(q^2,\nu)$ and $F_i^{\bar{\nu}p}(q^2,\nu) = F_i^{\nu n}(q^2,\nu)$, and consequently

$$F_i^{\nu N} = \frac{1}{2}(F_i^{\nu n} + F_i^{\nu p}) = \frac{1}{2}(F_i^{\bar{\nu}p} + F_i^{\bar{\nu}n}) = F_i^{\bar{\nu}N} \qquad \text{(A-6)}$$

The structure functions for neutrino and antineutrino on an isoscalar target should therefore be equal, so we can drop the superscripts in equation A-5.

Note that the Fe target used in this experiment is not exactly isoscalar (Z = 26, N = 30). The imbalance of protons and neutrons causes a 4% deviation from A-5 in relative $\bar{\nu}/\nu$ normalization, which tends to cancel the 5% difference due to the Cabibbo angle in the three-quark model. We have therefore ignored both of these effects.

In the case of neutral currents, the assumption of charge symmetry is not necessary to obtain this result. The much stronger relations

$$F_i^{\nu p} = F_i^{\bar{\nu}p} \qquad \text{and} \qquad F_i^{\nu n} = F_i^{\bar{\nu}n} \qquad \text{(A-7)}$$

follow from the hermiticity of the neutral current[9]. This symmetry means that equation A-6 is valid for neutral currents with any target (not only isoscalar targets) even if charge symmetry is broken for charged currents.

Assumption 2 -- Bjorken scaling[16]: At high energy and in the absence of any scale-defining masses, the structure functions (which are dimensionless) must depend only on the dimensionless quantity $x = -q^2/2M\nu$; the structure functions in equation A-5 thus become functions of a single variable.

Assumption 3 -- Callan-Gross relation[17]: $2xF_1(x) = F_2(x)$. In the parton model, this is equivalent to assuming that the constituent partons are spin-1/2 particles.

Using these first three assumptions, we can rewrite equation A-5 as

$$\frac{d^2\sigma^{\nu,\bar{\nu}}}{dx\,dy} = \frac{G^2 ME}{\pi}\left[F_2(x)\left(1 - y + \frac{y^2}{2}\right) \pm x F_3(x)\left(-y + \frac{y^2}{2}\right)\right] \qquad \text{(A-8)}$$

Defining

$$Q(x) = \frac{1}{2}\left(F_2(x) + x F_1(x)\right) \qquad \text{(A-9a)}$$

and

$$\bar{Q}(x) = \frac{1}{2}\left(F_2(x) - x F_1(x)\right) \qquad \text{(A-9b)}$$

we have

$$\frac{d^2\sigma^{\nu}}{dxdy} = \frac{G^2 ME}{\pi}\left[Q(x) + \bar{Q}(x)\,(1-y)^2\right] \qquad \text{(A-10a)}$$

$$\frac{d^2\sigma^{\bar{\nu}}}{dxdy} = \frac{G^2 ME}{\pi}\left[\bar{Q}(x) + Q(x)\,(1-y)^2\right] \qquad \text{(A-10b)}$$

which is the same as equation 6-1. This form is also derivable from the parton model, in which x is physically interpreted as the momentum carried by the scattered parton and $Q(x)$ and $\bar{Q}(x)$ are the momentum distributions of partons and antipartons in the nucleon[15].

We have not yet made any assumptions regarding shape or normalization of these functions.

Assumption 4 -- Isospin triplet hypothesis and current algebra (and/or quark-parton model)[14,15]: This relates the shape of the structure functions in ν-N scattering to those measured in e-N scattering:

$$F_2^{\nu N}(x) \propto F_2^{eN}(x) \qquad \text{(A-11)}$$

[We will use the terms "quark" and "parton" more or less interchangeably. In general, we do not assume the specific

"quark-model" characteristics of fractional charge, 3 or 4 quark flavors, etc., but only use the more general "parton-model" properties specifically mentioned in this appendix. For example, the quark model makes the specific prediction that $F_2^{\nu N}(x) \approx \frac{18}{5} F_2^{ed}(x)$. In the neutral current analysis, we do not use this relation for normalization; we have only used $F_2^{ed}(x)$ for the shape of $F_2^{\nu N}(x)$.]

$F_2(x)$ has been fitted by several different kinds of theoretical curves (see [35] and references cited). We have used Bodek's fit to the SLAC-MIT data, which is a polynomial in (1-x) (see section 6-3). It is virtually certain that this parameterization will change in the future. Low energy Gargamelle measurements[18] show a steeper slope in $F(x)$ at small x, and high energy Fermilab muon experiments[41] show a flatter slope. The difference may be due in part to q^2 dependence at low energy (i.e., the Slac data is not yet completely scaling). In any case, the Bodek fit appears to be a good compromise between all the available data, and the determination of the neutral current couplings in this thesis is not sensitive to variations in the shape of $F_2(x)$.

APPENDIX B

Y-DEPENDENCE AND V, A STRUCTURE OF THE COUPLING

The relationship between the space-time structure of the neutrino-nucleon coupling and the y-dependence of the interaction is seen most easily in the quark-parton model[15]. In this model, the deep inelastic neutrino-nucleon interaction is attributed to an elastic neutrino-quark scatter.

In the neutrino-quark center-of-mass system, the invariant kinematic variable y is directly related to the scattering angle of the final state lepton. The scattering angle distribution in this system, and thus the y-distribution in any system, is determined by the helicities of the two interacting spin-1/2 particles.

Case 1: Opposite sign helicities.

If the interacting quark and neutrino have opposite helicities, then the spins are parallel and the scattering occurs through a J=1, J_z=1 state:

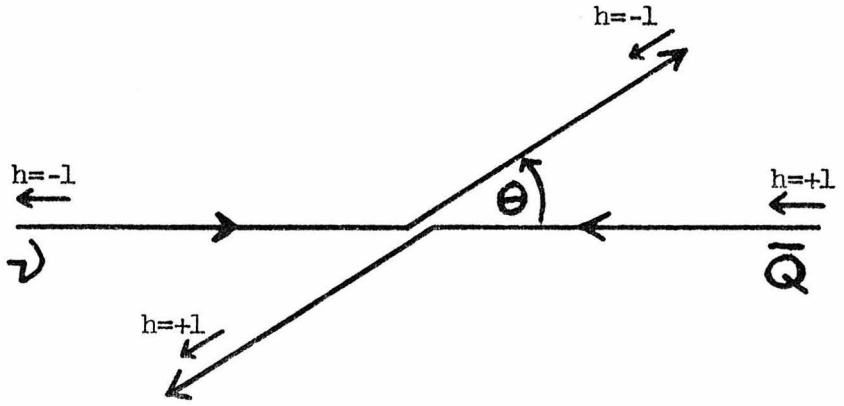

Since the V and A couplings preserve helicities, the final state helicities are the same as the initial state helicities. The final state spins are therefore rotated through an angle θ with respect to the incident spins. The dependence of the scattering angle is given by the (1,1) component of the rotation matrix for two spin-1/2 particles:

$$d^1_{11}(\theta) = \frac{1+\cos\theta}{2} \quad \Rightarrow \quad \frac{d\sigma}{d(\cos\theta)} = \frac{1}{2}\left(\frac{1+\cos\theta}{2}\right)^2 \qquad \text{(B-1)}$$

But this scattering angle is directly related to the kinematic invariant $y = 2\,\tilde{q}\cdot\tilde{p}^i_Q/s$. In the neutrino-parton c.m. system,

$$p^{i,f}_\nu \approx E^{i,f}_\nu \approx p^{i,f}_Q \approx E^{i,f}_Q \equiv E_\nu$$

$$\Rightarrow \quad s = (\tilde{p}^i_\nu + \tilde{p}^i_Q)^2 \approx 4E^2_\nu$$

$$\tilde{q}\cdot\tilde{p}^i_Q = (\tilde{p}^i_\nu - \tilde{p}^f_\nu)\cdot\tilde{p}^i_Q \approx E^2_\nu\,(1-\cos\theta)$$

Then $$y = 2\,\frac{\tilde{q}\cdot\tilde{p}^i_Q}{s} \approx \frac{1-\cos\theta}{2} \qquad \text{(B-2)}$$

Substituting into equation (B-1) yields

$$\frac{d\sigma}{dy} = (1-y)^2 \qquad \text{(B-3)}$$

An opposite-helicity collision therefore produces a $(1-y)^2$ distribution in y.

Case 2: Same Sign Helicities.

If the neutrino and parton have the same helicity, then the scattering occurs through a J=0 state and is uniform in angular distribution:

$$\frac{d\sigma}{d(\cos\theta)} = \frac{1}{2} \quad \Rightarrow \quad \frac{d\sigma}{dy} = 1 \tag{B-4}$$

The J=1, J_z=0 scatter, which would contribute an additional $\cos\theta$ term, is not allowed in V and A interactions.

The y-distributions of neutrino-parton interactions are therefore determined by the helicities of the interacting particles. Since the V-A coupling operator $(1-\gamma_5)$ is proportional to the negative-helicity projection operator, a V-A coupling projects out negative-helicity parton states and positive-helicity antiparton states. Since the neutrino has negative helicity and the antineutrino has positive helicity, the relative helicities and consequently the y-distributions are determined by which particles interact:

ν - parton $\Rightarrow$ same helicity $\Rightarrow$ $\frac{d\sigma}{dy} = 1$

ν - antiparton $\Rightarrow$ opposite helicity $\Rightarrow$ $\frac{d\sigma}{dy} = (1-y)^2$

$\bar{\nu}$ - parton $\Rightarrow$ opposite helicity $\Rightarrow$ $\frac{d\sigma}{dy} = (1-y)^2$

$\bar{\nu}$ - antiparton $\Rightarrow$ same helicity $\Rightarrow$ $\frac{d\sigma}{dy} = 1$

The y-distributions of V-A scattering are therefore given by

$$\frac{d\sigma^{\nu}}{dy} = (1-\alpha) + \alpha(1-y)^2 \tag{B-5a}$$

$$\frac{d\sigma^{\bar{\nu}}}{dy} = \alpha + (1-\alpha)(1-y)^2 \tag{B-5b}$$

where $\alpha = \Sigma\bar{Q} / \Sigma(Q+\bar{Q})$ is the fraction of the nucleon momentum carried by the antipartons.

If the scattering occurs through V+A coupling, then positive-helicity parton and negative-helicity antiparton states are projected. The scattering is given by

$$\frac{d\sigma^{\nu}}{dy} = \alpha + (1 - \alpha)(1 - y)^2 \qquad \text{(B-6a)}$$

$$\frac{d\sigma^{\bar{\nu}}}{dy} = (1 - \alpha) + \alpha (1 - y)^2 \qquad \text{(B-6b)}$$

Now suppose that the fractional V+A coupling is given by β, and the fractional V-A coupling by $(1-\beta)$. Since V+A and V-A do not interfere,

$$\frac{d\sigma^{\nu}}{dy} \propto (1-\beta)[(1-\alpha) + \alpha(1-y)^2] + \beta[(1-\alpha)(1-y)^2 + \alpha] \qquad \text{(B-7a)}$$

$$= (1 - P) + P(1 - y)^2$$

where $P = \alpha + \beta - 2\alpha\beta$. Similarly,

$$\frac{d\sigma^{\bar{\nu}}}{dy} = P + (1 - P)(1 - y)^2 \qquad \text{(B-7b)}$$

P in these equations represents the total fraction of positive-helicity scattering, due to the combined contributions from V-A scattering off antipartons and V+A scattering off partons.

In the pure scaling quark-parton model, these considerations apply to both NC and CC scattering. If the charged-current interaction occurs through V-A only (as indicated by low-energy data) then α can be measured from CC interactions. This value of α and the value of P measured from NC interactions could be used to extract β.

However, there are indications that the scaling model breaks down at high energies. In particular, the symmetry between ν and $\bar{\nu}$ in equations B-5 depends, for charged currents, on the charge-symmetry between neutron and proton. This symmetry could be broken at high energies by new parton states of high masses[40]. If this is the case, the value of α obtained by fitting B-5 to the CC data would not reflect the true antiparton component, and β could not be extracted from P. Equations B-7, however, would still be valid for neutral current interactions (see Appendix A).

References

1. B. C. Barish et al., Fermilab proposal No. 320 (1974); and B. C. Barish, J. F. Bartlett, A. Bodek, K. W. Brown, D. Buchholz, H. E. Fisk, G. Krafczyk, F. Jacquet, F. Merritt, F. J. Sciulli, L. Stutte, E. Suter, Proceedings of la Physique du Neutrino a Haute Energie, Ecole Polytechnique, Paris, France (1975), p. 291 (presented by F. Merritt).

2. C. Rubbia, Proceedings of the XVI International Conference on High Energy Physics, Vol. 4, 249 (Batavia, 1972).

3. D. H. Perkins, Proceedings of the XVI International Conference on High Energy Physics, Vol 4, 189 (Batavia, 1972).

4. F. J. Hasert et al., Phys. Lett., 46B, 138 (1973); and F. J. Hasert et al., Nucl. Phys. B73, 1 (1974).

5. A. Benvenuti et al., Phys. Rev. Lett. 32, 800 (1974).

6. B. C. Barish et al., Phys. Rev. Lett. 34, 538 (1975).

7. B. Aubert et al., Phys. Rev. Lett. 32, 1457 (1974).

8. S. L. Adler, Fermilab-Pub-74, 90-THY, Sep. 1974; and P. A. Schreiner, Argonne National Laboratory Report ANL/HEP 7436 (also presented at XVII International Conference on High Energy Physics, London, July 1974.

9. E. S. Abers and B. W. Lee, Physics Reports 9, 1 (1973); and A. de Rujula, "An Elementary Introduction to Unified Theories of Weak and Electromagnetic Interactions," Harvard preprint (1973).

10. S. Weinberg, Phys. Rev. Lett. 19, 1264 (1967);
and A. Salam, Elementary Particle Theory, ed. N. Svartholm (Almquist and Forlag, Stockholm, 1968).

11. S. Glashow, J. Iliopoulos, L. Maiani, Phys. Rev. D2, 1285 (1970).

12. B. W. Lee, Proceedings of 1975 Int. Symposium on Lepton and Photon Interactions at High Energies (Stanford, 1975), p. 635 (and references therein).

13. B. Kayser et al., Phys. Lett. 52B, 385 (1974);
R. L. Kingsley, F. Wilczek, A. Zee, Phys. Rev. D10, 2216 (1974).

14. C. H. Llewellyn-Smith, Physics Reports, Vol. 3C, 261 (1972).

15. R. P. Feynman, Photon-Hadron Interactions, Benjamin Inc., 1972;
and C. Franzinetti, Proceedings of "Weak and Electromagnetic Interactions at High Energy" (Cargese, 1975), p. 177-193. Feynman gives a very detailed study of the parton model, but concentrates mostly on electromagnetic interactions. Franzinetti gives a good review of the parton model as applied to neutrino interactions.

16. J. D. Bjorken, Phys. Rev., 179, 1547 (1969).

17. C. G. Callan and D. Gross, Phys. Rev. Lett. 22, 156 (1969).

18. H. Deden et al., Nucl. Phys. B85, 269 (1975).

19. B. C. Barish et al., Phys. Rev. Lett., 35, 1316 (1975).

20. B. C. Barish et al., NAL proposal No. E-21, 1970.

21. T. Humphrey, Ph.D. thesis, Cal. Institute of Tech., (unpublished).

22. P. Limon et al., Nucl. Instr. and Meth. 116, 317 (1974).

23. H. Grote, R. Hagedorn, J. Ranft, Atlas of Particle Production Spectra, CERN (1970).

24. B. C. Barish et al., Status Report

25. C. W. Fabjan, W. J. Ellis, Proceedings of Calorimeter Workshop (Fermilab, May 1975), p. 1.

26. B. C. Barish et al., Nucl. Instr. and Meth. 116, 413 (1974).

27. B. P. Roe, Proceedings of Washington APS Meeting, April 1975; and B. P. Roe, Proc. of 1975 Int. Conference on Lepton and Photon Interactions at High Energies (Stanford, 1975), p. 537.

28. B. C. Barish et al., Nucl. Instr. and Meth. 130, 49 (1975).

29. Proceedings of the Calorimeter Workshop (Fermilab, May 1975), (in particular, rapporteur talk by F. J. Sciulli on p. 79).

30. A. Rousset, Neutrinos--1974 (AIP Conference Proceedings, Philadelphia, 1974), p. 344.

31. G. B. Yodh et al., Proceedings of the Calorimeter Workshop (Fermilab, May 1975), p. 201.

32. A. Benvenuti et al., Phys. Rev. Lett. 32, 125 (1974).

33. R. Imlay et al., Proceedings of the XVII International Conference on High Energy Physics (London, July 1974), p. IV-100.

34. B. C. Barish et al., "Charged Current Differential Distributions in Caltech-Fermilab Experiment", CALT 68-560 (to be published in Phys. Rev. Lett.).

35. For a recent review, see R. Taylor, Proceedings of the 1975 Int. Symposium on Lepton and Photon Interactions at High Energy (Stanford, 1975), p. 679.

36. A. Bodek, Ph. D. Thesis, Mass. Institute of Technology, Report No. COO-3069-116, 1973 (unpublished).

37. D. Gross and C. H. Llewellyn-Smith, Nucl. Phys. B14, 337 (1969).

38. A. Benvenuti et al., Phys. Rev. Lett. 32, 125 (1974).

39. F. Sciulli, Proceedings of XVII Int. Conf. on High Energy Physics (London, 1974), p. IV-105.

40. R. M. Barnett, "Evidence in Neutrino Scattering for Right-Handed Currents Associated with Heavy Quarks," Harvard preprint (Jan. 1976).

41. L. Mo, Proc. of 1975 Int. Symposium on Lepton and Photon Interactions (Stanford, 1975), p. 651.

42. L. Wolfenstein, Proc. of 1975 Int. Symposium on Lepton and Photon Interactions (Stanford, 1975), p. 613; also see L. Wolfenstein, Nucl. Phys. B91, 95 (1975).

43. L. M. Sehgal, Nucl. Phys. B65, 141 (1973).

44. D. H. Perkins, Proc. of 1975 Symposium on Lepton and Photon Interactions (Stanford, 1975), p. 571.

45. D. Cline, Proceedings of International Conference on High Energy Physics (Palermo, Sicily, 1975).

46. F. J. Sciulli, private communication.

47. J. G. Morfin, Proc. of the 1975 Int. Symposium on Lepton and Photon Interactions at High Energies (Stanford, 1975), p. 537.

48. A. Benvenuti et al., "Evidence for Parity Non-Conservation in the Weak Neutral Current," HPWF-76/4 (1976). (This has recently been published in Phys. Rev. Lett. 37, 1039 (1976)).

49. P. Musset, Proceedings of the Tenth Rencontre de Moriond (Meribel-les-Allues, France, 1975).